Modeling of Deformation and Energy Dissipation for a Tumbling Body

by

Ryotaro Sakamoto

B.A., Tokyo Metropolitan University, 2011

M.S., National Defense Academy of Japan, 2016

A thesis submitted to the

Faculty of the Graduate School of the

University of Colorado in partial fulfillment

of the requirements for the degree of

Doctor of Philosophy

Department of Aerospace Engineering Sciences

2023

Committee Members:

Daniel Scheeres, Chair

Jay MacMahon

Marcus Holzinger

Yuichi Tsuda

Hiroaki Tanaka

Sakamoto, Ryotaro (Ph.D., Aerospace Engineering Sciences)

Modeling of Deformation and Energy Dissipation

for a Tumbling Body

Thesis directed by Prof. Daniel Scheeres

Several factors cause changes of spin rate and axes of rotational bodies such as space debris and small asteroids, even artificial satellites. Although these factors cannot be simply categorized, the Yarkovsky-O'Keefe-Radzievskii-Paddack (YORP) is considered as primary effects on the rotational body as external torque. On the other hand, structural friction and sloshing of liquid are thought as internal causes of rotational change. Again, these causes are not simple, since they interact with each other within a system. For example, if spin rate is changed due to external torque, sloshing and structural frictions occur inside the system.

A better understanding of de-tumbling could contribute to active debris removal and satellite servicing and undergoing RPO(Rendezvous and Proximity Operation) missions. De-tumbling, rotational axis in the body, and relaxation times are crucial pieces of information to conduct these missions. Currently, spin rate change and de-tumbling are found via ground observation and YORP simulation. However, to fully reveal the mechanisms of the change in spinning conditions, its internal energy dissipations are needed.

Therefore, this study explores the interaction between de-tumbling and its internal energy dissipation in a defunct satellite. To capture structural effects on the rotational body, FEM(Finite Element Methods) are used as analysis methods. Based on simple satellite body and rotational dynamics, internal energy dissipation is modeled with variations of damping, spinning conditions, and its mechanical sensitivity such as mass and stiffness matrices. This modeling helps us to reduce computational time which generally needs a long term simulation and tiny damping cases. Also, this modeling is able to estimate relaxation time of de-tumbling. To validate internal energy dissipation theory, it is evaluated with actual mission program with considering sloshing dissipation.

Acknowledgements

It's been exactly six years since I received the acceptance offer from Colorado University at Boulder and I'm truly honored to have enrolled in the PhD program in Aerospace Engineering. Due to the spread of COVID-19, my PhD life has been dynamic. These unprecedented circumstances are great examples of unavoidable issues, that has taught me valuable life lessons; that anything could come across our lives. First of all, I am very grateful to Dr.Scheeres for giving me the opportunity to pursue a PhD program at CU. He guided my research work in precise direction and has always provided accurate insight of research ideas. This PhD life would not have been possible without his support. I would also like to thank the CU professors. Taking Dr.MacMahon's lecture was really interesting and I enjoyed working on assignments. I was actively engaged in the class, which students positively discuss even outside of lectures. I would also like to thank Dr.Holzinger. His research and talks made me more interested in SSA and motivated me to pursue SSA duty in the Air Force. I am happy to have met such wonderful teachers at CU. I am also grateful to Dr.Tsuda at JAXA, who kindly agreed to be a visiting scholar when I returned to Japan due to the pandemic. I was able to meet many excellent people at JAXA by attending seminars and conferences. I would also really like to thank Dr.Tanaka at the National Defense Academy of Japan, who is my previous advisor. Even after I graduated from the master degree program in Japan, he supported my PhD study when I was stuck in my research issues.

In these years, since remote work has become a trend, I was able to receive research advice through meetings even though we are in different locations. I would like to use what I learned as a CU student in my future life.

Contents

Chapter

Tables

Table

Figures

Figure

Chapter 1

Introduction

1.1 Motivation

Outer space is an essential region nowadays which supports many activities on the globe including security, economic and scientific issues. Various kinds of satellites have been launched for observation, communication, broadcasting and positioning, making outer space a location for key infrastructure for both the public and private sectors. One trend is satellite constellations in Low Earth Orbit (LEO) [45]. Companies like Amazon, SpaceX, and OneWeb have been launching LEO satellites and providing high-speed internet services to various area in resent years. In February of 2022, Starlink and its satellite constellation gathered attention from all over the world. Soon after Russia's invasion of Ukraine began, Starlink provided communication service to the Ukrainian area. In addition to LEO, the Geostationary Earth Orbit (GEO) has also become a more crowded region of space. Because of the advantages of this orbital region, the number of communication satellites are increasing. On the other hand, the continuously increasing population of space objects, either active or defunct satellites, or more generally, space debris, requires us to consider several potential problems for space activities.

For space operations, if the amount of debris is increased, the risk of active satellite colliding with debris increases as well. Also, Kessler proposed the model of the number of the increasing debris considering collisions between space objects in an orbit [18]. Especially in the GEO, due to the lack of a natural cleaning phenomena, such as atmospheric drag, unused satellites are in the GEO for a long time, such as tens or hundred years [49]. Figure 1.1 shows a graph of the

actual increase of cataloged debris [1]. In outer space, the Space Surveillance Network (SSN) has tracked more than 25,000 pieces of debris. The increase in debris in 2007, 2009 and 2021 is due to the effects of China's satellite destruction test, US and Russian satellite collisions, and Russia's satellite destruction test, respectively.

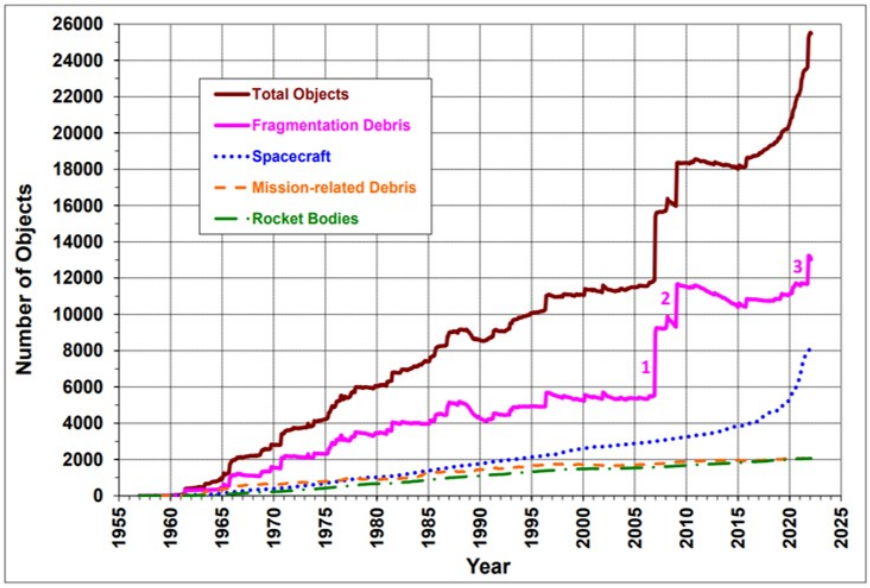

Figure 1.1: Increase of the Cataloged Objects Based on Data Available on 1 March 2022

To reduce collisions risk and the amount of debris, several approaches are being considered. In 2007, Space Debris Mitigation Guidelines were published by the United Nations (UN) [40]. Although this guideline is not legally effects on space activities, it establishes standards for design, operation, and post-operation to prevent satellites from turning into space debris. Even before starting to establish mitigation guidelines for space debris, many researchers have presented ideas for end of life disposal of space craft. Some examples of this are chemical or electrical propulsion, drag sails, solar radiation sails, and tether technologies [37].

As a different approach to mitigation guidelines, numerous organizations have proposed active debris removal (ADR) missions. JAXA (Japan Aerospace Exploration Agency) operates ADR programs with public companies [42]. One Japanese company, Astroscale, launched ELSA-d as a mission satellite to capture a spacecraft in 2021. It successfully demonstrated its magnetic capture

system to dock, hold and release client space craft. SKY Perfect JSAT Co. started designing and developing ADR satellite using laser ablation technologies [20]. Among these ADR missions, many technical difficulties are discussed and researched. Examples of these difficulties include trajectory design and propulsion necessary to approach the target, the observation technology to grasp the attitude of target debris and prediction associated with it, and the internal structure and materials of each chaser and target are also important topics for the mission. Thus, the mission of space debris reduction is important for our lives, and many studies are being conducted.

1.2 YORP Theory and Tumbling

For ADR missions, one of the challenges is that the target object may be tumbling, which means spinning with a time varying axis. When approaching and rendezvousing with an active and cooperative target, which is able to control its attitude, target capturing becomes easier. However, when a target satellite is malfunctioning or inactive, its attitude control system may be disabled and thus can be considered to be a non-cooperative target [59]. Therefore, the dynamics of non-cooperative object raise a number of interesting questions and has been a hot area of research for several years. Analysis by ground observations has shown that Solar Radiation Pressure (SRP) leading to the Yarkovsky-OKeefe-Radizievskii-Paddack (YORP) effect is considered to be one cause of spin rate changes in celestial bodies [44, 8]. The YORP effect arises from an unbalanced torque between SRP and heat radiation from the surface of the space object [50]. Several researchers studied spin rate transitions caused by the YORP effect around asteroids [39]. Also, the YORP effect acting on inactive satellites and not just small asteroids, has also been investigated [3]. Of course, several factors cause changes of spin rate and changes in axes of rotational bodies and the YORP effect alone cannot be simply categorized as the main reason for tumbling. But, the YORP effect is considered as a primary effect on a rotational body via external torque.

In a recent study, Albuja et al explored the YORP effect for defunct satellites in GEO, such as the Geostationary Operational Environmental Satellites (GOES) 8 and 10 satellites [2]. The GOES family is composed of eleven weather satellites, five of which have been de-commissioned.

They also proposed that energy dissipation plays an important role in understanding the dynamics of a tumbling satellite since external torque modeling alone cannot capture tumbling mechanism perfectly. For a truly rigid body, the kinetic energy is conserved without any external torque for rigid body dynamics. However, for satellites, friction between structural components or sloshing of internal liquid will cause energy dissipation [33, 13]. As the tumbling spacecraft loses energy, the rotation axis moves into coincidence with the maximum momentum inertia, which equals the minimum energy state [47]. Even decreasing kinetic energy, does not affect its angular momentum. This is called as a de-tumbling.

1.3 Structural Dynamics and Energy Dissipation

Again, the YORP effect alone cannot explain the mechanism of energy dissipation perfectly. Some researches shows that asteroid periodic spin has de-tumbling to minimum energy state in million years [46]. One reason for this was thought to be thermal conductivity. Periodical centrifugal force being lost as heat as part of the stress-strain cycle [11]. Thus internal energy dissipation breaks pure YORP spin by keeping angular momentum constant. This phenomena affects not only asteroids but debris as well.

Therefore, the structural dynamic analysis of debris capturing is a hot research topic on not only the capturing side, but also the targeting side. For instance, tethered satellite systems are being investigated by many researchers who are considering the influence of aerodynamics, perturbed motion, electrodynamics, and control strategy [16, 32, 41]. They proposed dynamics analysis based on multi-body systems. In terms of the structural dynamics and attitude motion of space debris, coupling effects have been explored in various situations [28]. One of these is the coupling effect of the flexible damping beam, spatial motion, and vibration of the system [26]. They concluded that even if damping is weak, the damping effect on the long-time dynamic behaviors of the spatial flexible beam could not be neglected. To reveal the attitude of the defunct satellite under the Coulomb forces, the influence of the flexible appendages should be investigated [4]. Similarly, to clarify the dynamic interaction behavior of a flexible body component, sloshing and control model

should be examined. They investigate the influence of the vibration and sloshing along with the flexible appendages such as antenna and solar arrays as well as the on-board liquid system [13]. In most of the above works, regardless of the cooperative or non-cooperative space craft model, they used simplified models with point mass on flexible appendages and a rigid body. Furthermore, the damping and deformation cannot be taken into account, which may result in error of dynamic analysis [27]. Thus, flexibility is a key to understanding rotational dynamics, and a flexible body component is assumed to be a trigger to change the dynamic behavior of space craft and their energy dissipation [15, 54]. Although the effect acts over a much longer period of time, flexure is also modeled as the dissipation of energy within asteroids [12, 24].

Therefore, detailed modeling of flexible dynamic analysis could contribute space mission and its attitude motion. As the analysis approach, Finite Element Method (FEM) is used for numerical simulations in this research, because FEM is the most popular method to examine structural discussion [14]. As I discussed above, understanding structural dynamics with flexible and rigid bodies in space is important for debris issues. The core topic of this study is understanding the influence of flexible components on satellites' spin rate and energy dissipation considering the deformation of the model.

1.4 Contributions

Although there are several factors that could cause internal energy dissipation, in this thesis, I focus on the deformation of defunct satellites, modeled with an FEM method that includes flexible and damping modes. Figure 1.2 illustrates the research area and academic topics. As already discussed above, within the general debris and their dynamical problem, there are three physical phenomena that interact each other: energy dissipations, de-tumbling, and deformations of bodies. As an example of previous studies, the relationship between de-tumbling and the YORP effect as an external torque was studied. But internal energy dissipation was not well understood as part of the relationship. Therefore, internal causes of energy dissipations and de-tumbling are focused on in this study. Basic theories and equations of rotational dynamics are used for simulations

and they help us to estimate relaxation time. As part of the structural approach, rigid body and flexible body need to be considered to capture dynamic behavior. In this area, variations of energy dissipations with damping effects and sensitivity of mass and stiffness parameters are discussed.

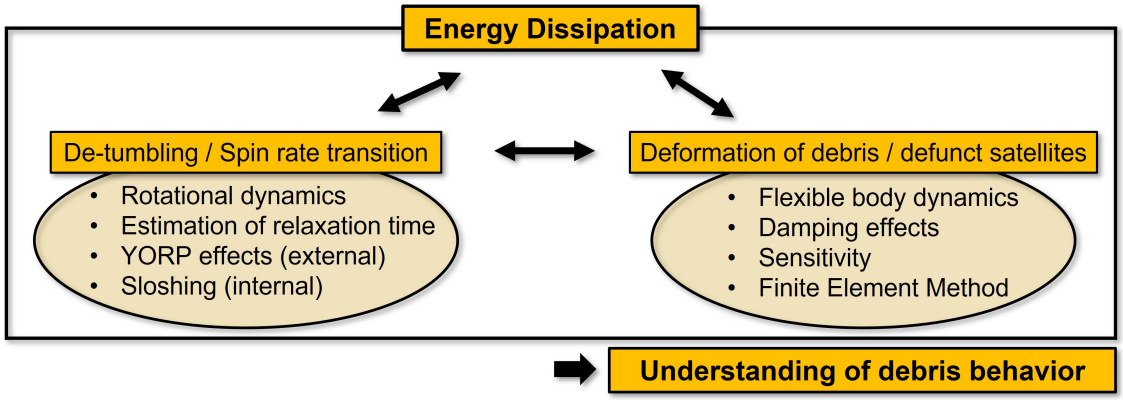

Figure 1.2: Research Area

Figure 1.3 indicates the structure of this thesis and approaches to explore internal energy dissipations. There are two levels of this topic. The first is modeling with a simple satellite model and the second is applications to actual project models with adjusting physical parameters. Firstly, using a simple satellite with flexible appendages, energy dissipations of a tumbling body are modeled. Using FEM theories, an analysis model is developed. The model has a rigid body main component and flexible solar panels. By adding three dimensional acceleration to this model, tumbling motion and deformation are simulated. In combination with the FEM and flexible body theory, the inertia matrix and the time derivative of the inertia matrix can be updated. Different spin rates, tumbling parameters, and the damping ratio are evaluated with numerical simulations.

For the advanced level, I develop another analysis model with FEM based on GOES 10 parameters from open source. By considering the sloshing effects on the de-tumbling, a deformation model is compared and both cases are applied into the GOES model. Through these explorations, I will discuss the variations of behaviors and estimations of relaxation times of tumbling. The goal of this research is to present an effective model for simulating energy decay and spin rate transition with the change in damping effects of defunct satellites. This detailed full-body dynamics

simulation provides an estimation of the de-tumbling and energy loss process without using a full FEM application software.

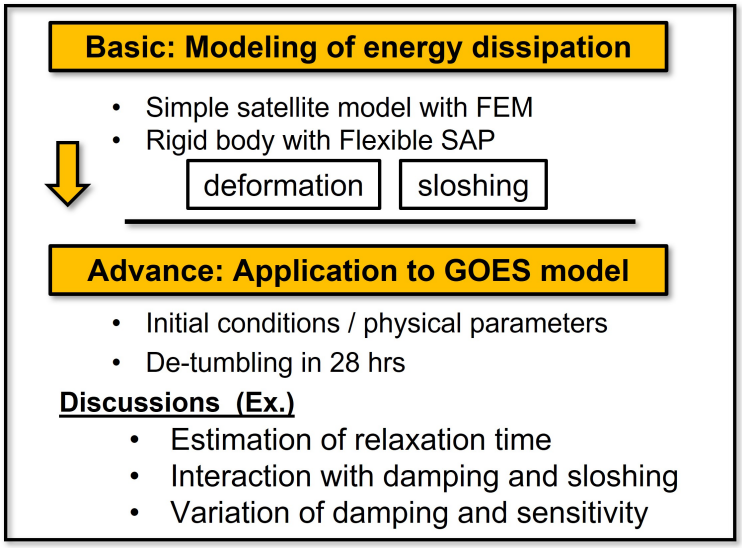

Figure 1.3: Structure of Thesis

Journal

- Tanaka H., and Sakamoto, R.,Effects of vibration characteristics on improvement of deployment repeatability by vibration, Aerospace Science and Technology, 84, 839-844, 2019
- Sakamoto R., Scheeres D.J., and Tanaka H., Modeling Energy Dissipation in a Tumbling Satellite, in preparation

Conference

- Sakamoto R., and Scheeres D.J., Modeling Energy Dissipation in a Tumbling Defunct Satellite using a Finite Element Method, 19th Advanced Maui Optical and Space Surveillance Technologies Conference, Sept. 11-14, 2018.
- Sakamoto R., and Scheeres D.J., Modeling Energy Dissipation and Deformation in a Tumbling Defunct Satellite using a Finite Element Method, 20th Advanced Maui Optical and

Space Surveillance Technologies Conference, Sept. 17-20, 2019.

- Sakamoto R., and Scheeres D.J., Analyzing the Stabilization of a Tumbling Satellite using a Finite Element Method, 70th International Astronautical Congress (IAC),Washington DC, Oct. 21-25, 2019.

- Sakamoto R., and Scheeres D.J., Modeling Effective Control of Satellite Oscillations using a Finite Element Method, 43rd Annual AAS Guidance, Navigation and Control Conference, Breckenridge, CO, Jan.30 - Feb.5, 2020.

- Sakamoto R., and Scheeres D.J., Modeling Internal Energy Dissipation in a Tumbling Defunct Satellite using a Finite Element Method, AAS/AISS Astrodynamics Specialist Virtual Conference, South Lake Tahoe, CA (online), Aug. 9-13, 2020

- Sakamoto R., and Scheeres D.J., De-tumbling Analysis of Unused Satellite with Flexible Appendages, The 31st Astrodynamics Symposium, Japan (online), July. 26-27, 2021.

- Sakamoto R., and Scheeres D.J., Modeling Energy Dissipation and De-tumbling of a Defunct Satellite using a Finite Element Method, 22nd Advanced Maui Optical and Space Surveillance Technologies Conference, Sept. 14-17, 2021.

- Sakamoto R., and Scheeres D.J., Analyzing Defunct Satellite De-tumbling using a Finite Element Method, The 33rd International Symposium on Space Technology and Science, Japan, (online) Feb.26 - March 4, 2022

Presented as a member of Japan Air Self Defense Force

- Sakamoto R., and Sakamoto N., Test on the New SSA System of JASDF, 22nd Advanced Maui Optical and Space Surveillance Technologies Conference, Sept. 14-17, 2021.

1.5 Thesis Statement

It is required to understand the dynamics of non-cooperative objects which have technical difficulties in the crowded orbit region. Modeling defunct satellites with a detailed structure which clarify the relationship between internal energy dissipation and spin rate transitions can contribute to the unraveling of the de-tumbling of space debris. Accurate modeling of energy dissipation and estimation of the dynamics behavior provides benefits for debris mitigation, docking techniques, and space situational awareness.

Organization

Following this introduction, basic modeling of energy dissipations and their numerical simulations are discussed in chapter 2 and 3, respectively. In chapter 2, starting with basic FEM theories and its related dynamics are introduced. There are two main equations to model energy dissipation with flexibility in a space body, that is the damping equation and rotational dynamics. By developing an acceleration matrix, tumbling is simulated. The analytical background of energy dissipations is also explained in chapter 2. Numerical simulations and its analysis of energy dissipations are demonstrated in chapter 3. In chapter 4, using sloshing theories and GOES 10 parameters, verifications of energy dissipation modeling is conducted. And founding are leveraged for sensitivity in chapter 5. As for structural dynamics, sensitivity is an important analysis process and effects on the behaviors of energy dissipations are explored. Finally, finding and summaries are described in the conclusion.

Chapter 2

Modeling of Energy Dissipation

2.1 Structural Model for Investigation

2.1.1 Model Design

In this section, the basis of the FEM analysis is introduced briefly. FEM is an effective tool to evaluate the dynamical behavior of a structure with given material properties [35]. I designed a simple satellite model with displacement-based FEM, which calculates the displacements of the structural nodes. Figure 2.1 shows a simple beam and triangular element with six DOF. $\bar{X}$, $\bar{Y}$, and $\bar{Z}$ is the global (body) frame. x, y, and z is the local (node) frame. Nodes of elements are denoted by l, m, and n. Each node has local displacements (u_i, v_i, and w_i) and rotational angle between of them (θ_{xi}, θ_{yi}, and θ_{zi}), and i denotes the node. Generally, individual elements are formed in a local frame, which is element based at first, and then are transformed to the global (body) frame and assembled for the entire mass and stiffness matrices. Transformations from local to global is described in Appendix A.1.

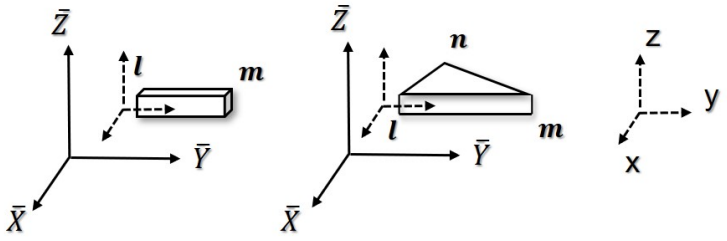

Figure 2.1: Beam and Triangular Element, $\bar{X}\bar{Y}\bar{Z}$: Global (Body) Frame, xyz: Local (Node) Frame

For a triangular element, the nodal displacement vector at one node is defined as

$$\vec{d_e} = \begin{bmatrix} u_i \\ v_i \\ w_i \\ \theta_{xi} \\ \theta_{yi} \\ \theta_{zi} \end{bmatrix}, (i = l, m, n) \tag{2.1}$$

Characteristics of triangular elements are designed by the combination of bending theory based on Discrete Kirchhoff Triangle (w_i, θ_{xi} and θ_{yi}), membrane element with the Constant Strain Triangular (CST) theory (u_i and v_i), and drilling DOF theory (θ_{zi}) [6, 22, 19, 34]. Here, Kirchhoff theory assumes that planes perpendicular to the mid-surface will remain plane and perpendicular to the deformed mid-surface. CST assumes that the strain does not vary within the element [48]. Since one node has six DOF, one triangular element has eighteen total degrees of freedom.

2.1.2 Mesh Effectiveness

This section discusses the effectiveness of the number of the elements to model dynamical behavior. Modal shape is verified with simple plate based on modal shape. Using the basic definition, the mass and stiffness matrices are developed [34]. Figure 2.2 shows a comparison of modal shapes using different computational resolutions and packages. In the top two rows of the figure, the black lines are the original position and the blue lines are the deformations. The displacements are scaled to clearly depict the deformation. The branch node matrix method is used to show this figure [52]. The top row uses a coarse mesh and the middle row uses a finer mesh. The bottom row shows a model computation from the FEM simulation software, Abaqus. Table 2.1 shows simulation parameters of the comparison of shapes. Table 2.2 indicates the comparison of natural frequencies of the results. Although the first frequencies differ, the modal shapes are same for all cases. These simulations are not sensitive to the precise value of the frequencies, and thus the coarser mesh is used for the current results.

Table 2.1: Simulation Parameters of Modal Shapes

Parameters	Value
Length [m]	2×3
Thickness [m]	0.01
Density [kg/m^3]	0.01
Modulus of elasticity [GPa]	1.0
Poisson ratio	0.3

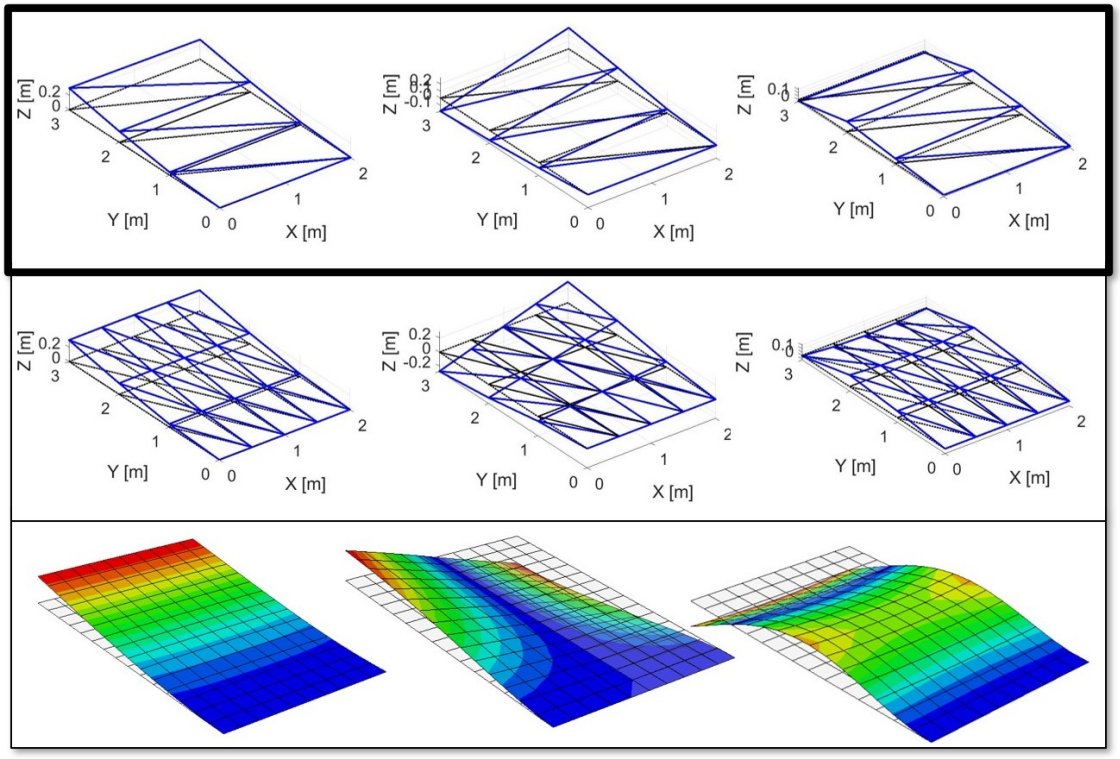

Figure 2.2: Modal Shapes Top: coarse mesh, Middle: fine mesh, bottom: FEM Abaqus

Table 2.2: Natural Frequencies [Hz]

	1^{st}	2^{nd}	3^{rd}
Matlab (1×3)	3.538	6.103	10.51
Matlab (4×3)	1.833	6.153	11.17
Abaqus (FEM Software)	1.849	6.238	11.61

2.1.3 FEM Analysis Model

Using FEM fundamentals and triangular elements, developed a three dimensional analysis model is developed as shown in Figs. 2.3 and 2.4. Figure 2.3 shows an overview of the model. Figure 2.4 shows the details of the model and the associated setups used for our Matlab simulation. This typical satellite model is composed of a rigid main component and two SAP. The black dot indicates the center of mass, and the arrows stand for the body frame. The circled numbers denote the node numbers. To simulate an interaction of a rigid component and flexible components, aluminum is used for the rigid body component, and CFRP (Carbon Fiber Reinforced Plastics) is used for the panel components. In addition, aluminum modulates the total weight of the analysis model. To enable large scale fluctuation behavior, joint elements motivated by beams are introduced between each SAP component. These parameters are shown in Tabs 2.3 and 2.4 [51, 34]. Although CFRP has a larger value of elasticity, in this work, I assumes that the elasticity is set as less than as usual. This is because I assume that quasi isotropic parameters of CFRP and the bending stiffness dominates over isotropic and axial elasticity in this simulation. The size of the main body is 1.0 [m] (X direction) × 1.0 [m] (Y direction) × 0.5 [m] (Z direction). The total model size of the satellite is 1.0 [m] (X direction) × 5.0 [m] (Y direction) × 0.5 [m] (Z direction).

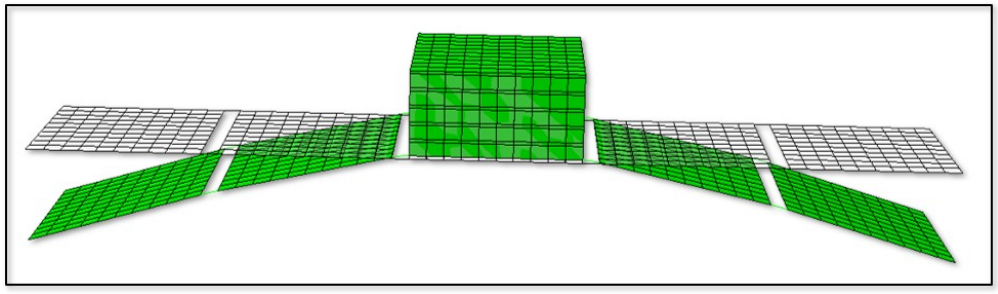

Figure 2.3: Analysis Satellite Model (Overview)

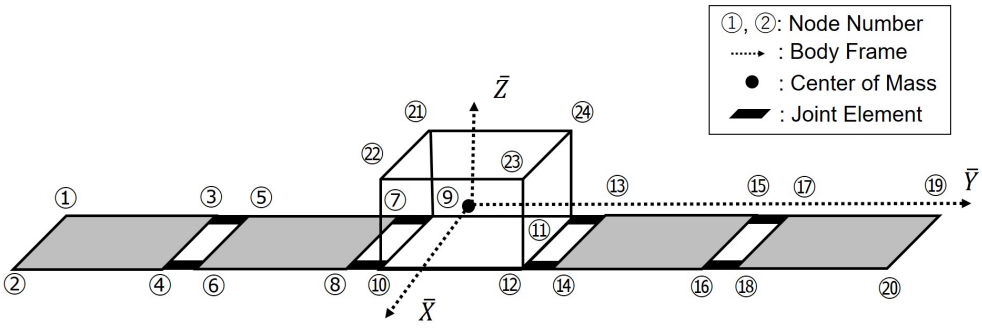

Figure 2.4: Analysis Satellite Model

2.2 Dynamics Model with FEM

For this study, I combine a mass-spring-damper equations to model the flexible structure, and I track the rotational dynamics of the flexible body accounting for the time variation in its inertia tensor. By combining these equations, we have a closed system that couples the deformation and angular velocities, allowing us to track the satellite behavior as it dissipates energy.

2.2.1 Dynamical Equation for FEM

For this simulation, the spring-mass-damper equation (Eq. 2.2) is used to investigate the dynamical behavior of the structure.

$$M\ddot{X} + C\dot{X} + KX = \vec{f}(t) \tag{2.2}$$

where M is the mass matrix, C is the damping matrix, K is the stiffness matrix, and $\vec{f}(t)$ is the excitation force. Here, the over dot is used for the time derivative. With basic definitions, the

Table 2.3: Parameters of the Plate Component (Aluminum, CFRP)

Parameters	Value (Aluminum)	Value (CFRP)
Thickness [cm]	10.0	1.00
Density [kg/m^3]	2.86 $\times 10^3$	1.60 $\times 10^3$
Modulus of elasticity [GPa]	70.0	10.0
Poisson	0.3	0.3

mass and stiffness matrices are developed from the FEM [34]. For numerical efficiency, the mass matrix is taken as a lumped mass matrix, which is a diagonal matrix [17]. The damping equation is in second order differential form and can be transformed into a first order form with $X = X_1$, $\dot{X} = X_2$ as shown in Eq. 2.3.

$$\begin{bmatrix} \dot{X}_1 \\ \dot{X}_2 \end{bmatrix} = \begin{bmatrix} 0 & I_{n\times n} \\ -M^{-1}K & -M^{-1}C \end{bmatrix} \begin{bmatrix} X_1 \\ X_2 \end{bmatrix} + \begin{bmatrix} 0 \\ M^{-1} \end{bmatrix} \vec{f}(t) \tag{2.3}$$

where $I_{n\times n}$ is the identity matrix with size of $n \times n$. As discussed above, each node has six DOF, thus the size of X_1 and X_2 will be $6N \times 1$ ($N = 1, 2, 3...$), where N indicates the number of nodes.

2.2.2 Damping Matrix

The Rayleigh damping model has been widely used to model the time history of structural response, thus I used this model in the study [5]. As shown in Eq. 2.4, the damping matrix has proportional terms to the unit-less mass and stiffness matrices.

$$[C] = \alpha[M] + \beta[K] \tag{2.4}$$

α and β are coefficients and given by following.

$$\alpha = \zeta \frac{2\omega_i\omega_j}{\omega_i + \omega_j},\ \beta = \zeta \frac{2}{\omega_i + \omega_j} \tag{2.5}$$

where ζ is a damping ratio and ω_i and ω_j are i^{th} and j^{th} natural frequencies of the system. Damping properties are frequency dependent functions. Although we can set damping ratios ζ_i and ζ_j differently, we assume the damping ratio ζ is the same at the i^{th} and j^{th} mode frequencies

Table 2.4: Parameters of the Joint Component

Parameters	Value
Area [cm^2]	5.0 × 5.0
Length [cm]	5.0
Density [kg/m^3]	2.86 ×10^3
Modulus of elasticity [Pa]	500

for this study. Since damping ratio make a differential behavior, the variation of ζ and its effects are explored in our simulation.

2.2.3 Acceleration Matrix

In order to simulate a tumbling body, a three dimensional acceleration matrix in the body frame is developed. This acceleration matrix is applied into Eq. 2.2 as an excitation force. An arbitrary angular velocity vector $\vec{\omega}$, is defined as the angular velocity of the body frame relative to the inertial frame. Then, using transport theorem, velocity vectors in the inertial frame are given by

$$^I\frac{d}{dt}\vec{r} = ^B\frac{d}{dt}\vec{r} + \vec{\omega} \times \vec{r} \tag{2.6}$$

$^I\frac{d}{dt}$ denotes the inertial derivative, $^B\frac{d}{dt}$ denotes the time derivative in the body frame, and $\vec{r}$ denotes position vector in the body frame. Furthermore, the acceleration vector in the inertial frame is given by

$$^I\ddot{\vec{r}} = ^B\ddot{\vec{r}} + 2\vec{\omega} \times ^B\dot{\vec{r}} + \dot{\vec{\omega}} \times \vec{r} + \vec{\omega} \times \vec{\omega} \times \vec{r} \tag{2.7}$$

Superscript I denotes the inertial derivative, and B denotes the time derivative in the body frame. Details are in Appendix B.1. Because there are no additional forces in the inertial frame, $^I\ddot{\vec{r}} = 0$, leading to the forcing accelerations in the body-frame:

$$^B\ddot{\vec{r}} = -\vec{\omega} \times \vec{\omega} \times \vec{r} - \dot{\vec{\omega}} \times \vec{r} - 2\vec{\omega} \times ^B\dot{\vec{r}} \tag{2.8}$$

Due to the small velocities of the components relative to the body frame, the Coriolis acceleration term is ignored. The verifications of Coriolis are demonstrated in simulations as well. Then, with

some mathematical developments, the acceleration matrix in the body frame can be given by

$$\vec{f}(t) = [\omega^2 I_{3\times 3} - \vec{\omega}\vec{\omega} - \dot{\tilde{\vec{\omega}}}] \cdot \vec{r} \tag{2.9}$$

where $\sim$ denotes a skew-symmetric matrix.

$$\tilde{\omega} = \begin{bmatrix} 0 & -\omega_3 & \omega_2 \\ \omega_3 & 0 & -\omega_1 \\ \omega_2 & \omega_1 & 0 \end{bmatrix} \tag{2.10}$$

Figure 2.5 illustrates a position vector $\vec{r}$ of node 1 in the body frame. As mentioned before, FEM simulation provides the displacements vector $\vec{d}'s$ from the original position, modeled by Eq. 2.2 in the body frame. Thus, the actual position of a node $\vec{r}$ in the body frame is defined by the nominal node position plus its displacement vector.

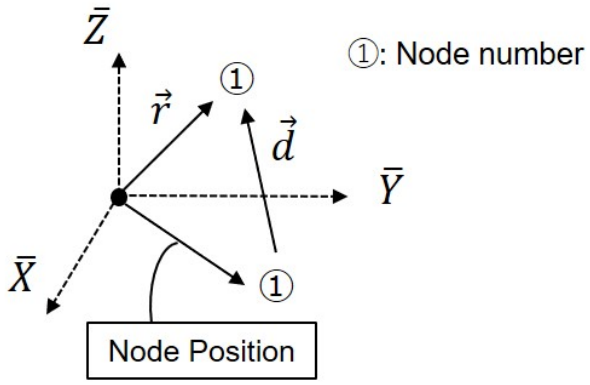

Figure 2.5: Vector Configuration

2.3 Hysteresis

In terms of the energy dissipation, one solution to analyze the level of the damping and energy loss is to determine the area within the hysteresis loop [43]. This sections briefly demonstrates this approach. The Bouc-Wen model has been widely used to show the nonlinear hysteretic systems and its energy dissipation. Bouc originally proposed this model, and it has been generalized by Wen and other researchers [10, 56]. This model is composed of the restoring force and deformation through

a nonlinear differential equation, which has unknown parameters. By changing these parameters, a large variety of different shapes of the hysteresis loops are generated [43, 53]. For example, with the simple dynamics as

$$m\ddot{x}(t) + c\dot{x} + F(t) = f(t) \tag{2.11}$$

where m is the mass, $x(t)$ is the displacement, c the damping coefficient, $F(t)$ is the restoring force, and $f(t)$ is the excitation force. It is assumed that the excitation force is cyclic. The Bouc-Wen model is described by the following differential equation:

$$\dot{g}(t) = A\dot{x}(t) - \beta|\dot{x}(t)||g(t)|^{n-1}g(t) - \gamma\dot{x}(t)|g(t)|^{n} \tag{2.12}$$

where g is an imaginary hysteretic displacement, $A(>0)$, γ, β and n are dimensionless quantities controlling the hysteresis shape and size. From the definition, n is integer and positive values, and β is a positive number. For structural dynamics, the hysteresis loop is caused by the restoring force and structural deformation. However, from FEM simulation, which total restoring force as $F = KX$, and total displacement as $\sum_{i=1}^{N} \vec{d}_i$, $(i = 1, 2, ...N)$ have complex shape as shown in Fig. 2.6. To achieve an analytical results, hysteresis needs transformation to simple shape. Due to this simplification process of simulations and it might eliminate accuracy of energy dissipation, the Bouc-Wen model is not applied in this thesis.

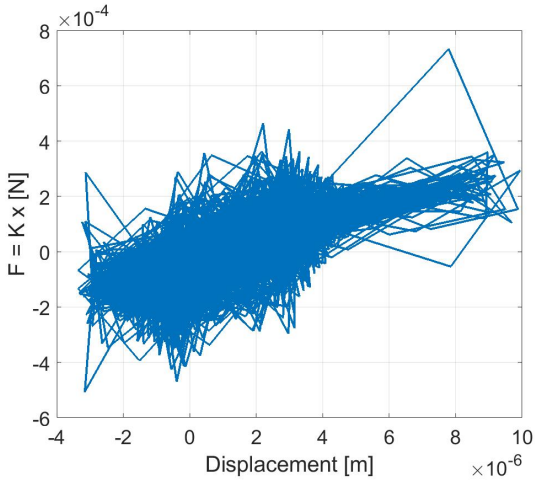

Figure 2.6: Hysteresis with FEM Results

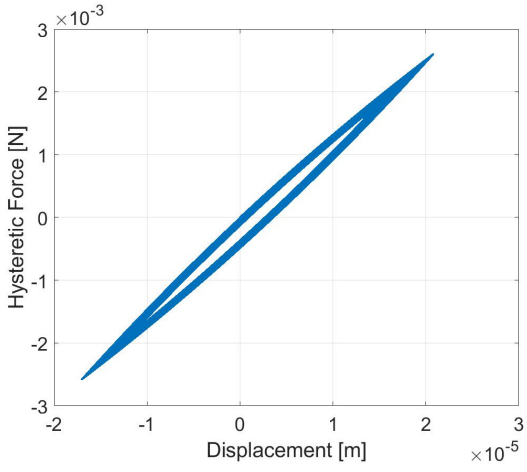

Figure 2.7: Hysteresis with Simplification

2.4 Dynamical Parameters of Rigid and Flexible Body

In this section, the rotational dynamics of a flexible body in the context of my model is developed.

2.4.1 Rigid and Flexible Body Dynamics

Firstly, the definition of rotational angular momentum vector of a single rigid body is defined as,

$$\vec{H} = [I_0]\,\vec{\omega} \tag{2.13}$$

where $[I_0]$ is a constant inertia matrix if the body is rigid. $\vec{\omega}$ is the angular velocity vector of the body fixed frame with respect to an inertial frame [30]. Since the magnitude of angular momentum is constant, this allows us,

$$H^2 = \vec{H}^T\vec{H} = constant \tag{2.14}$$

Assuming that there are no exogenous moments or forces acting on the body, the rigid body rotational equation of motion are defined in a body-fixed frame as

$$[I_0]\dot{\vec{\omega}} \ = -\tilde{\vec{\omega}}[I_0]\vec{\omega} \tag{2.15}$$

For a flexible body, the inertia matrix is a function of time $[I(t)]$. Then the time derivative of the inertia matrix $[\dot{I(t)}]$ must also be considered, and the rotational equations of a flexible body is given by

$$[I(t)]\dot{\vec{\omega}} \ = -\tilde{\vec{\omega}}[I(t)]\vec{\omega} - [\dot{I(t)}]\vec{\omega} \tag{2.16}$$

Generally, the inertia matrix for a rigid body using our lumped mass model is given by,

$$[I_0] = -\sum_{i=1}^{N} m_i\tilde{\vec{r}}\tilde{\vec{r}} \tag{2.17}$$

where N is the number of nodes, and m is a mass. Then the time derivative of Eq. 2.17 is then,

$$[\dot{I(t)}] = -\left(\sum_{i=1}^{N} m_i\dot{\tilde{\vec{r}}}\tilde{\vec{r}} + \sum_{i=1}^{N} m_i\tilde{\vec{r}}\dot{\tilde{\vec{r}}}\right) \tag{2.18}$$

It is assumed that the mass of the entire system is conserved. Figure 2.8 illustrates vector configurations of a part of the simple satellite model. Here, a mass of area with node 9, 10, 11, and 12 is distributed for the four nodes. All displacements and velocities of partial mass are taken into Eq. 2.18 during our simulation.

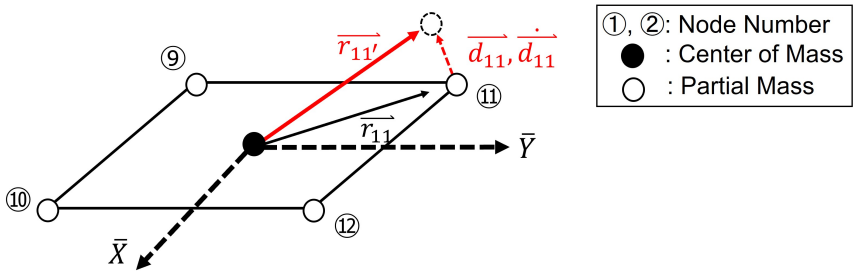

Figure 2.8: Vector Illustration of Part of the Satellite Model

2.4.2 Modified Rodrigues Parameters (MRP)

To translate the orientation of the model from body frame into inertial frame, The Modified Rodrigues Parameters (MRP) (denoted by σ) and direction cosine matrix $[BN]$ are defined by following equations [30].

$$[BN] = [I_{3\times3}] + \frac{8[\tilde{\sigma}]^2 - 4(1-\sigma^2)[\tilde{\sigma}]}{(1+\sigma^2)^2} \tag{2.19}$$

$$\dot{\sigma} = [(1-\sigma^2)[I_{3\times3}] + 2[\tilde{\sigma}] + 2\sigma\sigma^T]\vec{\omega} = \frac{1}{4}[B(\sigma)]\vec{\omega} \tag{2.20}$$

where $[I_{3\times3}]$ denotes an identity matrix with the size of 3×3. This allows us to transform the total angular momentum into an inertial frame in order to check its conservation.

2.4.3 Dynamic Moment of Inertia and Effective Spin Rate

For the torque free motion of a rigid body, rotational angular momentum and kinetic energy are conserved. The rotational kinetic energy T is defined by,

$$T = \frac{1}{2}\vec{\omega}^T[I]\vec{\omega} \tag{2.21}$$

The principal moments of inertia (possibly time-varying) are denoted by $I_x \leq I_y \leq I_z$. Then the rotational motion can be described with the dynamic inertia I_D and effective spin rates ω_l. These are defined by,

$$I_D = \frac{H^2}{2T} \tag{2.22}$$

$$\omega_l = \frac{2T}{\sqrt{H^2}} \tag{2.23}$$

where H is the magnitude of the angular momentum vector $\vec{H}$. The dynamic inertia I_D must satisfy the condition $I_x \leq I_D \leq I_z$. Also, the kinetic energy T has a limited range for a given angular momentum.

$$\frac{1}{2}\frac{H^2}{I_z} \leq T \leq \frac{1}{2}\frac{H^2}{I_x} \tag{2.24}$$

When subject to internal energy dissipation, the kinetic energy is no longer constant, but has a time rate of change equal to:

$$\dot{T} = \vec{\omega} \cdot I \cdot \dot{\vec{\omega}} + \frac{1}{2}\vec{\omega} \cdot \dot{I} \cdot \vec{\omega} \tag{2.25}$$

$$= -\frac{1}{2}\vec{\omega} \cdot \dot{I} \cdot \vec{\omega} \tag{2.26}$$

which is easily found by substituting for $I \cdot \dot{\vec{\omega}}$ in the rotational equation of motion and simplifying. I note that $\dot{T}$ can increase or decrease as the body undergoes fluctuations, and that it will only lead to a net decrease of kinetic energy if the system has damping present, analyzed later. Conversely, the total angular momentum of the rotating body is conserved, even in the presence of energy dissipation. Thus, the limits on the kinetic energy do not change (except for small oscillations in the moments of inertia) and define the limits that a body's kinetic energy can take on.

Rotation about a body's minimum moment of inertia is the maximum energy state for a given angular momentum. When internal energy dissipation is present, the kinetic energy will decrease and leads the tumbling body's angular velocity vector to asymptotically approach its maximum moment of inertia axis $\bar{Z}$, which is the minimum energy state as

$$T_{min} = \frac{H^2}{2I_z} \tag{2.27}$$

and is the stable final rotational state. When a body reaches this state, the fluctuations in the inertia tensor disappear as each node in the body is only subject to a constant acceleration, eventually leading all oscillations to decay to zero.

2.5 Combined Model

Figure 2.9 shows how the simulation sequence is combined to compute the coupled FEM dynamics with the rotational dynamics. The total state of the body is composed of the FEM state, the angular velocity of the body, and its attitude parameterization using MRPs. These three equations are integrated simultaneously. During this simulation, the inertia matrix $[I(t)]$ and its derivative $[\dot{I(t)}]$ are updated at each time step. This process simulates the interaction between the deformation and its spin rate.

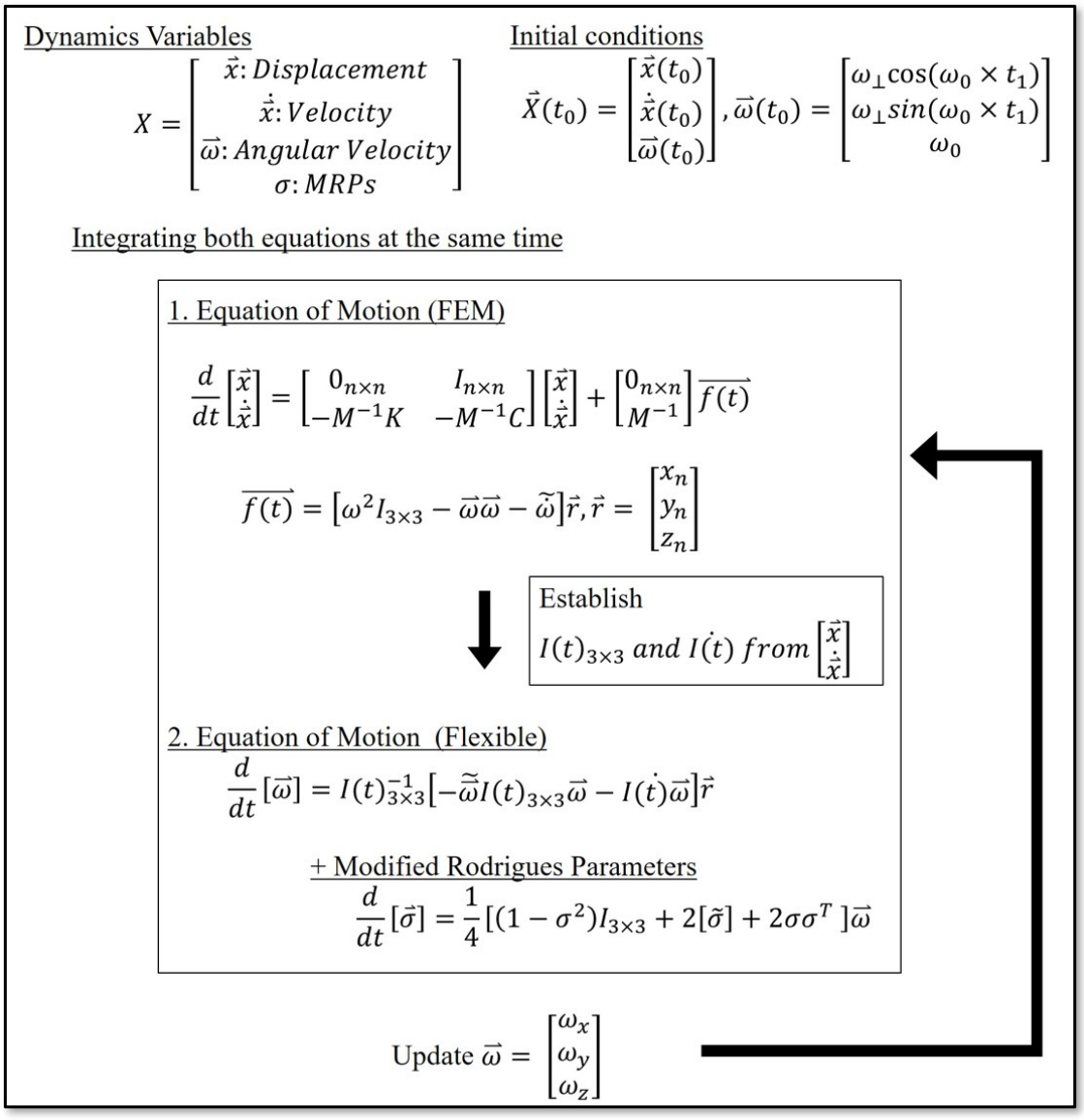

Figure 2.9: Simulation Sequence

2.6 Analytical Background for Energy Dissipation

Before the results of detailed numerical simulations are presented, the key drivers for the overall system energy dissipation dynamics are analyzed. It is instructive to evaluate the internal dynamics that drives the dissipation of energy in the system, and to analyze a simple model motivated by this evolution. This will be used to better interpret and generalize the numerical results presented later in this thesis.

As the body tumbles, its rotational motion will be close to that of a torque-free rigid body, although the time variation of the inertia and the internal loss of energy will cause deviations and the entire spin state to change. However, to enable an analytic discussion these changes are neglected for the moment. In addition, to simplify the analytics the system is modeled as if its inertia has a symmetric axis. This assumption is introduced only for the current discussion to get the general form of the driving dynamics and to enable us to use simpler trigonometric functions for the driving perturbations.

For a FEM model the main mechanical model consists of lumped mass terms, which can ideally be modeled as a mass m_i located by a position $\vec{r_i}$ in the body-frame, in the following the i subscript is suppressed. The full FEM model ties all of these disparate terms together, as explained above, however for the current discussion just a single element is considered along with how the rotational dynamics drive it.

2.6.1 Driving Accelerations

The main time-varying acceleration acting on an element is due to the tumbling motion of the satellite. Derivations are described in Appendix B.2. Let the instantaneous angular velocity of the body in a body-fixed frame be denoted as $\vec{\Omega}$. Then, the rotation matrix is given by $BN =$

$R_3(\sigma t)R_1(\delta)$ where R_i denotes a principal rotation about the i^{th} axis.

$$R_3(\sigma t)R_1(\delta) = \begin{bmatrix} \cos(\sigma t) & \sin(\sigma t)\cos\delta & \sin(\sigma t)\sin\delta \\ -\sin(\sigma t) & \cos(\sigma t)\cos\delta & \cos(\sigma t)\sin\delta \\ 0 & -\sin\delta & \cos\delta \end{bmatrix} \tag{2.28}$$

$\vec{\Omega}$ is expressed with the simplified form due to the symmetric inertia assumption

$$\vec{\Omega} = \omega_l I_D \begin{bmatrix} \frac{1}{I_t}\sin\delta\cos(\sigma t) \\ \frac{1}{I_t}\sin\delta\sin(\sigma t) \\ \frac{1}{I_a}\cos\delta \end{bmatrix} \tag{2.29}$$

where ω_l and I_D have been defined previously, δ is the angle between the body's symmetry axis and the angular velocity, I_t and I_a are moments of inertia perpendicular to and along the symmetry axis, respectively, and σ is the frequency of the angular velocity in the body frame,

$$\sigma = \frac{I_D\,(I_a - I_t)}{I_a I_t}\cos\delta\ \omega_l \tag{2.30}$$

where $\sigma \propto \omega_l$ in general. For definiteness, assume the spacecraft is an oblate body, or $I_a > I_t$, as then the symmetry axis is the final rotation axis and $\delta \to 0$ as energy is dissipated.

The driving acceleration for a mass element in the body frame is

$$\vec{a} = \Omega^2\vec{r} - \left(\vec{\Omega}\cdot\vec{r}\right)\vec{\Omega} \tag{2.31}$$

If the mass element is at a latitude λ in the body-fixed frame the driving acceleration becomes

$$\begin{aligned} \vec{a} = \omega_l^2 I_D^2 r \Bigg\{ & \frac{(\cos^2\delta I_t^2 + \sin^2\delta I_a^2)}{I_t^2 I_a^2} \begin{bmatrix} \cos\lambda \\ 0 \\ \sin\lambda \end{bmatrix} \\ & - \left(\frac{\cos\lambda\sin\delta\cos(\sigma t)}{I_t} + \frac{\sin\lambda\cos\delta}{I_a}\right) \begin{bmatrix} \frac{1}{I_t}\sin\delta\cos(\sigma t) \\ \frac{1}{I_t}\sin\delta\sin(\sigma t) \\ \frac{1}{I_a}\cos\delta \end{bmatrix} \Bigg\} \end{aligned} \tag{2.32}$$

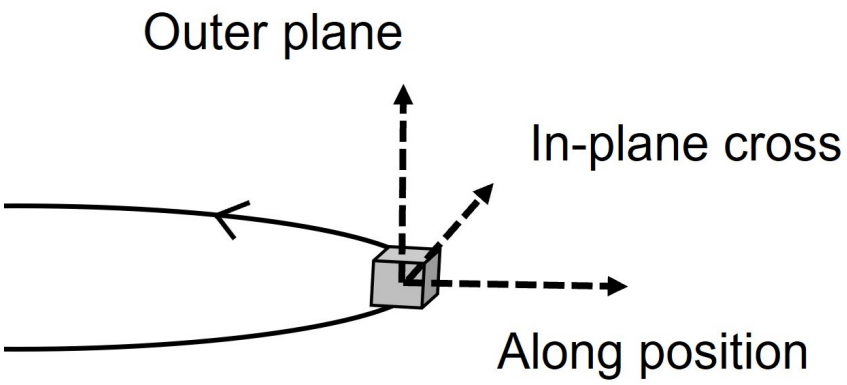

Figure 2.10: Driving Acceleration on an Element

For definiteness, consider the case $\lambda = 0$, which provides clarity on the different ways that the mass element is excited, and simplifies to:

$$\vec{a} = \frac{\omega_l^2 I_D^2 r}{I_t^2} \left\{ \left(\sin^2\delta + \frac{I_t^2}{I_a^2}\cos^2\delta \right) \begin{bmatrix} 1 \\ 0 \\ 0 \end{bmatrix} - \sin\delta\cos(\sigma t) \begin{bmatrix} \sin\delta\cos(\sigma t) \\ \sin\delta\sin(\sigma t) \\ \frac{I_t}{I_a}\cos\delta \end{bmatrix} \right\} \tag{2.33}$$

The along-position acceleration has a constant term plus an oscillatory term with an amplitude $\sin^2\delta$ and a frequency 2σ, the in-plane cross acceleration is oscillatory with a magnitude $\sin^2\delta$ and a frequency 2σ, and the out-of-plane term is oscillatory with an amplitude $\sin 2\delta$ and a frequency σ. Under the assumption that δ is relatively small, the out of plane driving acceleration will be larger than the radial and in-plane terms. As the system dissipates energy the angle $\delta \to 0$, reducing the magnitude of the oscillations and leading to the typical decay in excitation and a prolonged period of dissipation at an ever decreasing rate.

2.6.2 Oscillation Dynamics

For definiteness consider the out-of-plane oscillation of the mass element using a simplified model motivated by the FEM model. Then the driving acceleration will be $a_z = \frac{\omega_l^2 I_D^2 r}{2 I_t I_a}\sin 2\delta\cos(\sigma t)$ and the out-of-plane oscillations are modeled with a simple 2nd order dynamical system

$$\ddot{z} + 2\zeta\omega_o\dot{z} + \omega_o^2 z = a_z \tag{2.34}$$

where z is the out-of-plane coordinate, assumed to be small or $z \ll r$, ζ is the damping ratio of the element, and ω_o represents the natural frequency of the system. I note that in actuality there are multiple natural frequencies present and that the driving frequency tends to be much smaller than the system natural frequencies, or $\omega_o \gg \sigma \sim \omega_l$.

This system can be solved by finding a particular solution and a homogenous solution and summing them. Doing so, with simple initial conditions of $z = \dot{z} = 0$, yields the general solution

$$\begin{aligned} z(t) &= \frac{\omega_l^2 I_D^2 r}{2 I_t I_a} \frac{\sin 2\delta}{(\omega_o^2 - \sigma^2)^2 + 4\zeta^2 \omega_o^2 \sigma^2} \left\{ (\omega_o^2 - \sigma^2) \cos(\sigma\ t) + 2\zeta\omega_o\sigma \sin(\sigma\ t) \right. \\ &\quad \left. - \frac{\zeta}{\sqrt{1-\zeta^2}} e^{-\zeta\omega_o t} (\omega_o^2 + \sigma^2) \sin\left(\omega_o \sqrt{1-\zeta^2}\ t\right) - (\omega_o^2 - \sigma^2) e^{-\zeta\omega_o t} \cos\left(\omega_o \sqrt{1-\zeta^2}\ t\right) \right\} \end{aligned} \tag{2.35}$$

In general the natural frequencies of the body will be larger than the body spin rate, or $\omega_o \gg \sigma$. Thus we note that the overall amplitude of z oscillations is of order ω_l^2 and that of $\dot{z}$ oscillations will be of order ω_l^3 due to the σ term that gets introduced. Additionally, while the explicit exponential terms in the oscillation will damp out relative to the forced oscillations, the amplitude of the forced oscillations will also decrease as $\delta \to 0$, the two effects combining in a more complex way that our FEM code will explicitly model. Derivations of driving acceleration and oscillation dynamics are described in Appendix C.

2.6.3 Kinetic Energy Variations

The oscillation of the mass element will cause the satellite to fluctuate and provides the main conduit for energy dissipation. My simple model allows us to identify the main drivers behind the amplitude of oscillation and the decay behavior. First recall that the time rate of change of the kinetic energy is

$$\dot{T} = -\frac{1}{2} \vec{\Omega} \cdot \dot{I} \cdot \vec{\Omega} \tag{2.36}$$

Next, given the general form of the system inertia matrix

$$I = \sum_i m_i \left[\vec{r_i}^2 U - \vec{r_i}\vec{r_i} \right] \tag{2.37}$$

where m_i is a lump mass, $\vec{r_i}$ is the position of the mass in the body frame, and U is the identity matrix. Evaluating the time rate of change of this quantity and substituting into the equation for the time rate of change of the kinetic energy yields

$$\dot{T} = -\sum_i m_i \left[\vec{r_i} \cdot \dot{\vec{r}_i} \Omega^2 - \left(\vec{\Omega} \cdot \vec{r_i} \right) \left(\vec{\Omega} \cdot \dot{\vec{r}_i} \right) \right] \tag{2.38}$$

If the system has no dissipation, the time variation of the moment of inertia terms will oscillate and not change their amplitude, with the kinetic energy trading with the internal potential energy of the system to keep the energy constant. If dissipation is present, however, the oscillations will decay in amplitude and the kinetic energy will have a decreasing oscillation that will asymptotically decay to a stationary state.

It is important to note that the time rate of change of the kinetic energy is proportional to a few key parameters. Specifically, it can be seen that

$$\dot{T} \propto \Omega^2 \Delta r_i \Delta \dot{r}_i \tag{2.39}$$

where Δr_i and $\Delta \dot{r}_i$ represent the oscillation amplitude of the given position, and we note that $\Omega \propto \omega_l$. As dissipation occurs I expect the overall order of magnitude of ω_l to decrease, but at most by a factor of I_D/I_a. In contrast, I expect the variations Δr_i and $\Delta \dot{r}_i$ to undergo an exponential decrease in amplitude, as the angle δ decays due to dissipation. There is also an expectation that the amplitude of these terms, and hence the overall size of the kinetic energy variations and dissipation rate, to be driven by how large the overall angular velocity of the spacecraft to be. In the following we will study the basic system dynamics that drive this dissipation.

2.6.4 Expected behavior as a function of time

We see that there are multiple oscillation modes present, even in this simplified system. However, the explicit decay in the flexible components occurs through the exponential decay function $e^{-\zeta t}$. Thus, I expect that, all else being equal, the overall system loss of energy should be a function of the product ζt. This is tested in our simulation results by plotting the time decay behavior as a function of this product for different values of ζ, but with the same excitation conditions.

I also note that for a given dissipation coefficient ζ, that the overall spin rate of the spacecraft should also drive the speed with which energy is dissipated. While the overall kinetic energy is scaled by ω_l^2, we also note that the amplitude of oscillations are scaled by $\Delta r\ \Delta\dot{r} \sim \omega_l^5$. The main driver of dissipation is the amplitude of oscillation, which is driven by the overall excitation frequency. Thus, I expect that a larger driving frequency for the tumbling spacecraft will drive a faster dissipation, through both a larger amplitude of motion and through a faster frequency. This is primarily driven by the oscillation in the kinetic energy, which affords an opportunity for the excess kinetic energy to be dissipated. As we have seen above, the variation in the kinetic energy is driven by the variation in the inertia matrix, which consists of terms $\propto \Delta r\ \Delta\dot{r}$ in the different vector directions, which predicts that the overall amplitude and hence dissipation rate should vary approximately as

$$T/\omega_l^2 \propto \omega_l^5 \tag{2.40}$$

which will be verified in the results section.

Chapter 3

Simulations of Energy Dissipation

In this section, the simulation setups and results are demonstrated based on findings and theories which are described above chapters. For the following simulations, first I discuss how deformation affects internal energy dissipation and spin rate transition of the tumbling model. Using their findings, I leverage them for estimation of relaxation times of spinning with the change of damping ratio and spin rates.

3.1 Simulation Sequence and Setups

Figure 2.9 shows the simulation sequence which simulates the interaction between the deformation and the body spin rate. In the following, for context, I also compare the results to a rigid body with a constant inertia matrix. The key initial conditions for our set-up are the node displacements and velocities, which are all set to zero, the attitude, which is initially aligned with the rigid body frame axis, and the angular velocity, which is set as described below.

Although the inertia matrix is updated each time step, the initial matrix $I_0 = I(t_0)$ is computed from the relaxed system, and for our model is defined as

$$I(t_0) = \begin{bmatrix} 21.7633 & 0 & 0 \\ 0 & 15.6146 & 0 \\ 0 & 0 & 31.1428 \end{bmatrix} [kg \cdot m^2] \tag{3.1}$$

Then the overall dynamics and level of excitation of the system is driven by the initial angular

velocity. To be consistent I use the following form

$$\vec{\omega}(t_0) = \begin{bmatrix} \omega_\perp \cos(\Delta\theta) \\ \omega_\perp \sin(\Delta\theta) \\ \omega_0 \end{bmatrix}, \ \omega_\perp = F \times \omega_0 \tag{3.2}$$

where ω_0 is the initial spin rate along $\bar{Z}$ axis component, and $\omega_\perp$ is the perpendicular spin rates with the $\bar{Z}$ axis in the body frame. F is the ratio of the two angular velocities and leads to an excited system when $F > 0$. To enable the transverse spin rate to be projected off-axis we choose a non-zero $\Delta\theta$ for the initial spin state. As mentioned before, FEM simulation provides the displacements vector $\vec{d}'s$ from the original position. Therefore, $\vec{r}$ in the body frame is defined by the node position plus each displacement vector of nodes. For my initial analysis, I use a basic angular velocity vector, given by Eq. 3.3.

$$\vec{\omega}(t) = \begin{bmatrix} \omega_\perp \cos(\omega_0 \times t) \\ \omega_\perp \sin(\omega_0 \times t) \\ \omega_0 \end{bmatrix}, \ \omega_\perp = F \times \omega_0 \tag{3.3}$$

where ω_0 is a spin rate along $\bar{Z}$ axis component, and $\omega_\perp$ is the perpendicular spin rates with the $\bar{Z}$ axis in the body frame. F is the ratio of a pure spin and tumbling, it is the same as the perturbation acting on the pure spin. Based on Eqs. 2.9 and 3.3, the three dimensional acceleration matrix is defined by

$$\vec{f}(t) = \begin{bmatrix} \omega^2 - \omega_\perp^2 \cos^2(\omega_0 t) & -\omega_\perp^2 \sin(\omega_0 t)\cos(\omega_0 t) & -\omega_\perp \omega_0 \cos(\omega_0 t) \\ -\omega_\perp^2 \sin(\omega_0 t)\cos(\omega_0 t) & \omega^2 - \omega_\perp^2 \sin^2(\omega_0 t) & -\omega_\perp \omega_0 \sin(\omega_0 t) \\ -\omega_\perp \omega_0 \cos(\omega_0 t) & -\omega_\perp \omega_0 \sin(\omega_0 t) & \omega^2 - \omega_0^2 \end{bmatrix} \vec{r} \tag{3.4}$$

where, $\omega^2 = \omega_0^2 + \omega_\perp^2$.

3.2 Rigid and Flexible Comparison

Using the parameters, which are shown in Tab. 3.1, simulations comparing a rigid and flexible satellite are conducted and compared. These spin rate parameters are referenced to a specific

project mission [57]. For the simulation, w_i and w_j are set as 0.1 in Eq. 2.5. and F is 1.0 in Eq. 3.3. Figure 3.1 shows the time history of the angular velocities in the body frame. Here blue lines depict results of the rigid body dynamics with a constant inertia matrix, and the red lines depict behaviors of the flexible body dynamics accounting for the deformation. For the rigid body all of the angular velocities remain periodic, as is expected from the torque-free solution. However, for the flexible body case, ω_x and ω_y are seen to damp towards zero, and ω_z approaches a particular value as time goes on. We can see this behavior represented in the polhode plot as shown in Fig. 3.2. Here, the rigid body maintains a fixed, closed curve on the polhode ellipsoid while the dissipating case has a decreasing amplitude in the cross axes and has an increasing spin rate along the z-axis.

As a check on the numerical accuracy of the simulations, the magnitude of the angular momentum is shown in Fig. 3.3. I note that it is constant to within a small deviation for the flexible case. and observe it to be a conserved quantity.

Figure 3.4 shows the kinetic rotational energies of the rigid and the flexible body dynamics. The nominal value of the rigid body theory is constant but the deformation case is decreasing toward the minimum energy state E_{min} following the expected exponential decay.

Table 3.1: Simulation Parameters of Energy Dissipation

Damping	$\zeta = 0.1,$	$w_i = w_j = 0.1$
Spinning	F = 1.0	$\frac{2\pi}{360}$[rad/sec]

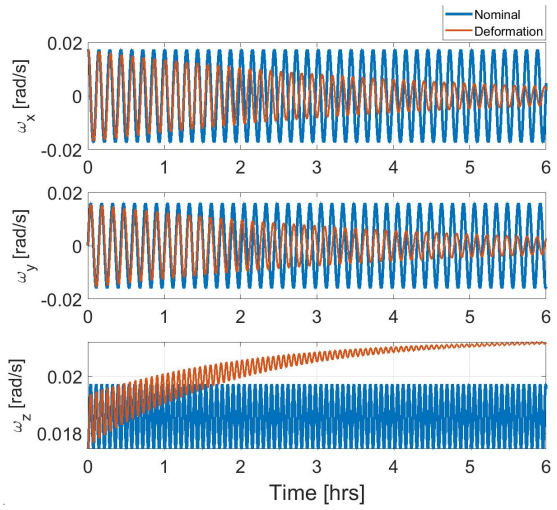

Figure 3.1: Angular Velocities $\vec{\omega}$

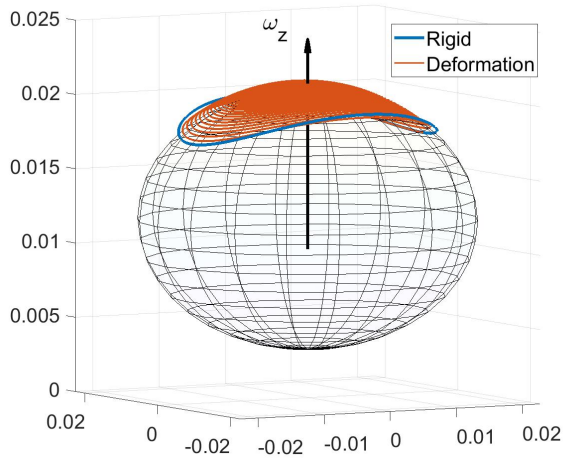

Figure 3.2: Polhode of $\vec{\omega}$

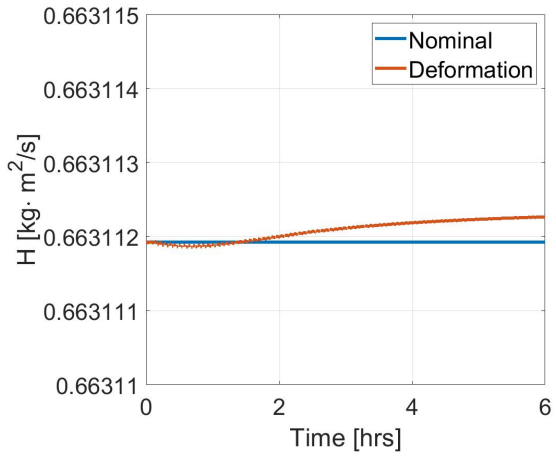

Figure 3.3: Angular Momentum $|\vec{H}|$

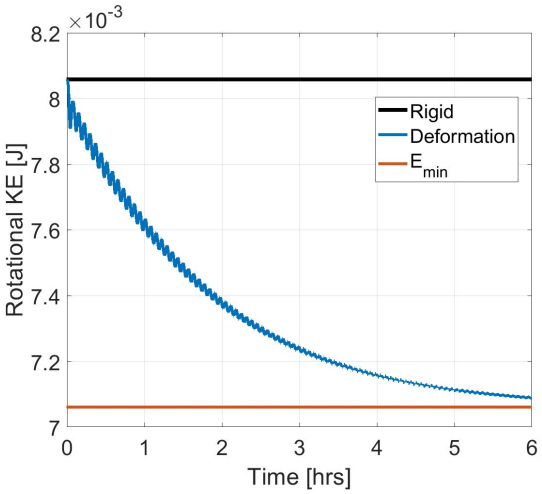

Figure 3.4: Rotational Energy T_{rot}

As an alternate way to track the rotational state of the system, Figures 3.5 and 3.6 show the time history of the effective spin rate ω_l and the dynamic inertia I_D respectively. Similar to the energy decay curve, the dynamic inertia and effective spin rate also change exponentially. In Fig. 3.6, the dynamic inertia is less than the maximum moment of inertia, which is defined as the maximum eigenvalue of the time-varying inertia matrix $I(t)$ (denoted by I_{max}). Due to the fluctuation of the inertia this maximum value fluctuates.

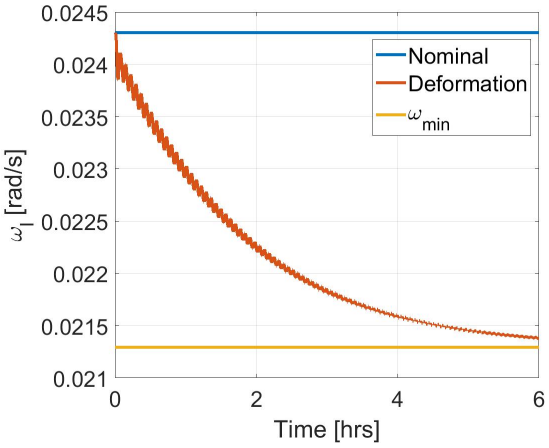

Figure 3.5: Effective Spin Rate ω_l

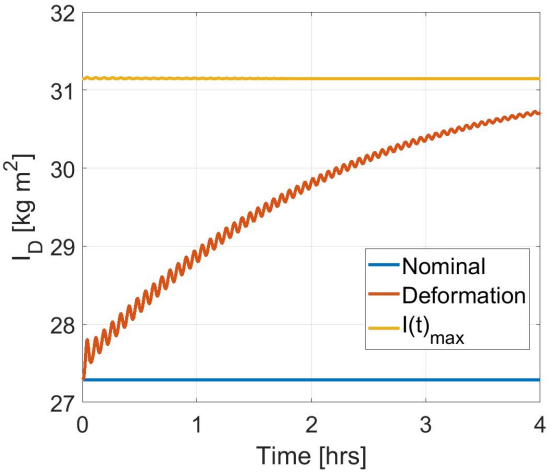

Figure 3.6: Dynamic Inertia I_D

3.3 Coriolis Effects

In this section, the Coriolis effects are explained. In the derivation of acceleration matrix as an excitation force, Coriolis terms $\left(-2\tilde{\vec{\omega}}\dot{\vec{r}}\right)$ is ignored. To check this step, simple simulations are conducted and results are shown in Figs .3.7 and 3.8. These figures compare Coriolis term included or not among energy dissipation. Figure 3.7 indicates time history of $\delta\vec{\omega}$ which shows difference with Coriolis term based on Fig. 3.1. As shown this figure, scale of spin rate along z axis, is 10^{-5}, and the order of expected scale of spin rate is 10^{-2}. In terms of differences of these, we can say Coriolis term is not critical for the numerical simulations. Energy dissipations are occurred within order of 1×10^{-3} in Fig. 3.4, but, as shown in Fig. 3.8, Coriolis term effects are in the order of 1×10^{-6} at the final state. Based on these simulation results, following discussions do not consider

Coriolis term.

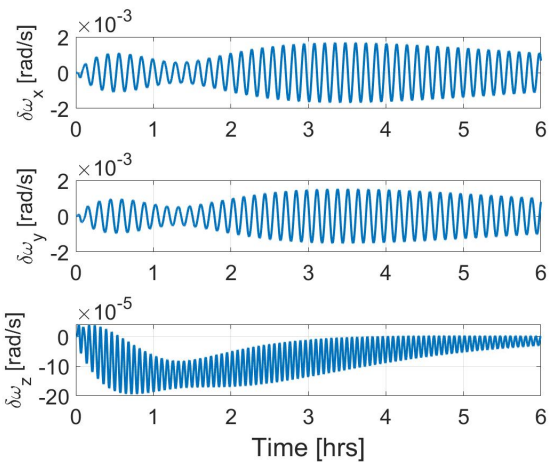

Figure 3.7: Coriolis Effect ($\delta\omega$)

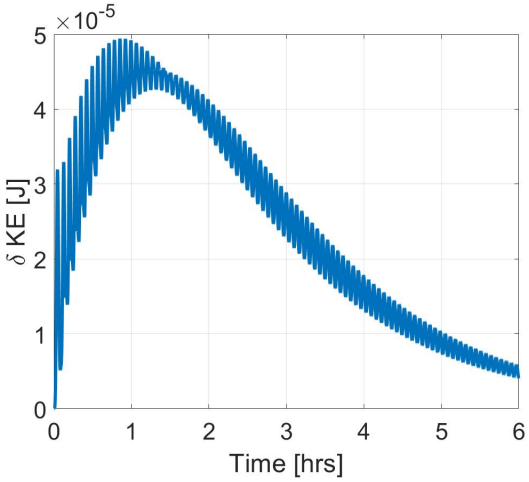

Figure 3.8: Coriolis Effect (δT)

3.4 Parametric Exploration of Energy Loss

To better understand the performance of the model, the variation of satellite parameters and the initial spin state are explored. I find the most critical model parameter to influence the damping behavior is the damping ratio (ζ). Therefore, the relationship between the damping ratio and energy decay curves are investigated. The range of the damping ratios is set to be consistent with a reasonable simulation time, as driving the damping ratio to small values makes the simulation time longer. Next, I explored the relationship between spin rate and shape of energy decay curves with a few different initial spin rates. Finally, I also explored the damping timescale variation as the initial spin state F is modified. Simulation parameters are summarized in Tab. 3.2. Again, $w_i = w_j = 0.1$ is chosen for simulation simplicity.

3.4.1 Variation of Damping Ratio

For a given initial spin rate and state, Fig. 3.9 shows the variation of the energy decay curves with a change in the damping ratio with $\omega_0 = \frac{2\pi}{360}$, corresponding to a 6 minute rotation period. As shown in this figure, energy decay with a weaker damping ($\zeta = 0.01$) requires a longer relaxation

Table 3.2: Simulation Parameter Conditions

Variation	ζ	ω_0 [rad/sec]	F
Damping Ratio (ζ)	$0.01 \sim 0.1$	$\frac{2\pi}{360}$	1.0
Spin Rate (ω_0)	$0.01 \sim 0.1$	$\frac{2\pi}{180}, \frac{2\pi}{360}, \frac{2\pi}{540}$	1.0
Ratio of ω_0 and $\omega_\perp$ (F)	$0.01 \sim 0.1$	$\frac{2\pi}{360}$	$0.1 \sim 2.0$

time. Conversely, a larger damping ratio causes a faster decay in the energy.

Motivated by our analysis, I expect the decay time to be mainly affected by the dissipation parameter used in our model. This can be tested by plotting the energy decay curves using ζt as the independent parameter.

Figure 3.10 shows that plotting the energy as a function of $(Time \times \zeta)$ collapses the different curves. For the other parameters being held constant, I can estimate the longer timescales referencing the faster decays, appropriately scaled. Thus, even given a relatively short and incomplete simulation, the relaxation time can be estimated along the exponential function as like Fig. 3.11. Figure 3.12 shows computational time of each simulation via MATLAB. Each color matches with Fig. 3.11, and the time step is 0.1 s. For the case of $\zeta = 0.01\,(5days)$, due to the limit of simulation storage, calculation was terminated before 1 hour elapsed. From these comparison, finding energy decay shapes is an essential approach to save computational time.

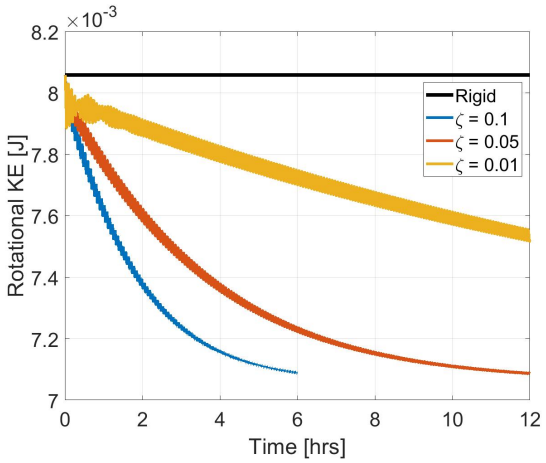

Figure 3.9: Energy Decay with $\omega_0 = \frac{2\pi}{360}$

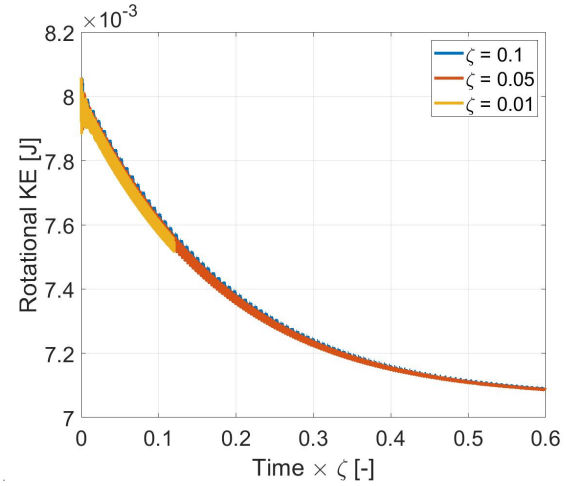

Figure 3.10: Energy with Time $\times\zeta$ $\left(\omega_0 = \frac{2\pi}{360}\right)$

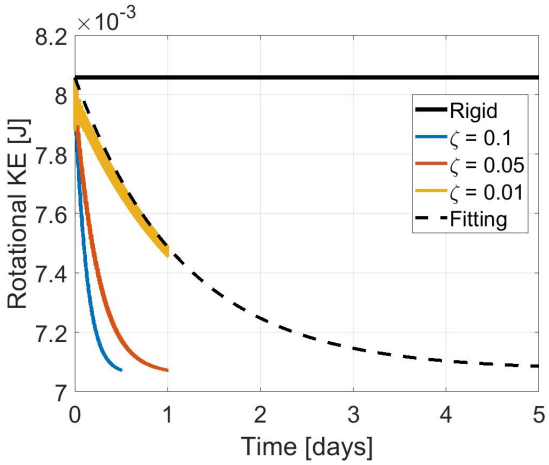

Figure 3.11: Estimation of Energy Decay

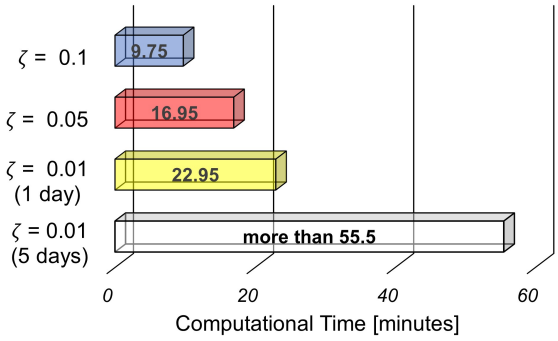

Figure 3.12: Computational Times $\left(\omega_0 = \frac{2\pi}{360}\right)$

3.4.2 Variation of Spin Rate

Figures 3.13 and 3.14 show the plots of energy state with a changing damping ratio and different spin rates. Of course, if the system has a different spin rate, then the kinetic energy and its decay rate is also expected to be different. From these figures, we note that faster spin rates lose energy more quickly. Also as in the previous section, we can see the general shape of the decay curves collapse for a given spin rate when scaled by $(Time \times \zeta)$ as shown in Figs. 3.15 and 3.16 for different spin rates from $\frac{2\pi}{540} \sim \frac{2\pi}{180}$.

As demonstrated above, energy dissipation curves all follow the exponential functions such as $y = \Delta E e^{-\lambda t}$. For these different cases the λ values of each case are summarized in Tab. 3.3. Here we note significant variations in these relaxation times across the parameters.

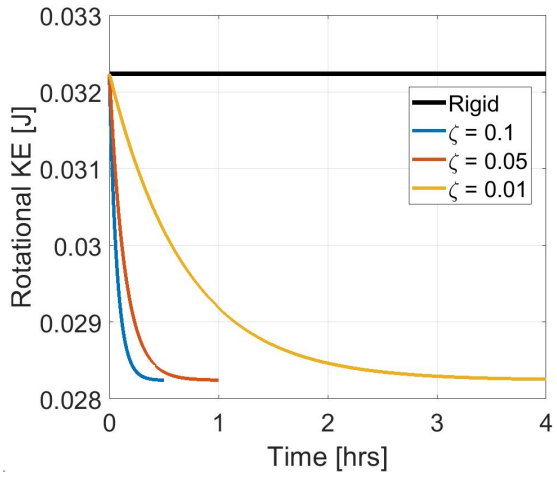

Figure 3.13: Energy Decay with $\omega_0 = \frac{2\pi}{180}$

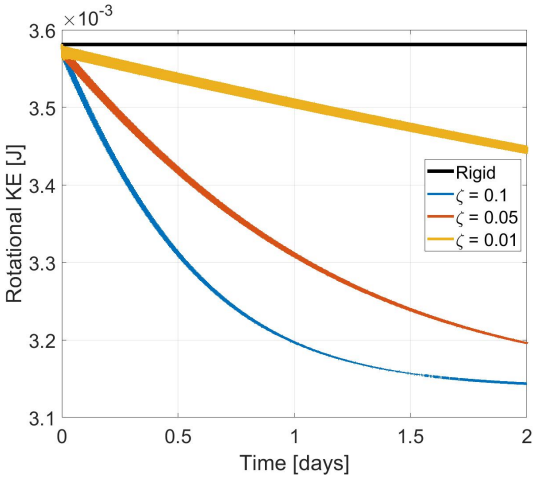

Figure 3.14: Energy Decay with $\omega_0 = \frac{2\pi}{540}$

Motivated by the analytical discussion, I expect that these different time behaviors can be scaled to a single parameter for this case, as the only difference is the dissipation parameter and the initial spin rate, as the initial tumbling state is held constant with $F = 1$. The relationship in Eq. 2.40 suggests that the energy can be scaled by ω_0^2 and the time scaled by ω_0^5.

Doing so I find the tendency of the variations to be $\lambda = \alpha\zeta\omega_0^5$, $\alpha = 10^6$ as shown in Tab. 3.4 and Fig. 3.17. Then, given one computation of the relaxation time it can be scaled to other

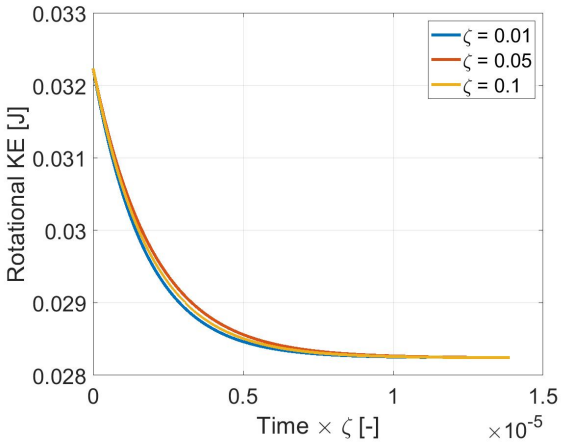

Figure 3.15: Energy with Time $\times\zeta$ $\left(\omega_0 = \frac{2\pi}{180}\right)$

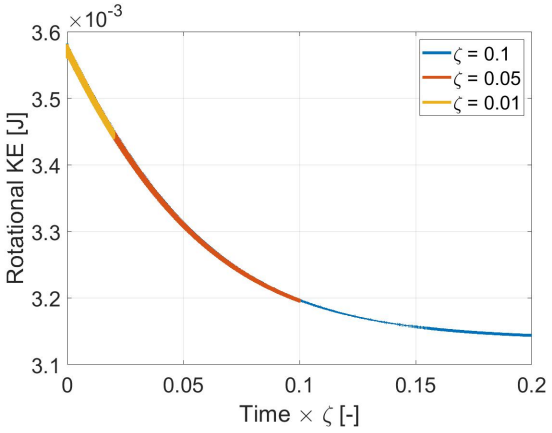

Figure 3.16: Energy with Time $\times\zeta$ $\left(\omega_0 = \frac{2\pi}{540}\right)$

parameter values as specified. This shows that the analysis appropriately identified the driving conditions, and enables the extension of simulations at higher dissipation rates to be scaled to low dissipation and spin rates, which may be more impractical to compute.

Table 3.3: Variations of λ [1/s]

$\zeta \setminus \omega_0$	$\frac{2\pi}{180}$	$\frac{2\pi}{360}$	$\frac{2\pi}{540}$
0.01	$4.0e^{-4}$	$1.6e^{-5}$	$2.0e^{-6}$
0.05	$2.0e^{-3}$	$8.0e^{-4}$	$1.1e^{-5}$
0.1	$4.0e^{-3}$	$1.6e^{-4}$	$2.1e^{-5}$

Table 3.4: Variations of $\frac{\zeta\omega_0^5}{\lambda}$

$\zeta \setminus \omega_0$	$\frac{2\pi}{180}$	$\frac{2\pi}{360}$	$\frac{2\pi}{540}$
0.01	$1.30e^{-6}$	$1.01e^{-6}$	$1.06e^{-6}$
0.05	$1.30e^{-6}$	$1.01e^{-6}$	$9.7e^{-7}$
0.1	$1.30e^{-6}$	$1.01e^{-6}$	$1.02e^{-6}$

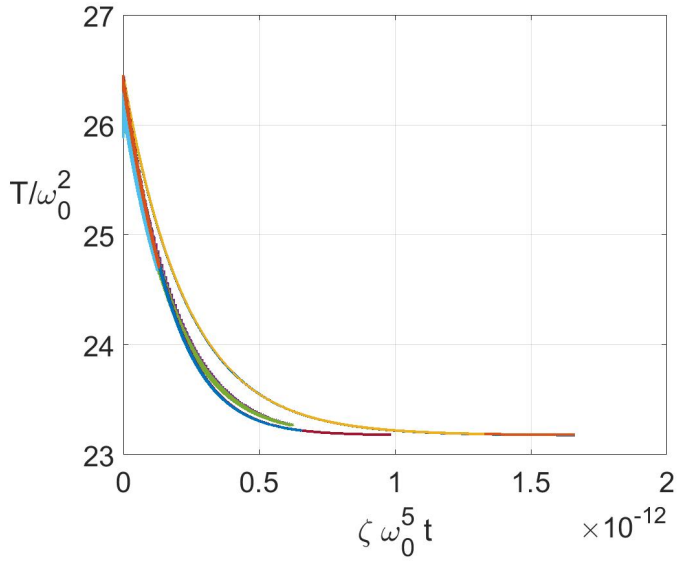

Figure 3.17: Scaled Energy Curves Collapse to a Single Profile

3.4.3 Variation of F

I also explored the effects of varying the F parameter on the energy decay curves with two cases for initial spin conditions. Variation in F causes the rigid body to start at different levels of excitement. First I vary F while keeping the angular velocity magnitude $|\vec{\omega}|$ constant. Next I keep the magnitude of angular momentum $|\vec{H}|$ constant.

To keep the total angular velocity constant as F varies, the initial value of ω_0 is modulated to keep same angular velocity.

$$\vec{\omega}(t_0) = \begin{bmatrix} \omega_\perp \cos(\Delta\theta) \\ \omega_\perp \sin(\Delta\theta) \\ \omega_0 \end{bmatrix} = \omega_0 \begin{bmatrix} F\cos(\Delta\theta) \\ F\sin(\Delta\theta) \\ 1 \end{bmatrix}, \tag{3.5}$$

For a given F the initial angular velocity magnitude is $|\vec{\omega}| = \omega_0\sqrt{1+F^2}$. Thus at $F = 1$, $|\vec{\omega}| = \omega_0\sqrt{2}$. To keep this value constant for different values of F, we must choose a new spin rate $\omega_0' = \omega_0\sqrt{2}/\sqrt{1+F^2}$. Thus if $F = 0.1$, the initial spin rate $\omega_0' = 10\frac{\sqrt{2}}{\sqrt{101}}\omega_0$, with the value of $\omega_\perp' = 0.1\omega_0' = \frac{\sqrt{2}}{\sqrt{101}}\omega_0$.

For the second case, to keep the magnitude of angular momentum constant, first consider the angular momentum magnitude $H = \omega_0\sqrt{F^2I_x^2\cos^2\Delta\theta + F^2I_y^2\sin^2\Delta\theta + I_z^2}$. To maintain this value compared with the case with $F = 1$, the initial spins are modulated as following.

$$\omega_0' = \sqrt{\frac{I_x^2\cos^2\Delta\theta + I_y^2\sin^2\Delta\theta + I_z^2}{F^2I_x^2\cos^2\Delta\theta + F^2I_y^2\sin^2\Delta\theta + I_z^2}}\omega_0 \tag{3.6}$$

Figures 3.18 and 3.19 show time histories of effective spin rates for the two cases with a changing F and the same damping ratio ($\zeta = 0.1$) and nominal spin rate $\omega_0 = \frac{2\pi}{360}$ at $F = 1$. As shown in Fig. 3.18, when the magnitude of the initial spin rate is kept constant, the magnitude initial energy states are similar, but different, due to the influence of the moments of inertia. It is clear, however, that for an increasing excitation level the system takes longer to dissipate energy and relax to its minimum energy state, and that these minimum energy spin rates are all different.

As seen in Fig. 3.19, for a constant angular momentum the initial energy states are all different, however the final spin rates are the same. This is expected behavior as the final spin

rates are expresses as $\frac{|\vec{H}|}{I_z}$. It is also interesting to observe that the relaxation times are clearly similar to each other despite a large range of values in the initial energies. This indicates that a controlling factor for energy dissipation will be the total angular momentum of the spinning body.

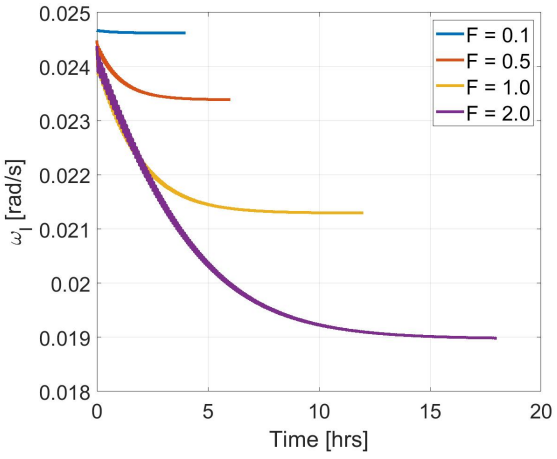

Figure 3.18: F Variation for Constant $|\omega(t_0)|$

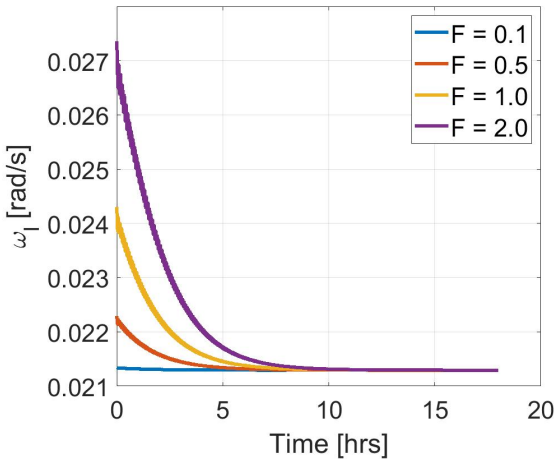

Figure 3.19: F Variation for Constant $|H(t_0)|$

Figures 3.20 and 3.21 show the relaxation times of these energy decay curves for different values of F and damping ratios. For this analysis, their relaxation times are estimated to occur when the energy decays to less than 1% of ΔE with respect to their minimum energy states. Figure 3.20 indicates relaxation times considering variations of F and damping ratio, all with the same magnitude of initial spin rate. The vertical axis is set as log scale and the time axis is scaled by the damping ratio, as investigated previously. Here we see a strong trend of increasing relaxation time with excitation.

This is contrasted with Fig. 3.21 which shows the same quantities but for a fixed value of angular momentum. Here it is clear that there is only a minor variation in relaxation time as systems with different levels of excitation are considered. This indicates that the dissipation of energy occurs rapidly at first, and then as the common spin rate is reached for these different cases the longer relaxation time seems to dominate. I do note the small trend for longer dissipation time for increasing excitation, however this appears small compared to the overall relaxation time.

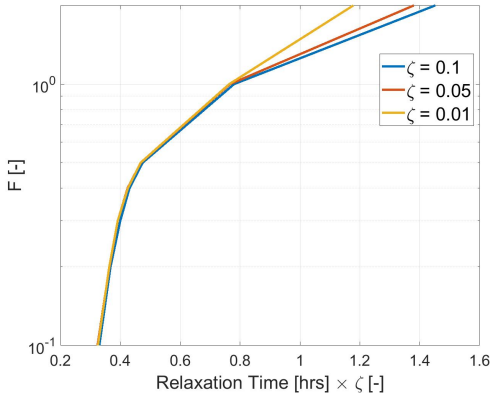

Figure 3.20: F Variation of Relaxation Time same ω_0

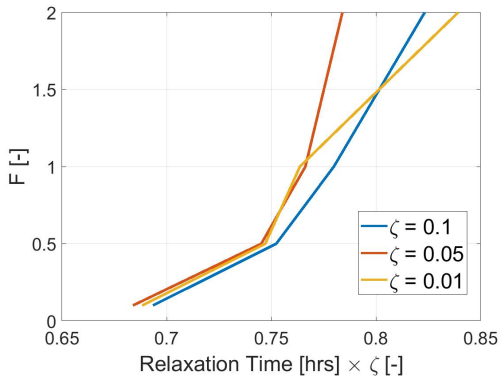

Figure 3.21: F Variation of Relaxation Time same H_0

3.5 Short Summary

In this chapter, a model for the coupled rotational dynamics and internal energy dissipation caused by deformation for a rotating spacecraft was developed and investigated. To model energy loss, FEM dynamics with flexible body theory were combined. Using the FEM analysis model, deformation and fluctuation are demonstrated driven by the accelerations due to non-principal axis rotation. The analysis model is a rigid body with attached flexible space structures. The simulation studies the interaction between deformation and the changing spin rate due to energy dissipation while tumbling. Numerical results for comparisons of energy loss between the constant and the time-varying inertia are provided. In terms of the energy, the nominal situation, which has a constant inertia matrix, conserves energy. On the other hand, analysis that includes the deformation data, energy decays are found. Using the model I explore a few simple scaling relations predicted by a simple model, and confirm that this more general tumbling body with dissipation follows some basic scaling rules for how fast it dissipates energy. The scaling rules involve both the dissipation parameters and the overall level of angular momentum the spacecraft has. Using this model it is possible to analyze the expected tumbling behavior of defunct satellites. Such studies can be of use for matching observations of defunct satellites and to develop plans for interactions with such bodies for debris mitigation purposes.

Chapter 4

Sloshing and GOES Analysis

4.1 Introduction of GOES Analysis

In this chapter, energy dissipation is parsed with actual program data of GOES 10 (Geostationary Operational Environmental Satellite) de-tumbling and sloshing theory. Figure 4.1 shows the overview of GOES R, which is a series of weather satellites. The GOES program is a joint effort of NASA and the National Oceanic and Atmospheric Administration (NOAA). The object of GOES is to help scientists predict weather patterns further in advance and save lives. The satellites are on geostationary orbits at 36,000 [km] above the Earth, which means it has the same orbital period as the Earth. However, after completing their missions, ground observation found the spin rate evolutions of GOES [8, 9]. Many researchers discussed their dynamics from ground observation or long term simulations.

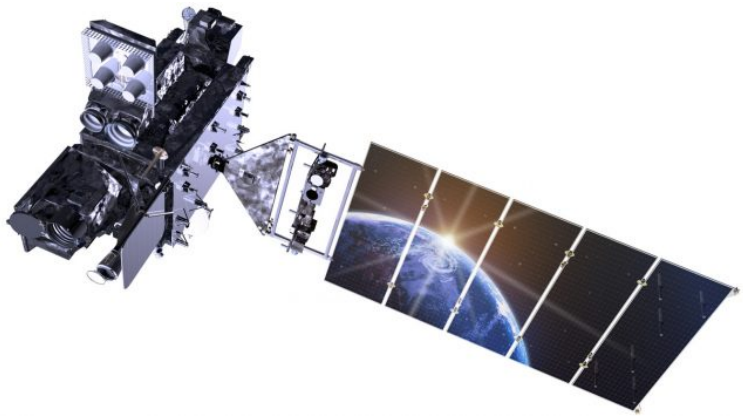

Figure 4.1: GOES R (NOAA website)

In a recent study, Albuja et al. explored the YORP effect for the defunct satellites in GEO, such as the GOES 8 and 10 satellites [2]. They proposed that energy dissipation plays an important role to understand the dynamics of a tumbling satellite. By comparing simulation data of GOES series and my energy dissipation model, accuracy of my modeling is evaluated. There are many causes of energy dissipation. For example, to clarify the dynamic interaction behavior of a flexible body component, we examine sloshing and the control model is examined. They investigated the influence of the vibration and sloshing along the flexible appendages such as antenna and solar arrays as well as the on-board liquid system [13]. With the deformations to cause internal energy dissipations and de-tumbling, sloshing is an important topic. Although debris or defunct satellites are assumed to have run out of fuel at the end of their lives, there are debris which had unexpected mission trouble of control issues in real space activities. Therefore, sloshing might be a cause to dissipate energy. Then, this chapter picks up the sloshing discussions as well.

Figure 4.2 illustrates the outline of discussion in this chapter. There are two stages of discussion; basic and advance. In the basic stage, modeling of energy dissipations with a simple satellite model was demonstrated in previous chapters, where it was focused on deformation. Here, sloshing effects on a tumbling body are introduced and applied to GOES discussions. There are three reasons to conduct a sloshing analysis. Firstly, to reenact the de-tumbling of GOES 10, sloshing theory and documented data for GOES 10 are used. For general energy dissipations, the mechanism is complex and deformations are not the sole as one cause. Therefore, by adding another case to the modeling of energy dissipations, my theory would cover more complex situations. Finally, by using actual parameters of the GOES series, the feasibility of the energy dissipation model is verified.

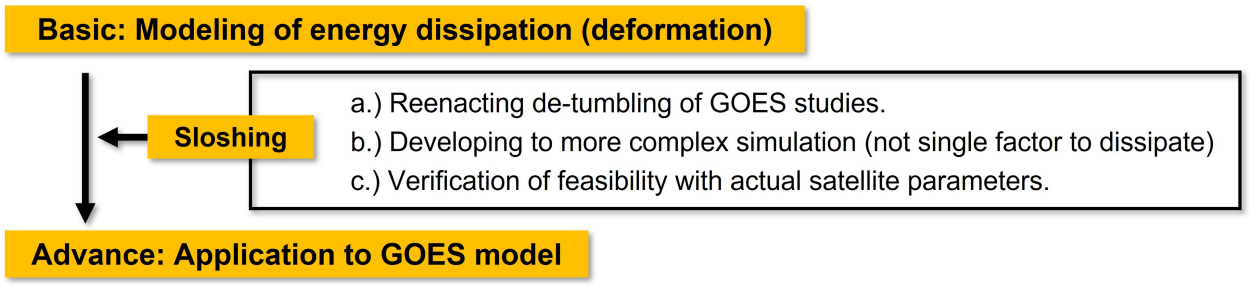

Figure 4.2: Concept of Sloshing and GOES 10 Implications

Major discussions in this chapter are summarized in Tab. 4.1. In the beginning, the GOES program and basic sloshing model are explained, and they are simulated based on GOES parameters. Since the sloshing model has two values which affects de-tumbling behaviors, a Monte Carlo analysis is conducted to find suitable parameters. Among the studies about GOES tumbling, Harvie et al. demonstrated the de-tumbling process in about 28 [hours] with GOES 10 [25]. This 28 [hours] is assumed as a goal and target of relaxation time. Using a basic theory of deformational energy dissipation, the estimation of relaxation time is verified. Finally, case studies of hybrids with deformation and sloshing are demonstrated. Defunct satellites are assumed to have no fuel, but actually complex situations occurred. Brief summaries are described at the end of this chapter.

4.2 GOES Simulation

This section explains the physical and dynamic parameters of the GOES series. Since not all dynamic parameters of GOES are available, full dynamics of GOES are compensated with basic assumptions.

4.2.1 GOES model

Since GOES is a series of satellites and missions, the general design of the space craft was the same. But the detailed design has not been released and there are differences depending on each missions. Refer to [2] and open source information, analysis model is developed. For example, the

Table 4.1: Major Discussions of Sloshing Analysis

	Contents
Sloshing	· Applications of sloshing into GOES models · Monte Carlo analysis to find sloshing parameters
Deformation	· Deformational effects on GOES de-tumbling · Estimation of relaxation time of GOES spinning
Hybrid (Slosh. + Deform.)	· Case studies (dissipated energy by two causes) · Discussions and summary

reference modeled GOES 8 as shown in Fig. 4.3. The general design is composed of a main body and an asymmetrical SAP.

4.2.2 Setups

Table 4.2 summarized the available open information for GOES 10. Using partial information, an analysis model is developed in this section. The rotational frame of the GOES series is shown in Fig. 4.4. In this figure, the X axis is along the velocity vector, the Z axis points continuously towards the earth, and the Y axis is a cross product of vectors along X and Z axes. Spins are described with roll (ϕ), pitch(θ) and yaw(ψ) respectively.

Table 4.2: Partial Information of GOES Dynamics

	Inertia matrix $[kg \cdot m^3]$	Initial angle $[deg]$	Initial spin rate $[deg/s]$	Angular momentum $[Nm \cdot s]$
Symbols	$[I_{GOES}]$	$\begin{bmatrix} \theta \\ \phi \\ \psi \end{bmatrix}$	$\begin{bmatrix} \dot{\psi} \\ \dot{\theta} \\ \dot{\phi} \end{bmatrix}$	$\lvert\vec{H}\rvert$
Parameters	$\begin{bmatrix} 3483.2 & -24.5 & -62.4 \\ -24.5 & 1060.2 & 19.3 \\ -62.4 & 19.3 & 3598.7 \end{bmatrix}$	$\begin{bmatrix} 6.5 \\ 24 \\ - \end{bmatrix}$	$\begin{bmatrix} -0.25 \\ 0.05 \\ 0.75 \end{bmatrix}$	47.7

While de-tumbling, the nutation angle ($\theta = 6.5$ $[deg]$) goes to 0. Since GOES 10 rotation is written with yaw-pitch-row condition, body spin rates are transformed by the transform matrix,

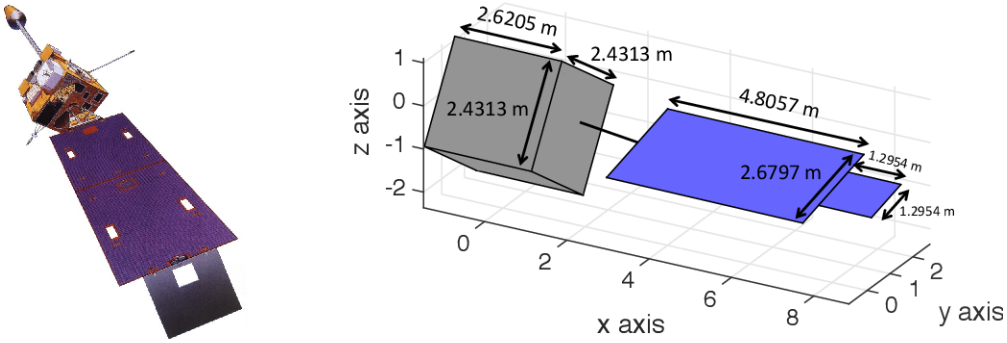

(a) GOES satellite (b) Simple GOES 8 satellite model

Figure 4.3: GOES 8 Configuration [2]

the angular velocity vector for the initial condition in the body frame is estimated as the following.

$$ {}^{B}\vec{\omega}_{t=0} = \begin{bmatrix} -\sin\theta & 0 & 1 \\ \sin\phi\cos\theta & \cos\phi & 0 \\ \cos\phi\cos\theta & -\sin\phi & 0 \end{bmatrix} \begin{bmatrix} \dot{\psi} \\ \dot{\theta} \\ \dot{\phi} \end{bmatrix}_{t=0} = \begin{bmatrix} -0.0058 \\ 0.0061 \\ 0.0115 \end{bmatrix}_{t=0} [rad/s] \tag{4.1} $$

Angular momentum vector is defined as

$$ \vec{H} = [I_{GOES}]\,\vec{\omega} \tag{4.2} $$

Then, angular momentum vector and its magnitude are as follows.

$$ \vec{H} = \begin{bmatrix} -21.23 \\ 6.81 \\ 41.96 \end{bmatrix}_{t=0}, \quad \left|\vec{H}\right| = 47.52\ [Nm \cdot s] \tag{4.3} $$

The magnitude of angular momentum is almost the same as the GOES 10 model. To find the history of angular momentum, dynamics are integrated with the rigid body equation,

$$ I\dot{\omega} = -\tilde{\omega} I \omega \tag{4.4} $$

The below figures show constant angular momentum with the estimated GOES 10 inertia matrix with a rigid body equation. The left figure shows a constant angular momentum and the right unit sphere stands for angular momentum trace in the body frame.

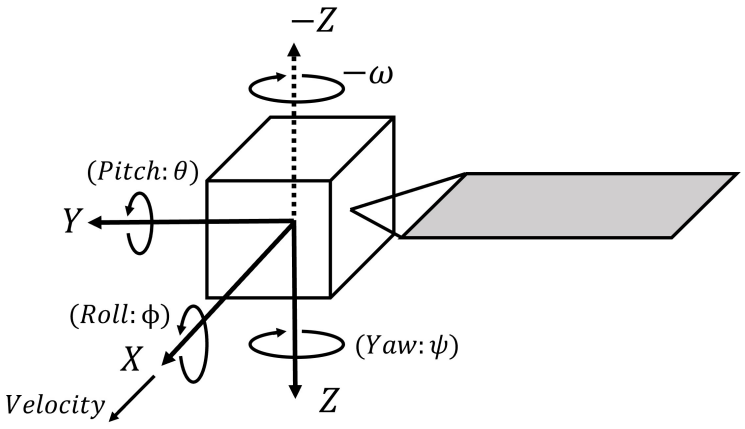

Figure 4.4: Satellite Rotation Frame

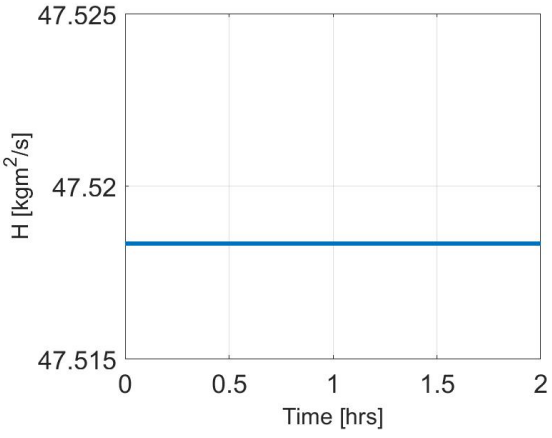

Figure 4.5: Constant Angular Momentum

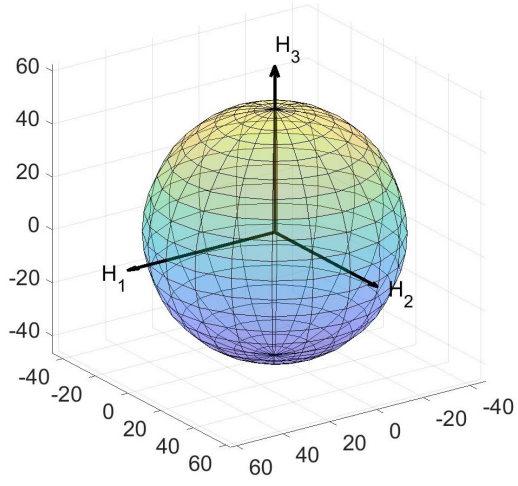

Figure 4.6: Sphere of Angular Momentum

4.3 Sloshing Analysis

4.3.1 Dynamics

To compare modeling of energy dissipation and simulate a de-tumbling of the satellite, sloshing analysis is considered in this section. Rahn developed a simple sloshing model, which consists of a rigid space craft with a spherical slug. The configuration is as shown in Fig. 4.7. The slug is

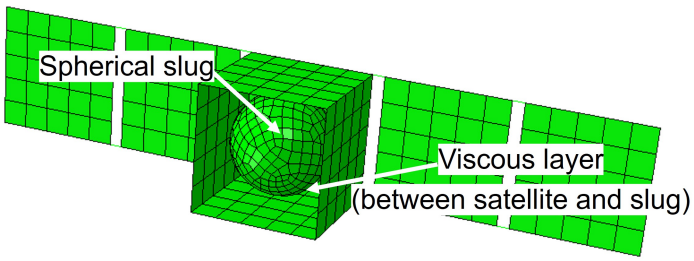

Figure 4.7: Sloshing Model

located at the satellite center of mass and between the satellite and the slug is a thin viscous fluid layer. Although fuels of defunct satellites or space debris are all used at the end of life, this model can be used to refer to general energy dissipation. The equations of motion for the spacecraft and slug are,

$$[I]\,\dot{\omega} = -[\tilde{\omega}]\,[I]\,\omega + \mu\sigma + L \tag{4.5}$$

$$\dot{\sigma} = -\dot{\omega} - [\tilde{\omega}]\,\sigma - \frac{\mu}{J}\sigma \tag{4.6}$$

where $[I] = diag(I_1, I_2, I_3)$, J is the spherical slug's inertia, μ is the non-negative viscous damping coefficient, σ is the angular velocity of the slug relative to the body frame in the spacecraft, and L is the external torque acting on the spacecraft. $\dot{\sigma}$ is the time derivative with respect to the body frame. As for total kinetic energy, T and its time derivative,

$$\dot{T} = -\mu\sigma^2 \tag{4.7}$$

indicates that positive value of μ will dissipate energy. On the other hand, energy is conserved when the spacecraft and slug are uniformly rotating with equal inertial angular velocities. Derivations

are in Appendix. D. For non-zero μ, the system will dissipate energy whenever there is relative motion between the spacecraft and spherical slug.

4.3.2 GOES 10 Case

Based on parameters in Tab. 4.2 and Eqs. 4.5 and 4.6, a simple sloshing is simulated. Conditions are summarized in Tab. 4.3. The inertia matrix and spin rates refer to the GOES 10 parameters. As shown in Eq. 4.5, J and μ decide dynamics behaviors. This simulations are with $J = 20$ and $\mu = 1$ respectively. Then, Figs. 4.8 through 4.10 show the results of it. Figure 4.8 shows

Table 4.3: Conditions of Simple Sloshing

Causes of energy dissipation	Sloshing
Analysis model	GOES 10
Initial spin rate	GOES 10
Equations	Sloshing
Parameters	$J = 20, \mu = 1$

angular velocities in the body frame. Figure 4.9 shows a total kinetic energy of rotation, a dashed line indicates minimum energy state of system. Relaxation time is estimated as $\sqrt{{\omega_x}^2 + {\omega_y}^2} \leq 1e^{-3}$, and 33.7 [hours] in Fig. 4.9. As shown in Fig. 4.8, rotation around X and Y axes go to 0 as time goes on, while ω_z goes to a particular value. Although factors to cause energy dissipation are different with the deformation, the sloshing model achieves de-tumbling while keeping angular momentum constant as shown in Fig. 4.10.

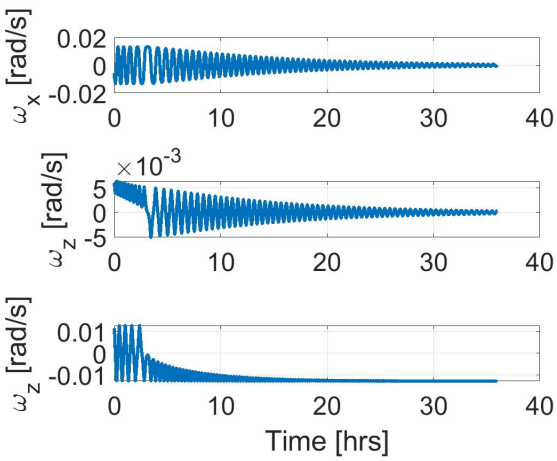

Figure 4.8: Angular Velocities with Sloshing

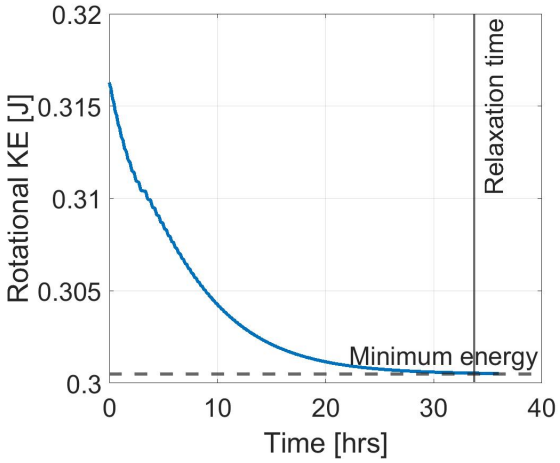

Figure 4.9: Kinetic Energy with Sloshing

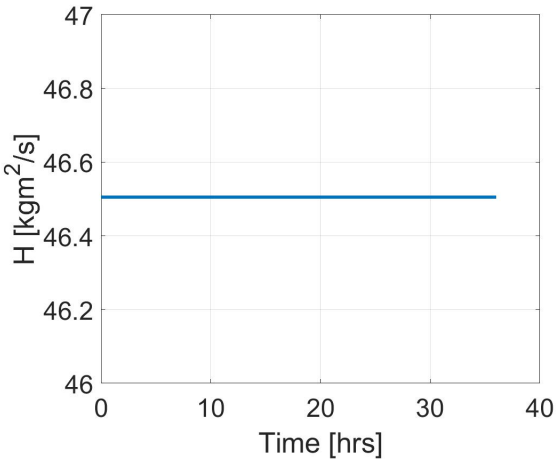

Figure 4.10: Angular Momentum with Sloshing

As for the sloshing model, variations of energy curves depend on J and μ parameters in Eqs. 4.5 and 4.6. Then, variations of curves are explored with these parameters. Figures 4.11 and 4.12 show energy dissipation curves with an arbitrary change of J and μ parameters. Large J causes the satellite to dissipate energy quickly, and large μ causes a longer relaxation time. Refer to Eq. 4.5, larger μ becomes $+\mu\sigma$ term gets large and a torque works to the satellite body rotation. Thus, relaxation time gets longer. After exploration of the combination of J and μ values,

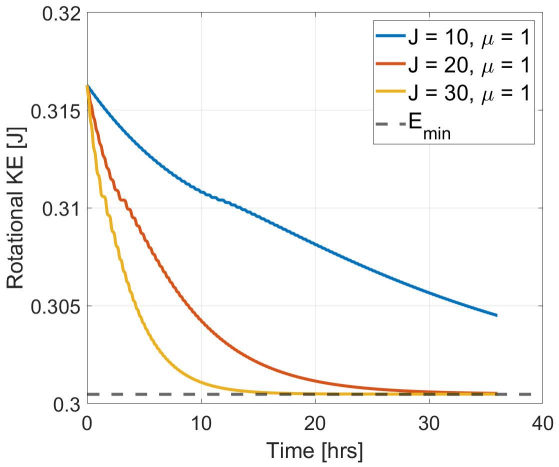

Figure 4.11: Variations of J

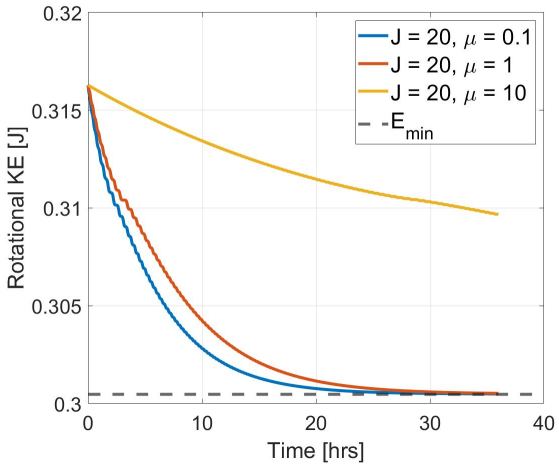

Figure 4.12: Variations of μ

GOES 10 de-tumbling is reenacted. These results are shown as Figs. 4.13 and 4.14. $J = 25$ and $\mu = 1.306$ approximately matched with GOES 10 simulations. As shown in Fig. 4.14, kinetic energy dissipates to the minimum energy state at 28 [hours] with estimated as $\sqrt{{\omega_x}^2 + {\omega_y}^2} \leq 1e^{-3}$. The way of finding these parameters is explained in following section.

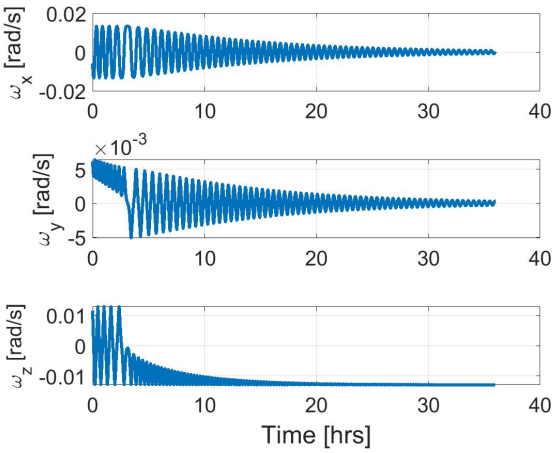

Figure 4.13: GOES $\vec{\omega}$ Reenacted by Sloshing

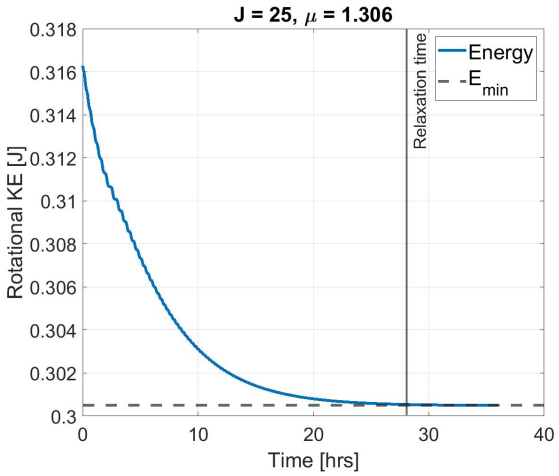

Figure 4.14: GOES T Reenacted by Sloshing

4.4 GOES- α simulation

This sections discusses a modeling of GOES-α and interactions of deformation and sloshing to cause energy dissipations. First, based on GOES physical characteristics, GOES-α is developed with FEM, as shown in Fig. 4.15. Since details of parameters are not available, the features of GOES shapes are mainly focused on asymmetric with joint between the body and SAP. Similar to simple satellite models, which were used in previous chapters, the main body is composed of aluminum and assumed to be a rigid body with SAP, and joint flexibility which cause fluctuations and de-tumbling. The size of the main body is totally the same. But the length of the SAP along Y axis is 0.8 [m] longer than the actual model. This is because of adding joints and the inertia matrix should be as close as possible to GOES 10's. This information is summarized in Tab. 4.4.

Table 4.5 shows case studies of GOES and sloshing simulations. At first, using GOES-α model, dynamics of deformation and its energy dissipation are explored. Secondly, using initial conditions of GOES 10, de-tumbling is reenacted. Using the damping equation, flexible body equation, and sloshing dynamics, hybrid case of the combination with deformation and sloshing are simulated in Case 3.

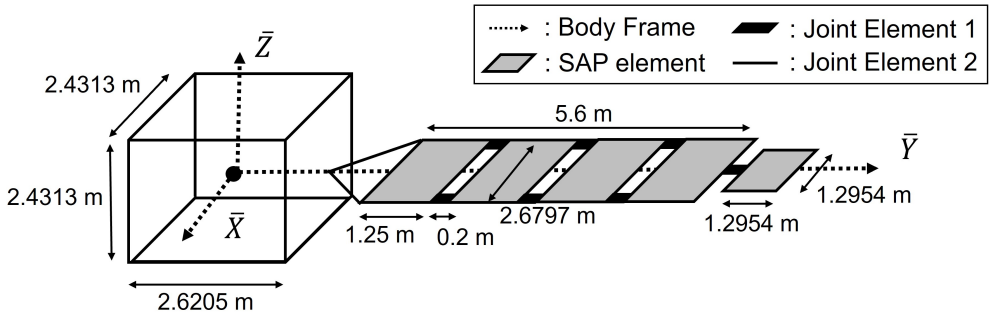

Figure 4.15: GOES-α Configuration

Table 4.4: Parameters of GOES Modeling

	Inertia matrix $[kg \cdot m^3]$	Main body $[m]$	SAP $[m]$
GOES 10	$[I_{GOES}] = \begin{bmatrix} 3483.2 & -24.5 & -62.4 \\ -24.5 & 1060.2 & 19.3 \\ -62.4 & 19.3 & 3598.7 \end{bmatrix}$	$2.4313 \times 2.6205 \times 2.4313$	2.6797×4.8057 $+1.2954 \times 1.2954$
GOES-α	$[I]_{\alpha} = \begin{bmatrix} 3292.1 & 23.0 & 0.0 \\ 23 & 964.5 & 0.0 \\ 0 & 0 & 3542.0 \end{bmatrix}$	$2.4313 \times 2.6205 \times 2.4313$	2.6797×5.6 $+1.2954 \times 1.2954$

Table 4.5: Case Studies of GOES-α

	Simulations	Outputs
Case 1	Deformation	Verifications using GOES-α model Predicting relaxation times
Case 2	Sloshing	Reenact GOES 10 De-tumbling
Case 3	Deformation and Sloshing	Discussion of dominant factor

4.4.1 Case 1: Deformation Effects on GOES-α

Using GOES-α model, deformation and its energy dissipations are simulated. Simulation setups are summarized in Tab. 4.6. Initial spin rates are based on GOES 10 initial conditions. As shown in this table, simulations include damping and flexible body equation. Simultaneously, variations of damping parameter (ζ) are evaluated with in order to match the 28 [hours] relaxation times. Simulation results are shown in Figs. 4.16 and 4.17.

Table 4.6: Case 1 Conditions

Causes of energy dissipation	Deformation
Analysis model	GOES-α
Initial spin rate	GOES 10
Equations	Damping equation Flexible body equation
Change of Parameters	ζ

Figure 4.16 shows ζ variations for energy dissipation curves. As already discussed in previous chapters, a strong ζ makes relaxation time short. Due to the limits of computer storage, full calculation cannot be terminated. Therefore, the relaxation period is predicted based on an exponential function with $\zeta = 5e^{-3}$. This parameter matches with the GOES 10 relaxation time.

4.4.2 Case 2: Sloshing Approach

Using the GOES-α model, sloshing simulations are conducted. As already discussed in the above sections, the change of sloshing parameters causes variations of the relaxation time. To find parameters of J and μ, which match relaxation times of GOES 10 relaxation time, Monte Carlo simulations are applied. The Monte Carlo simulation is a computational method that finds an approximate solution by performing simulations many times using a large amount of random numbers. In this situation, under the same initial conditions of rotational angular velocity, J and μ are changed and confirmed the transition of relaxation time. Simulation Conditions are summarized in Tab. 4.7. Simulation results are shown in Figs. 4.18 and 4.19. By finding parameters of J and μ, GOES 10 relaxation time is reenacted with GOES-α model. Both figures have a large amount of

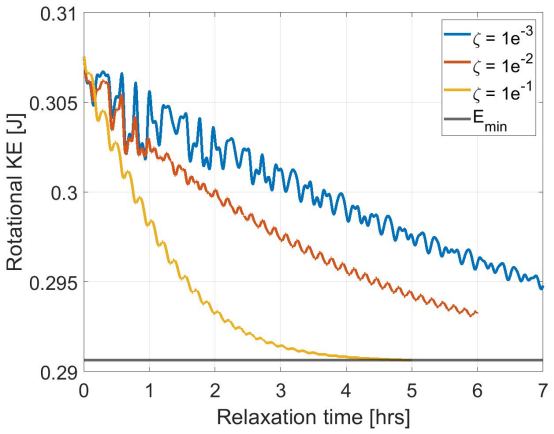

Figure 4.16: GOES-α Variation with ζ

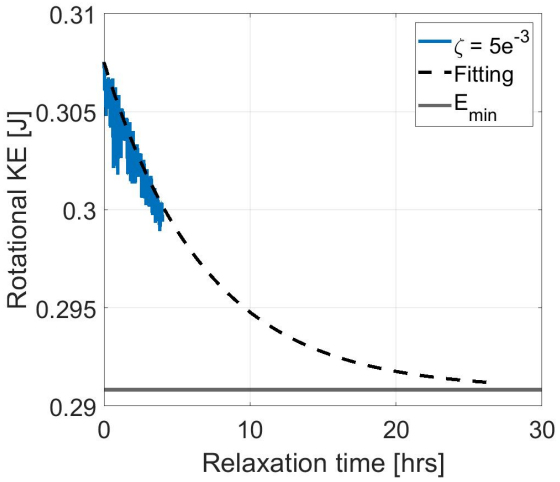

Figure 4.17: GOES-α Relaxation Time

combination of J and μ. In Fig. 4.18, black line indicates a 28 [hours] relaxation time which matches the GOES 10 case. Although there is an infinite combination of them, reasonable parameters are found as shown in Fig. 4.19. As a result, $J = 19.9$ and $\mu = 1.35$ as shown in Fig. 4.20 relaxation times archives matching GOES 10 de-tumbling with GOES-α model.

In summary, there are two approaches. One is deformation with the exponential function with $\zeta = 5e^{-3}$, Another is the sloshing approach with $J = 19.9$ and $\mu = 1.35$. In the following sections, hybrid models with deformation and sloshing are discussed.

Table 4.7: Case 2 Conditions

Causes of energy dissipation	Sloshing
Analysis model	GOES-α
Initial spin rate	GOES 10
Equations	Sloshing
Change of Parameters	J and μ (Monte Carlo)

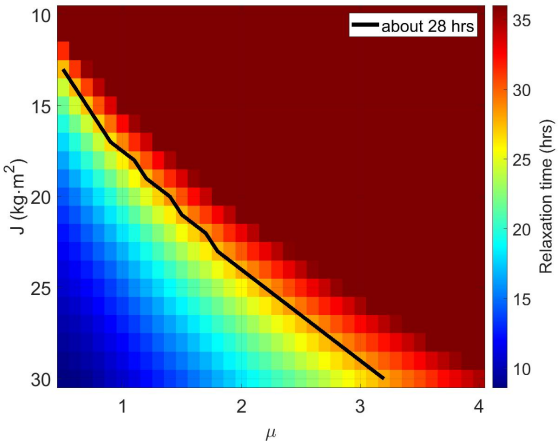

Figure 4.18: Monte Carlo Simulation 1

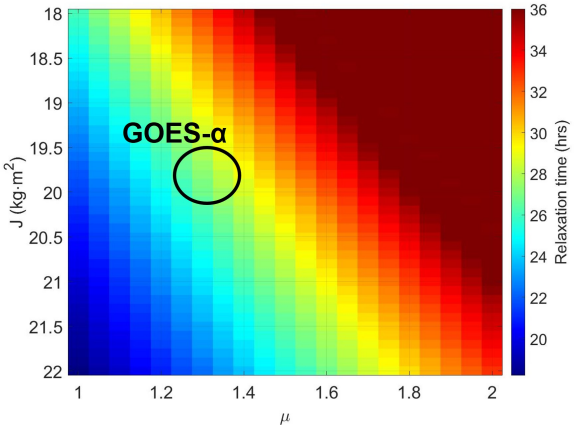

Figure 4.19: Monte Carlo Simulation 2

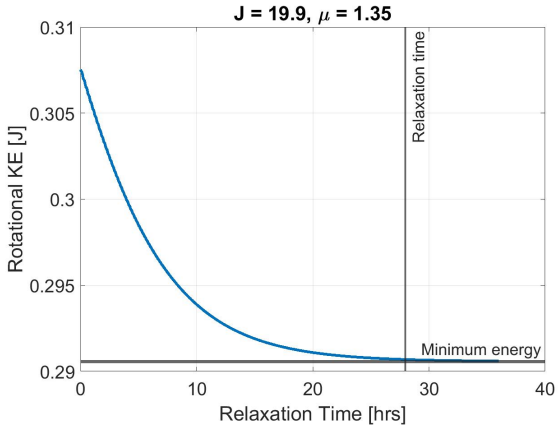

Figure 4.20: Reenact GOES 10 De-tumbling

4.4.3 Case 3: Hybrid model

The combination of de-tumbling causes are explored in this section with sloshing and deformation. By simulating under there conditions, we can see how physical phenomenon interact with each other and cause de-tumbling and energy dissipations. The conditions are summarized in Tab. 4.8. To achieve GOES 10 relaxation time as a target, sloshing and deformation parameters are found. From previous discussion, we can reenact GOES 10 relaxation time using both deformation and sloshing models. In the hybrid case, dynamics are integrated simultaneously. For example, in Case 3-1, we already knew that using $J = 19.9$ and $\mu = 1.35$ in a sloshing model can simulate a 28 [hours] relaxation time, so ζ variations from a deformation aspect are explored. On the other hand, in Case 3-2, J and μ parameters are varied, but ζ is fixed, which simulates a 28 [hours] relaxation time using simple deformational model approach.

Figures 4.21 and 4.22 show examples of hybrid simulations. For the deformation parameters as $\zeta = 0.1$ and added with sloshing theories as $J = 20, \mu = 1$. Of course, the hybrid simulation model causes energy dissipation more quickly than a single factor simulation. Similar to Fig.4.21, Fig. 4.22 indicates the energy decay curves with a simple deformation case and a hybrid version of dynamics. For example, if a system loses internal energy by deformational effects, the relaxation time is estimated as 12 [hours] with a blue highlight. But if sloshing is added on to this system, it loses internal energy in 8 [hours]. However, we cannot see which cause is dominant for energy dissipation. In the following sections, this topic is explored.

Table 4.8: Case 3 Conditions

Causes of energy dissipation	Sloshing, Deformation
Analysis model	GOES-α
Initial spin rate	GOES 10
Equations	Damping equation Flexible body equation Sloshing
Case 3-1	$(J = 19.9, \mu = 1.35)$ plus ζ variation
Case 3-2	J and μ variation plus $(\zeta = 5e^{-3})$
Case 3-3	Achieving 28 hrs with hybrid model

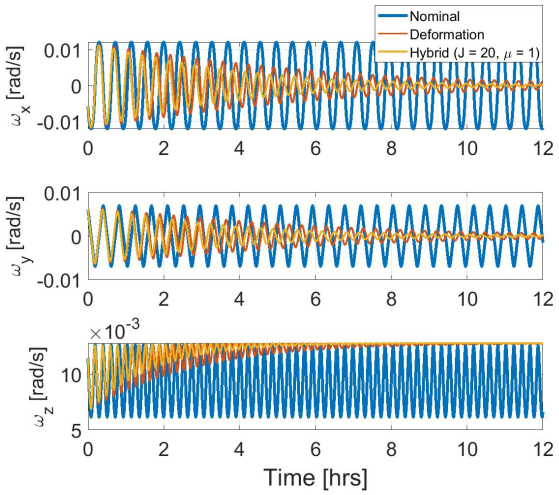

Figure 4.21: Angular Velocities in Hybrid Model

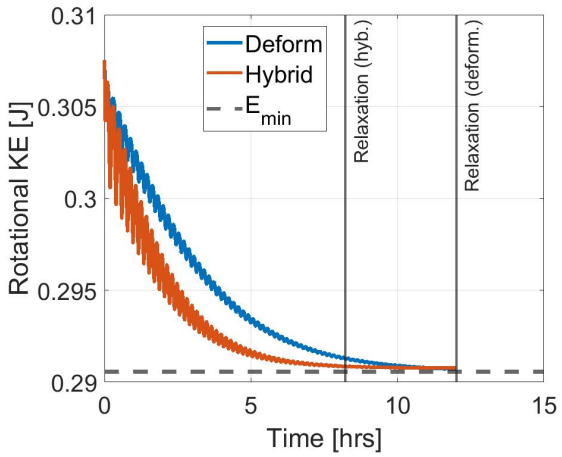

Figure 4.22: Energy Curves of Hybrid Model $\zeta = 0.1$

4.4.3.1 Case 3-1

Figure 4.23 shows variation of damping ratio, and its energy loss curves. The dashed line indicates GOES 10 curves simulated by simple sloshing dynamics. The bottom line shows the minimum energy state. Figure 4.24 shows the relationships between the damping ratio and their relaxation time. Of course, weaker damping (close to $\zeta = 0$) approaches 28 [hours]. But, due to the limits of computer storage, an extremely weak damping case was not computed in the hybrid model. At least, we can predict even extremely weak damping affects on the energy decay curves.

4.4.3.2 Case 3-2

As I discussed in the above sections, dashed lines are expressed with exponential functions with power of $5e^{-3} \times t$. By adding variation to the sloshing parameters, behaviors of energy decays are confirmed. Especially, Fig. 4.25 includes J variations with a fixed μ and deformation conditions. We can see a lower value J moves closer to the dashed line. Similar to this, Fig. 4.26 shows μ variation with constant J and deformation conditions. In both examples, in the hybrid case, small J and large μ are needed to achieve a 28 [hours] relaxation time. But due to the limits

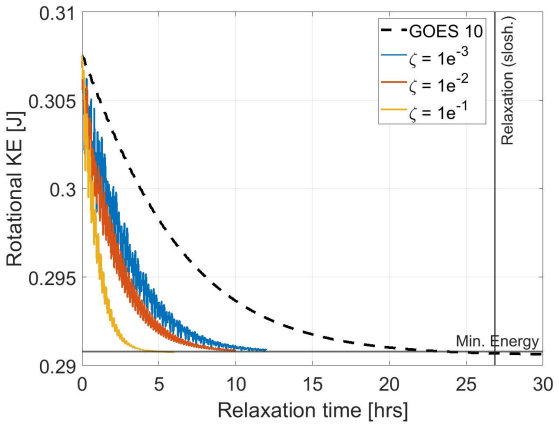

Figure 4.23: Energy Decay Curves as Case 3-1

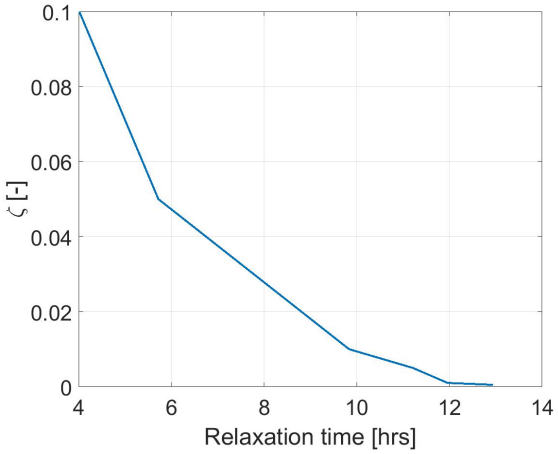

Figure 4.24: Relaxation times as Case 3-1

of simulation time on the computer, the final states are not confirmed. For Case 3-3, this area is explored.

4.4.3.3 Case 3-3

Based on the above discussion, we can see that two causes of de-tumblings are affected by each other. To achieve a 28 [hours] relaxation with the hybrid case, this section explores using a wider range of J and μ. Figure 4.27 shows a Monte Carlo simulation of GOES-α data and sloshing parameters (J and μ). A dot in this figure depicts GOES 10 relaxation point with sloshing dynamics, which is $J = 19.9$ and $\mu = 1.35$. We already know that the hybrid case cannot match this point. Therefore, longer relaxation times are explored to fit this target point to the hybrid model from sloshing simulation. As shown in this figure, smaller J with constant μ as 1.35 is set as direction 1. Oppositely larger μ with constant J with $J = 1.35$ is set as direction 2. Larger J means relatively small μ, and larger μ indicates quick spin rate of the liquid. Two patterns are summarized as J variation while keeping μ constant, and μ variation while keeping J constant.

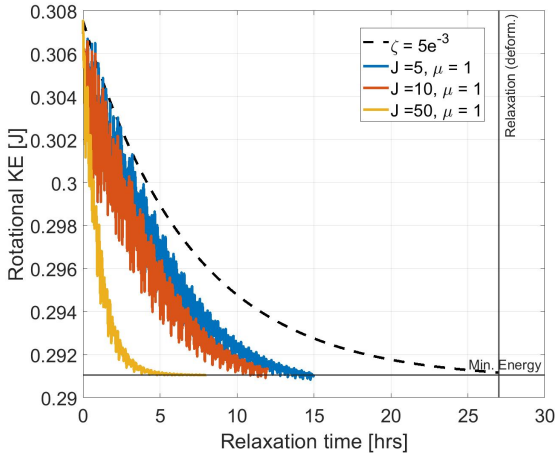

Figure 4.25: Energy Decay Curves as Case 3-2

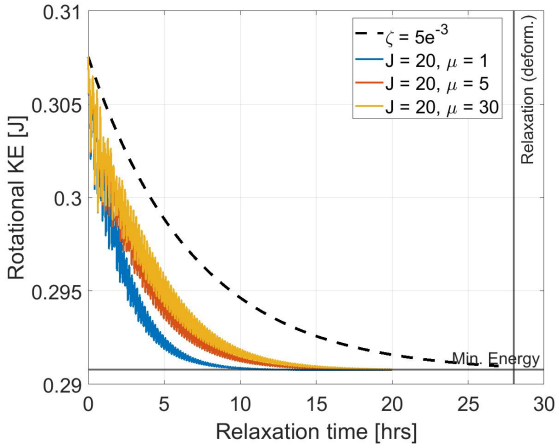

Figure 4.26: Relaxation times as Case 3-2

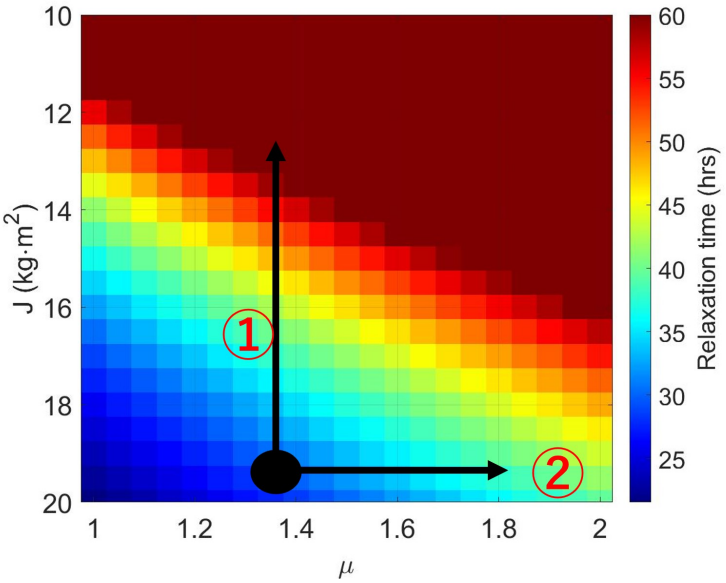

Figure 4.27: Monte Carlo Simulation 3

At first, an extreme case of simple sloshing dynamics with J and μ parameters were explored because it was needed to check for behaviors for smaller J and larger μ based on the GOES 10 position. These results are shown as Figs. 4.28 and 4.29. Figure 4.28 shows the behavior of J getting smaller from $J = 19.9$. As shown in this figure, there is a limit of smaller J as $J = 1$. Similar to Fig. 4.28, the increase of μ has a longer relaxation time as shown in Fig. 4.29.

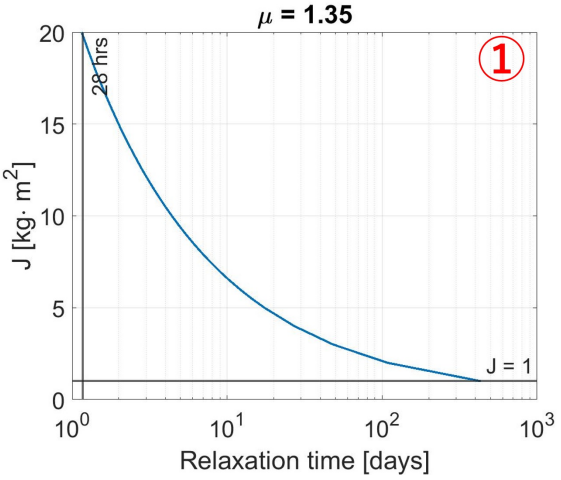

Figure 4.28: Smaller J with Constant μ

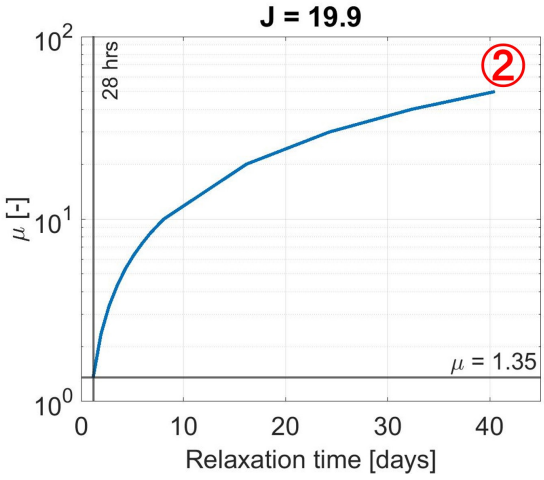

Figure 4.29: Larger μ with Constant J

Along with considering extreme parameters of J and μ, hybrid cases were simulated. The simulation results are shown in Figs. 4.30 and 4.31. Figure 4.30 indicates how increase relaxation times along one direction by keeping μ constant as 1.35. Yellow and red lines highlight hybrid cases of energy dissipations. The blue line shows simple sloshing theories with $\mu = 1.35$ in Fig. 4.30. More than $J = 10$, the curves are affected by sloshing. As already shown in Fig. 4.28, there is a simulation limit at $J = 1$. However, even smaller J cases with small damping such as $\zeta = 5e^{-3}$, relaxation times cannot be over 28 [hours]. Similarly, Fig. 4.31 shows a larger μ value and a constant $J = 19.9$ for the hybrid case. Yellow and red lines include deformational dynamics and sloshing theories. Their relaxation times are getting longer slightly with the increase of μ value. But they also still cannot be longer than 28 [hours] relaxation time.

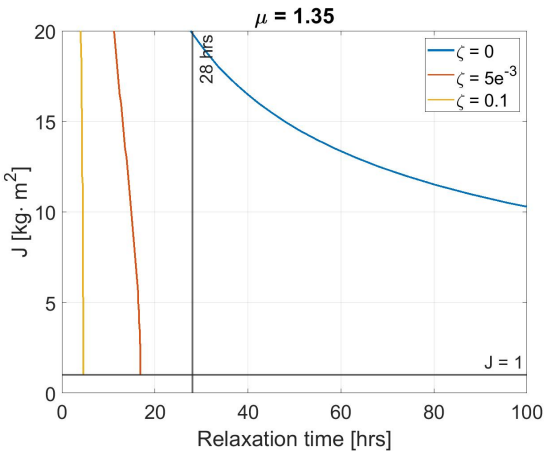

Figure 4.30: Smaller J in Hybrid Case

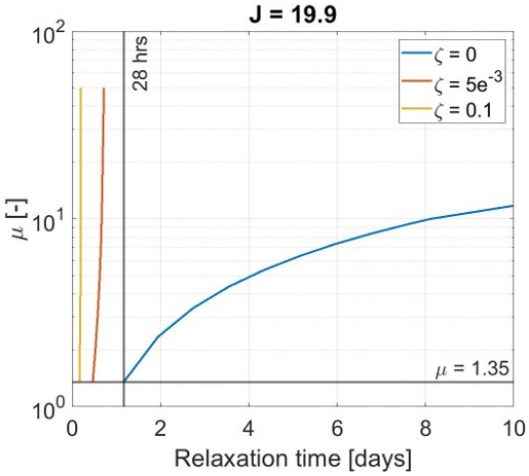

Figure 4.31: Larger μ in Hybrid Case

4.5 Short Summary

In this chapter, I discussed energy dissipation model with the GOES study and sloshing. In the beginning, using GOES parameters from open sources, an analysis model was developed with FEM. It also confirmed the deformational effects on GOES de-tumbling. During sloshing discussions, the Monte Carlo analysis was used. By combining deformational effects and sloshing on the energy dissipation model simultaneously, interesting results were obtained. Deformational damping is more dominant than sloshing analysis. Of course, double factors caused energy to dissipate quickly. However, when considered in a weaker sloshing case, the relaxation time is limited by the deformational effect.

Chapter 5

Sensitivity Analysis

5.1 Introduction of Sensitivity Analysis

In this chapter, I will discuss the sensitivity analysis for internal energy dissipation with the change of structural parameters of the analysis model. Basically, sensitivity analysis is used for many reasons. For example, by comparing outputs, we can find which inputs contribute most to output variability or which parameters are most highly correlated with the output. In terms of error analysis, sensitivity analysis is able to reduce output uncertainty. There are many different ways of conducting sensitivity analyses. In structural dynamics, the uncertainties in material, geometrical, environmental and loading conditions of structures result in a certain scatter of structure response [23]. There are many parameters involved in simulations model. However, in terms of energy dissipation modeling, stiffness and flexibility is crucial because they dominantly cause energy dissipation while satellites are tumbling. As I discussed in the above section, the damping term or its matrix is also important to decide the behaviors of energy dissipations. Actually I used the Rayleigh damping model for my simulations, which have a proportional term with mass and stiffness matrices. Therefore, the change of damping, mass, and stiffness matrices is explored as sensitivity analysis. In terms of the structural component of the analysis model, the weight and stiffness of SAP, which are designed as CFRP, and joint stiffness, which is the connection between the body and the SAP, are targets of this work.

5.2 Sensitivity Analysis on the Structural Model

There are many studies to improve the mechanical performance of CFRP. However, CFRP parameters are changed by heat cycles or radiation in space. For example, there have been a large number of studies that experimentally explored the effect of thermal treatment on the mechanical behaviors of CFRP [55]. Of course, depending on the different magnitudes and periods of time, such as related to temperature, CFRP showed a decreased mechanical behavior after thermal treatment [58]. Furthermore, it has more effects on the defunct satellite since the direction of the SAP is assumed as a malfunction.

Figure 5.1 indicates the concept of sensitivity analysis on this work. As I demonstrated in the previous chapters, two models are designed to explore internal energy dissipations caused by deformation. One is simple satellite model, which has a main rigid body and two SAPs. Another model is GOES-α. To explore sensitivities on energy dissipation, two parameters were focused on: mass and stiffness. To change the mass matrix (∂M), the weight of the SAP is changed. For the stiffness, the elasticity of the SAP and joint elements 1 are changed. Because of the unsynchronized shape of both models, the joint element 2 is not focused on. Of course, even mass and stiffness change, so evaluation of sensitivity is conducted by energy dissipation curves and their relaxation time. The below figures show more conceptional thought of sensitivity analysis. As shown in Fig. 5.2, the main point mass change is to cause unbalanced effects on the energy dissipation. Of course, a completely rigid body does not lose energy while it tumbles. But, by attaching additional component, which mass varies from small to large, the behaviors of energy dissipations are affected.

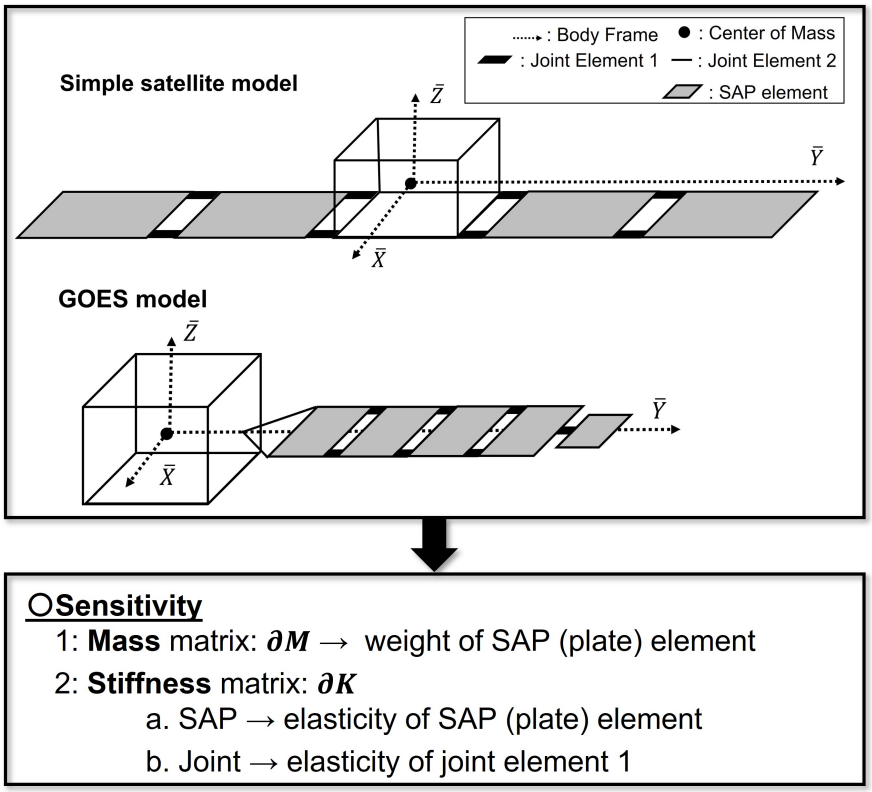

Figure 5.1: Concept of Sensitivity Analysis

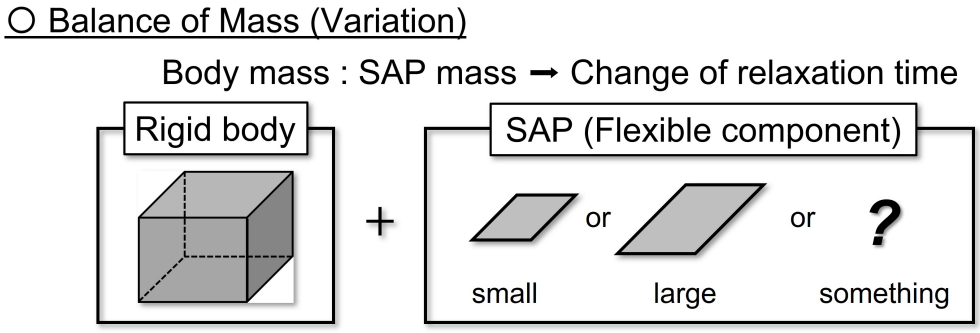

Figure 5.2: Concept of Mass Changes

On the other hand, Fig 5.3 indicates the concept of stiffness variation for energy dissipations. As mentioned in the introduction, the stiffness of SAP is changed by space environmental factors such as heat cycles or radiation of the sun. Furthermore, defunct satellites or debris are not in control of their body attitude. The first item of stiffness change is a variation from 10 $[GPa]$, which is set as a nominal value. For the second item, stiffness variations at joint components of both models are examined. Since joint flexibilities of models cause large fluctuations while it is tumbling, and the effects on the energy dissipations are examined. The nominal values are set as 1.0 $[KPa]$ for the simple satellite model, 0.50 $[MPa]$ for the GOES model respectively.

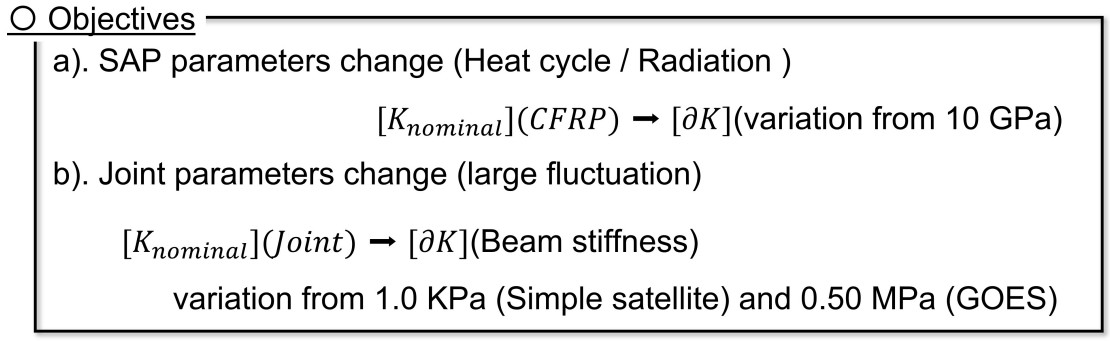

Figure 5.3: Concept of Stiffness Changes

5.3 Simulation Setups

Along with the above discussion, the sensitivity analysis on internal energy dissipations are explored by the change of the mass and stiffness matrices. The below table shows variations of sensitivity analysis in this section. To change the mass matrix, the density (ρ) of SAP elements are changed. At the same time, by changing the mass of SAP, inertia matrix and derivatives of the inertia matrix are changed. Automatically, the initial energy state and minimum energy states are different in these simulations. The relaxation times of de-tumbling and effects of the damping are evaluated as outputs. For the stiffness sensitivity, plates and beams are changed and performances are compared. The joint length variation cannot be discussed in this work. However, if the length of the joint is extended, the stiffness is weakened, the inertia and its derivative are also changed,

and the damping matrix is also changed. There are values which are extremely affected. Therefore, we cannot distinguish which factors generated the change of performance. As in previous chapters, relaxation time is estimated as $\sqrt{{\omega_x}^2 + {\omega_y}^2} \leq 1e^{-3}$.

Table 5.1: Variation of sensitivity parameters

Matrix	Parameters Variation		
	Objects	Element	Dynamics
$[\partial M]$	Balance of Mass	Density (ρ) of plate (SAP = CFRP)	$[I], [\dot{I}], [C]$
$[\partial K]$	Flexibility of SAP	Stiffness (E) of plate (SAP = CFRP)	$[C]$
	Fluctuation at Joint	Stiffness (E) of beam (Joint)	

Nominal Case

In our simulation, I assigned Rayleigh damping in the damping equation, so the mass or stiffness variation cause the change of ($[C]$) as well. Such as

$$[\partial C] \quad = \quad \alpha\,[\partial M] + \beta\,[\partial K] \tag{5.1}$$

Such a case, we cannot distinguish which parameters has the greatest effects on the simulation results. Therefore, $[C_o]$ is set as fixed value and nominal case. For the dynamics of sensitivity analysis,

$$[\partial M]\,\ddot{X} + [C_o]\,\dot{X} + [\partial K]\,X = f(\vec{t}) \tag{5.2}$$

Either the mass or the stiffness matrix is changed, but damping matrix is constant. Below figures shows a nominal energy dissipation with the simple satellite (SC) model and the GOES-α case respectively. These simulations are conducted with a flexible body and deformational effects. As shown in Figs. 5.4 and 5.5, relaxation time is estimated as 9.6 and 4.6 [hours]. respectively. These simulations and parameters, which are summarized in Tab. 5.2 and 5.3, are taken as nominal sets. Mass ratio and stiffness are going to be changed to evaluate of sensitivity.

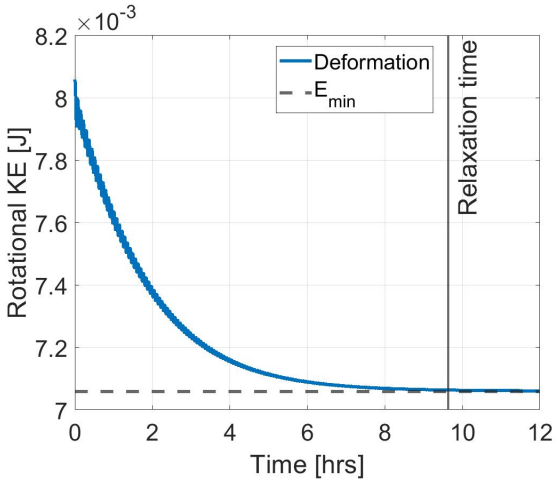

Figure 5.4: Nominal Dissipation (SC)

Table 5.2: Nominal SC Parameters

Nominal set (M_o, K_o, C_o)		
Relaxation Time		9.6 [hrs]
Mass ratio ($\frac{M_{SAP}}{M_{body}}$)		7.8 [%]
Stiffness (E)	**SAP**	10.0 [GPa]
	Joint	1.0 [KPa]

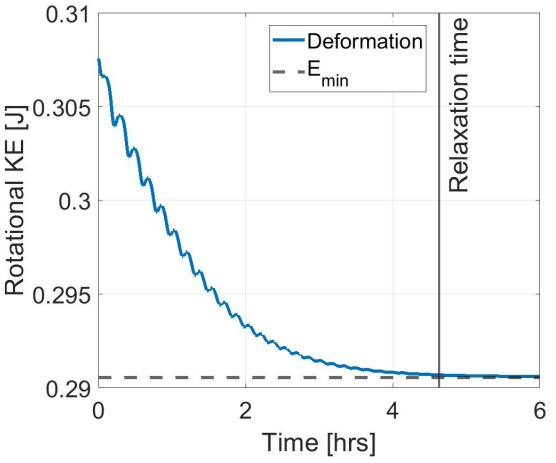

Figure 5.5: Nominal Dissipation (GOES-α)

Table 5.3: Nominal GOES-α Parameters

Nominal set (M_o, K_o, C_o)		
Relaxation Time		4.6 [hrs]
Mass ratio ($\frac{M_{SAP}}{M_{body}}$)		7.7 [%]
Stiffness (E)	**SAP**	10.0 [GPa]
	Joint	0.50 [MPa]

5.4 Mass Sensitivity

The below figures show the simulation results of mass sensitivity. The vertical axis is set as a ratio of SAP and body mass $\left(= \frac{M_{SAP}}{M_{body}}\right)$ with a log scale. As a numerical simulation, the density of the plate elements that make up the SAP (=CFRP) are changed. By changing the density of the element (ρ_e), the entire mass matrix and its ratio are changed as well.

$$\rho_e = \alpha \times \rho_e(nominal) \tag{5.3}$$

$$\alpha = 0.25 \sim 5.0$$

As the weight of the SAP is increased, the entire weight is increased as well. But, the vertical axis is set as SAP mass with respect to the body mass. The horizontal axes show relaxation time. We can see that both the simple satellite and the GOES-α cases have similar curves of relaxation time. This curve means that if the SAP is much heavier or lighter with respect to the body, the relaxation times get longer.

Regarding the comparison of damping effects, in the lighter case of M_{SAP}, when the entire mass matrix gets smaller than nominal, then, the stiffness matrix is dominant on the energy dissipation. Also, in the opposite case, when there is a heavier SAP increases large values in the entire mass matrix, and the damping is stronger than nominal and makes the relaxation time shorter by the Rayleigh damping which is a proportional term with stiffness and mass matrices.

5.5 Stiffness Sensitivity

Similar to above, this section shows stiffness sensitivity of the plate and joint respectively. Simulation results are compared with the damping variation as well.

5.5.1 Change of SAP Stiffness

In terms of stiffness, by changing the elasticity of the SAP and the joint element of the FEM, the entire stiffness matrix is changed. Numerically,

$$E_{SAP} = \beta \times E_{SAP}(nominal) \tag{5.4}$$

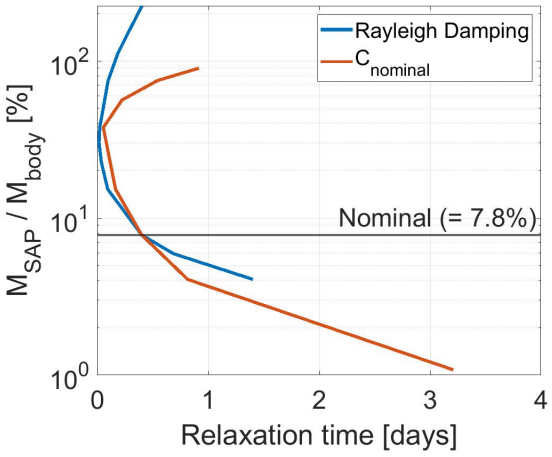

Figure 5.6: ∂M (SC)

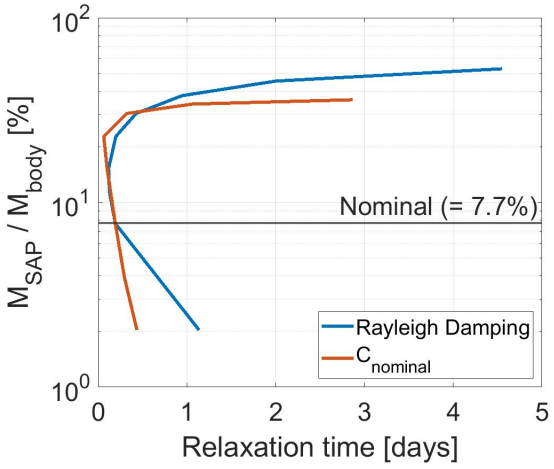

Figure 5.7: ∂M (GOES-α)

$$\beta = 1.0e^{-4} \sim 2.0 \tag{5.5}$$

Figures. 5.8 and 5.9 shows simulation results. The comparison of the damping matrix is highlighted with color as well. Vertical axes are set as an elastic parameter of the SAP element with a log scale. Horizontal axes show relaxation time. In terms of shapes of curves, both figure are similar to each other. As elasticity is decreased, at a particular point, relaxation times are exponentially decreased. Their points are at 10^{-4} in Fig. 5.8 and at 10^{-3} in Fig. 5.9, respectively. But the variation of relaxation times are different from each other. For example, for the simple satellite case, the range of change is 2 [hours]. For the GOES-α case, the range is small such as 0.2 [hours]. When it is compared as a damping matrix, the nominal case does not change relaxation time for both figures. From here, the decreasing is caused by the Rayleigh damping matrix rather dynamics of stiffness in the damping equation.

5.5.2 Change of Joint Stiffness

Simple Satellite model

Next, the joint stiffness is changed and relaxation times are compared. Numerically, the variations are caused by the change of elasticity of the joint element. As in the mass and SAP

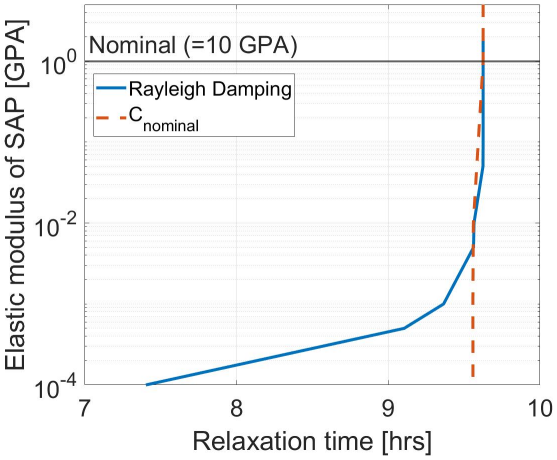

Figure 5.8: ∂K (SAP, SC)

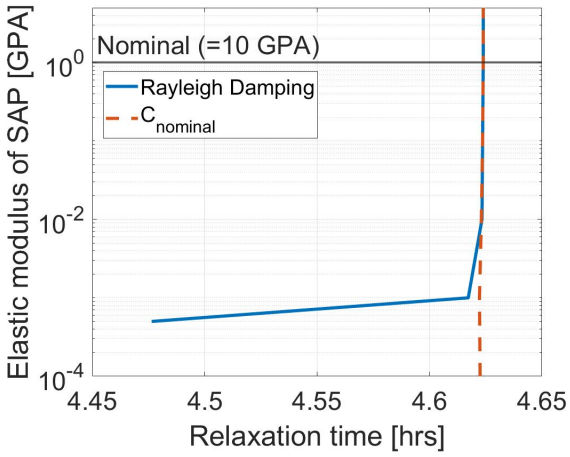

Figure 5.9: ∂K (SAP, GOES-α)

stiffness case, by changing parameters of the element, the entire matrix is changed as well.

$$E_{joint} = \beta \times E_{joint}(nominal) \tag{5.6}$$

$$\beta = 0.50 \sim 10$$

Figure 5.10 and 5.11 show energy dissipation curves with log scale plot. Due to the limit of computational analysis and the sensitivity of the joint, even if the range of β is small, the relaxation times are changed largely. Figure 5.10 shows Rayleigh damping cases and Fig. 5.11 shows constant damping cases. From these figures, we can see that joint stiffness is dominant to change relaxation times. But we cannot see the difference with the kind of damping matrix.

Next, Fig. 5.12 shows a comparison of relaxation time with Rayleigh and nominal damping cases. Here, we can see that in the larger stiffness case, the Rayleigh damping affects the relaxation time strongly. But, in the smaller case on the top left, we cannot see the difference.

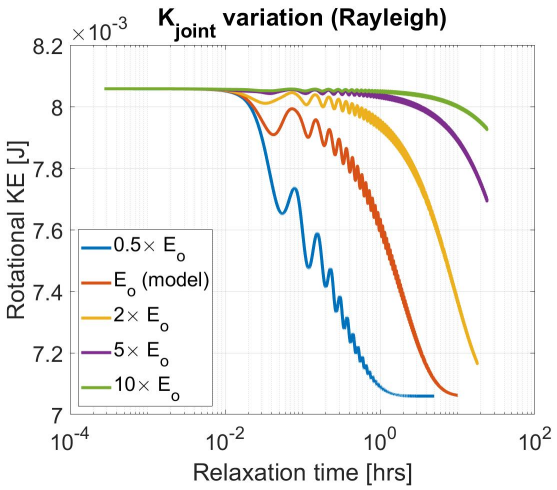

Figure 5.10: ∂K (joint, SC, Rayleigh)

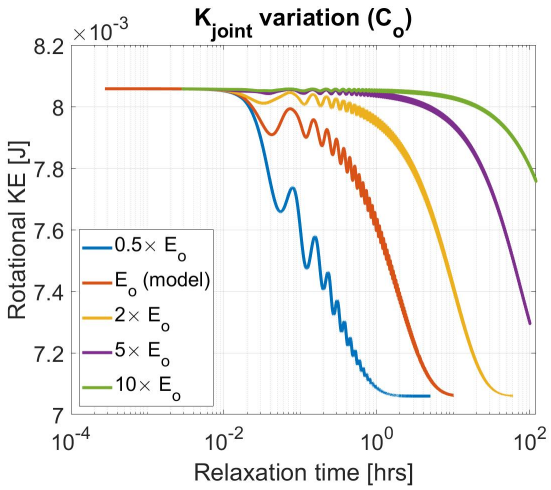

Figure 5.11: ∂K (joint, SC, Nominal)

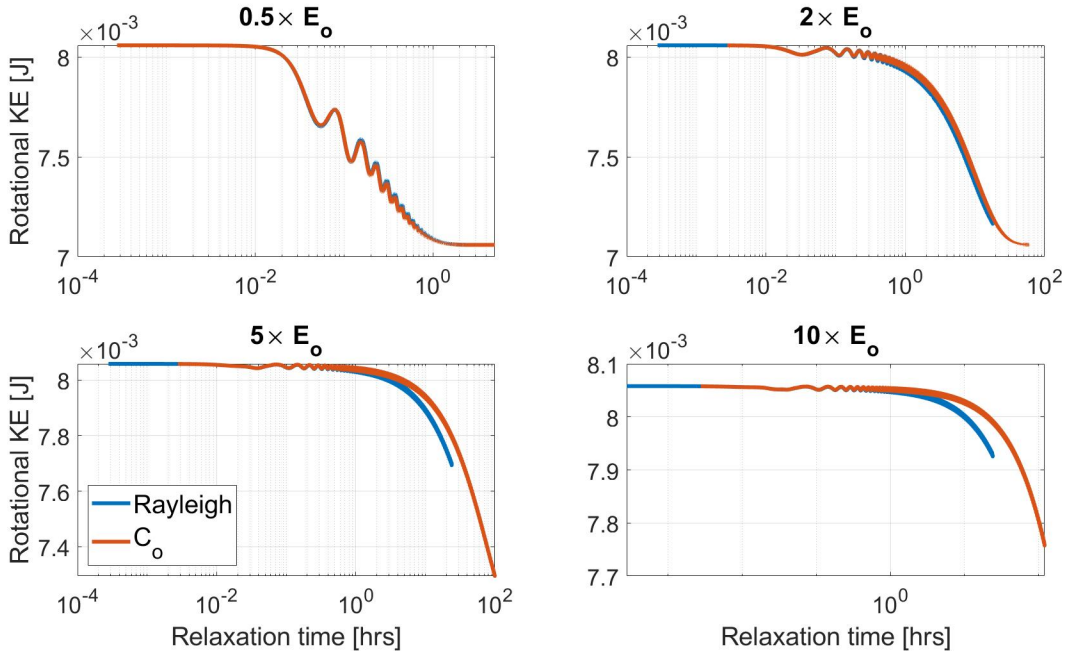

Figure 5.12: Comparison Relaxation Time (∂K, joint, SC)

GOES-α model

The same as the simple satellite case, the sensitivity of the joint element in GOES-α is explored. Figure 5.13 and 5.14 show energy dissipation curves with log scale plot. The beta is changed from $0.75 \sim 100$ in Eq. 5.7. Figure 5.13 shows the Rayleigh damping case and Fig. 5.14 shows the constant damping case. In both cases, strong stiffness cases need longer relaxation time. The range of relaxation times are large as horizontal axes. On the other hand, there is not difference with curves between the two figures.

Again, the below figure shows a comparison of relaxation time with Rayleigh and nominal damping

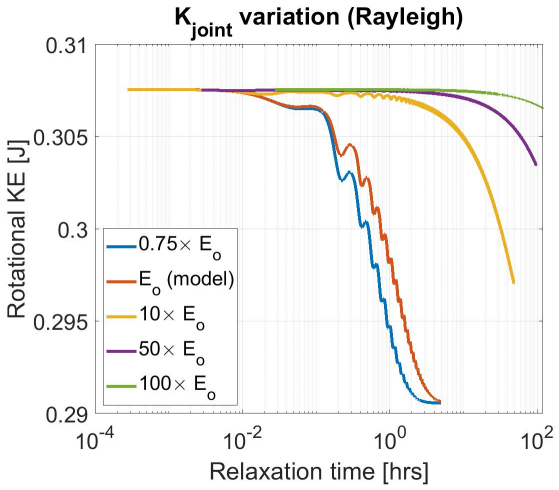

Figure 5.13: ∂K (joint, GOES-α, Rayleigh)

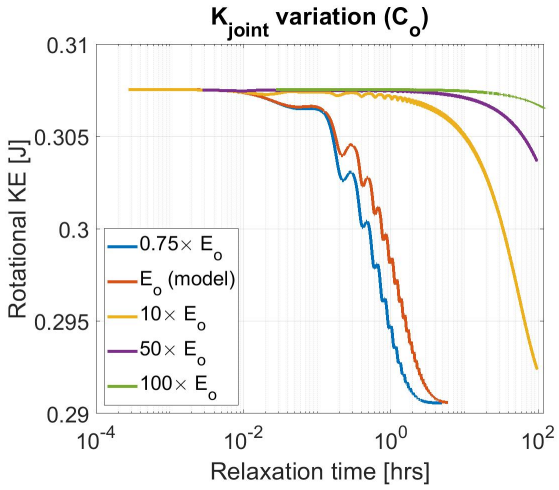

Figure 5.14: ∂K (joint, GOES-α, Nominal)

cases. On the other hand, with simple satellite case as shown in Fig. 5.12, we cannot see the difference with two cases. From here, the stiffness of the joint is dominant cause of the change of the relaxation times longer. If the stiffness of a system decreases, damping will be more affects on the K matrix $[K]$ within damping equation rather than damping matrix $[C]$.

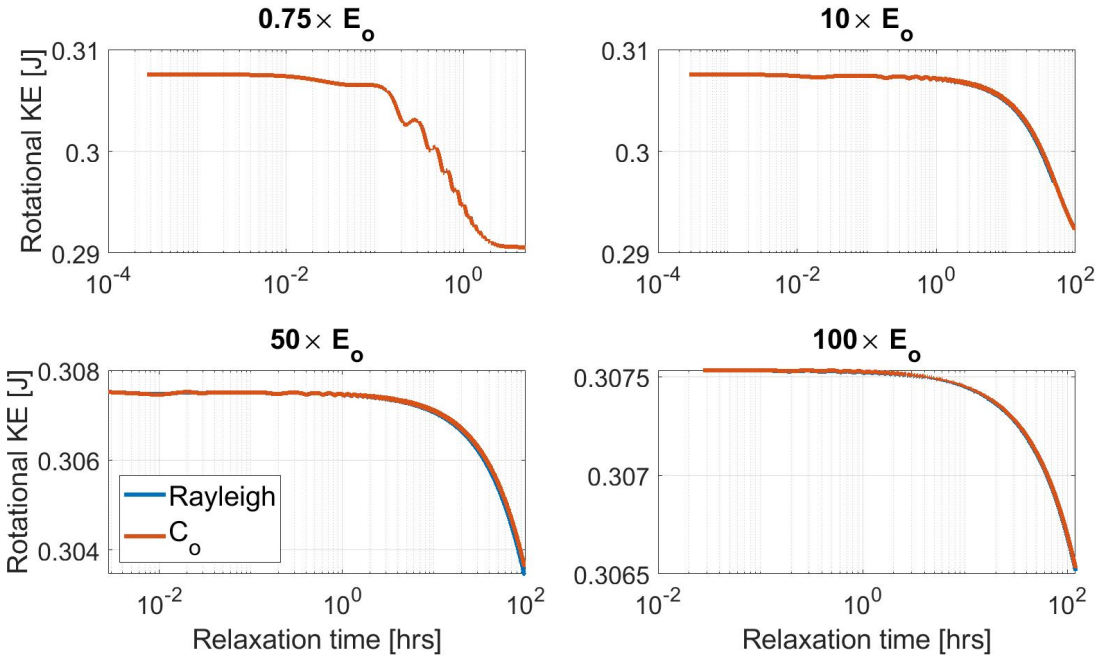

Figure 5.15: Comparison Relaxation Time (∂K, joint, GOES-α)

Discussions

In the additional case, the sensitivity of the stiffness of the joint element 2 is explored, which is a connection between the body and the SAP. Since this portion is a unique component of GOES-α, this analysis is not comparable between the simple satellite case and GOES-α. Figure 5.16 shows this. Relaxation times are scaled along the horizontal axes. Again, the strong stiffness cases need a longer relaxation time, because it does not be fluctuated much and there is not much dissipated energy. In terms of the change of the damping matrices, there is not much difference between of them. At least, we can see that the K matrix within the damping equation affects relaxation time rather the damping matrix directly.

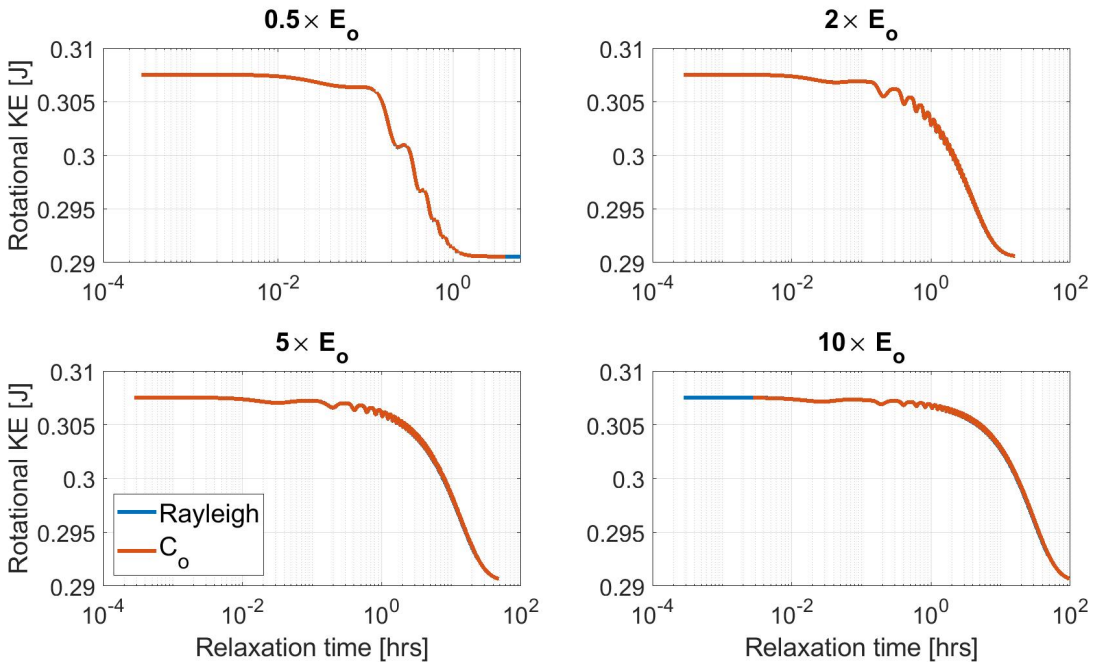

Figure 5.16: Comparison Relaxation Time (∂K, joint 2, GOES-α)

5.6 Short summary

In this chapter, I discussed the sensitivity on the relaxation time of de-tumbling and energy dissipations. As already discussed previous chapters, deformation and fluctuations are varied with the parameter setting. Therefore, by changing the density and elasticity of material, each relaxation times are evaluated. In the sensitivity analysis, input is element parameters which change mass and stiffness matrices, through integrating of the dynamics, relaxation times are compared. In addition to the change of the element values of the FEM, sensitivity of the damping matrix is investigated. In terms of the mass sensitivity, it is found that if the SAP is much heavier or lighter with respect to the body, the relaxation times get longer. This found is a common between the simple satellite model and GOES-α model. Compared to mass change, we can guess stiffness change is more dominant. The variations of SAP stiffness and component of joint are investigated via sensitivity analysis. These simulations provided us how dominant stiffness works on the energy dissipation.

Chapter 6

Conclusions and Future Work

Overall this thesis discussed the interaction between de-tumbling and ~~its~~ internal energy dissipation of a defunct satellite. ~~Around~~ the increasing the amount of ~~the~~ debris ~~problem~~, ~~a~~ tumbling state of space object~~s~~ was considered. Analysis motived by ground observations has shown that the YORP effect is considered to be one cause of spin rate change in celestial bodies. Especially, in a recent study, Albuja et al explored the YORP effect for ~~the~~ defunct satellites in GEO, such as GOES 8 and 10. They proposed that energy dissipation plays an important role to understand the dynamics of a tumbling satellite since ~~only~~ external torque modeling cannot capture tumbling mechanism perfectly.

For this research ~~back ground~~, this thesis developed a model~~ing~~ of energy dissipations from structural approach. ~~Especially,~~ deformation of ~~the~~ defunct satellite~~s~~ modeled with a FEM method that include flexible and damping modes ~~were focused~~. To explore internal energy dissipations, this thesis set two levels, basic and advance. The first was modeling ~~with~~ a simple satellite model and the second was applications to actual ~~project~~ model~~s with~~ adjusting physical parameters. Firstly, using a simple satellite with flexible appendages, energy dissipations of a tumbling body were modeled in chapter 2. By adding three dimensional acceleration to this model, tumbling motion and deformation were simulated. In combination with the FEM and flexible body theory, the inertia matrix and the time derivative of the inertia matrix can be updated. This process simulated the interaction between the deformation and its spin rate. The analytical background of energy dissipation was also explained in chapter 2. In chapter 3, numerical simulations and its

analysis of energy dissipations were demonstrated. Different spin rates, tumbling parameters, and the damping ratio were evaluated with numerical simulations. Through discussions in chapter 2 and 3, I explored a few simple scaling relations predicted by a simple satellite model, and confirmed that this more general tumbling body with dissipation follows some basic scaling rules for how fast it dissipates energy. I found that this model is possible to analyze the expected tumbling behavior of defunct satellites.

For the advance level, I developed another analysis model with FEM based on GOES 10 ~~parameters from open source~~. Since the parameters of GOES ~~details~~ are not ~~open~~ed, some assumptions ~~supported to~~ simulating a de-tumbling of ~~actual~~ GOES. For space missions, sloshing is thought as one cause to dissipate energy as an internal effects. Therefore, using a basic sloshing theory, GOES de-tumbling was reenacted and compared with my hypothesis in chapter 4. In terms of actual space satellite, internal energy dissipations are not caused by single factor but ~~more~~. Therefore, to adjust more complex situation of dissipating energy, ~~as~~ a hybrid case ~~were~~ considered, which was a combination with deformations and sloshing within one system. Through this hybrid simulation, we saw how these causes are contributed and interacted to energy dissipation of tumbling GOES. Under our assumptions, we found that structural damping was more dominant than sloshing analysis.

To find how structural damping contribute de-tumbling and energy dissipation, sensitivity analysis was conducted in chapter 5. Since this thesis uses the damping equation, such as $\left([M]\,\ddot{X} + [C]\,\dot{X} + [K]\,X = F\right)$, to take damping effects on tumbling, each matrix was target of sensitivity analysis. Also, when it is considered to broaden the energy dissipation model, variations of mass and stiffness are significant ~~on this~~ dynamics. Therefore, by checking behaviors of mass and stiffness change of the analysis model, crucial information ~~were~~ found. Rayleigh damping ($[C] = \alpha\,[M] + \beta\,[K]$) provided us the variation of damping matrix as well as the change of the mass and stiffness matrices.

In terms of the mass sensitivity, We found that the change of the mass ratio between the body and the SAP, $\left(\frac{M_{SAP}}{M_{body}}\right)$, effects ~~on~~ rotational dynamics and the relaxation time. It is found

that if the SAP was much heavier or lighter with respect to the body, the relaxation times got longer. Through the sensitivity analysis of elasticity, we found that the stiffness variations affects relaxation time more than mass sensitivity. Especially, the joint flexibility was the biggest factor on the energy dissipation.

In addition to the mass and stiffness sensitivity, damping variations were also evaluated. Even if dynamic equation was same, damping term variation, such as ($[C] =$, constant $[C_0]$ or $[\partial C]$), caused the change of the relaxation time. For the SAP stiffness, damping term ($[C]$) in the damping equation was important. But for the joint stiffness, $[\partial K]$ was more important than damping term in the equation. Discovering these trends can contribute accuracy of the modeling energy dissipation. These founding are brought with benefit of FEM analysis, because FEM can change parameters setting of material and size easily.

In this ~~paper~~, the analytical model was developed from the simple satellite to GOES-α. Then, in this work, the analysis models of the satellites were made up of the main rigid body, the SAP, and the joints that connect of them. By changing the combination of these three parts, it can be applied to other satellite shapes and structures. For example, we showed the possibility of estimating the de-tumbling and relaxation time of a space object that is only a thin film of SAP, or only the arm part of a robot that had turned into debris from space missions. In addition, we can track the dynamic behavior of debris, even if the remaining fuel of the satellite is unknown, or even if there are changes in structural materials and errors in parameters.

Although the time span is different with satellite case, we can understand the dynamics of the asteroid by designing the FEM model by combining plate, rigid and joint elements.

Future Work

- Mesh and Related Problem in the FEM

  In numerical analysis, while increasing the number of meshes improves analysis accuracy, it is a common problem that calculation time increases. In this thesis, the validity of the FEM modeling was evaluated using a FEM software ABAQUS, and then the main analysis

was performed. Of course, I know that the finer the mesh, the more accurate the analysis. On the other hand, it is also an advantage of FEM to be able to increase the number of meshes in order to improve the analysis accuracy.

- Simulation Time

  Physically, in oscillation problems, the smaller resistance to oscillation or vibration, the longer it takes to stabilize. Also, in the analysis, the smaller damping term, the relaxation time gets longer and the analysis time as well. When we run dynamics of simulations with a simple model,

$$\ddot{x} = \frac{1}{m}\left(f - c\dot{x} - kx\right) \tag{6.1}$$

  As completely zero term of damping $\left(\frac{c}{m}\right)$ makes simulations easy, but it does not satisfied with physical problems of rotation. On the other hand, when we take the small damping of a system the $\left(\frac{c}{m}\right)$ term getting small as well. Therefore, resistance to the $\ddot{x}$ is getting less, and relaxation time get longer. In addition, as mentioned above, this research uses FEM approach. Then the finer the mesh, the larger matrices of $[M]$ and $[K]$, and the longer the computation time. If the relaxation of rotating space objects is extremely small and its de-tumbling is modeled by the damping equation, the damping term must be extremely small as well. This resulted in longer simulation times and computational storage limitations as mentioned in the previous chapters. In addition to the problem that increasing the FEM mesh increases the analysis time, there is also the problem that even small damping increases the simulation time. Analysis targeting flexible structures without including the attenuation term is also conceivable, but it is not possible to model the energy dissipation as in this study.

- Asteroid

  Considering two items described as above, as I have wrote several times, asteroid de-

tumbling is also a hot research area. Studies considering FEM and mesh are also being conducted. However, in order to model using the damping equations, an approach is needed to reduce computation time. In this analysis, the main analysis was several hours to hundreds of days, but in the case of asteroids, the time span is thousands to hundreds of years.

- Sloshing and Material Properties

  In this paper, I adopt a simple sloshing model and it supported modeling of GOES de-tumbling and other discussions. Currently, various studies have been conducted on the dynamics of the liquid inside the satellite system. In addition, materials in the structure of satellites are also being studied by many researchers. It is necessary to incorporate the latest research and update to capture precise model with the combination of energy dissipation. However, if we understand the parameters and dynamics of the latest research on sloshing and space material, I would believe that it can be captivated by the model of this research, which is also an advantage of this thesis topic.

- Spin Up of GOES

  In this work, I designed the GOES-α model based on open source information with FEM. In addition, the energy dissipation modeling was verified by comparing with one de-tumbling case of GOES 10. However, researchers found GOES repeat of spin up and down. Therefore, this study focused on a part of GOES tumbling sequence. To understand full dynamics of GOES spinning, not only de-tumbling, but also the start of a tumbling situation should be added on modeling of energy dissipation.

- Adaptability for Other Satellites

  This study focuses on a behavior of a large defunct satellite. This is because of priority of target model. In ADR research trends, first, the removal of large debris has a higher priority

than that of small debris. This is because large debris has a higher risk of colliding with an operational satellite than smaller debris. As I mentioned in conclusion, only one case of physical parameters of GOES was designed and verified with my hypothesis. Also it was stated that my energy dissipation model can be applied to other satellites by combining the body, SAP, and joint element. However, it has not been verified whether it can be applied to satellites having antennas or complicated shapes. Also, the physical parameters of the satellite are needed when applying to other target debris or defunct satellites. In addition, to improve the accuracy of this modeling, it is necessary to obtain the physical parameters of the target model and its data that can confirm the state of de-tumbling.

Bibliography

[1] Orbital debris quaterly news. 26(1), 2022.

[2] R.L. Cognion W. Ryan A. Albuja, D.J. Scheeres and E.V. Ryan. The YORP effect on the GOES 8 and GOES 10 satellites: A case study. Advances in Space Research, 61:122–144, 2018.

[3] Antonella A Albuja, Daniel J Scheeres, and Jay W McMahon. Evolution of angular velocity for defunct satellites as a result of YORP: An initial study. Advances in Space Research, 56(2):237–251, 2015.

[4] Vladimir S Aslanov. Dynamics of a satellite with flexible appendages in the coulomb interaction. Journal of Guidance, Control, and Dynamics, 41(2):565–572, 2018.

[5] Klaus Jurgen Bathe. Finite element procedures. Klaus-Jurgen Bathe, 2006.

[6] Jean-Louis Batoz, Klaus-JÜRgen Bathe, and Lee-Wing Ho. A study of three-node triangular plate bending elements. International journal for numerical methods in engineering, 15(12):1771–1812, 1980.

[7] Conor J Benson and Daniel J Scheeres. Averaged solar torque rotational dynamics for defunct satellites. Journal of Guidance, Control, and Dynamics, 44(4):749–766, 2021.

[8] Conor J Benson, Daniel J Scheeres, William H Ryan, and Eileen V Ryan. Cyclic complex spin state evolution of defunct geo satellites. Proceedings of the Advanced Maui Optical and Space Surveillance Technologies Conference, Maui, HI, 2018.

[9] Conor J Benson, Daniel J Scheeres, William H Ryan, Eileen V Ryan, and Nicholas A Moskovitz. GOES spin state diversity and the implications for geo debris mitigation. Acta Astronautica, 167:212–221, 2020.

[10] R. Bouc. Forced vibration of mechanical systems with hysteresis. In Proceedings of the 4th Conference on Nonlinear Oscillations,, page 315, Prague, Czechoslovakia,1967.

[11] S Breiter and M Murawiecka. Tumbling asteroid rotation with the YORP torque and inelastic energy dissipation. Monthly Notices of the Royal Astronomical Society, 449(3):2489–2497, 2015.

[12] Joseph A Burns, VS Safronov, and T Gold. Asteroid nutation angles. Monthly Notices of the Royal Astronomical Society, 165(4):403–411, 1973.

[13] Masakatsu Chiba and Hidetaka Magata. Influence of liquid sloshing on dynamics of flexible space structures. Journal of Sound and Vibration, 401:1–22, 2017.

[14] ER Christensen and SW Lee. Nonlinear finite element modeling of the dynamics of unrestrained flexible structures. Computers & structures, 23(6):819–829, 1986.

[15] JE Cochran Jr and PH Shu. Effects of energy addition and dissipation on dual-spin spacecraft attitude motion. Journal of Guidance, Control, and Dynamics, 6(5):368–373, 1983.

[16] Guido de Matteis and Luciano M de Socio. Dynamics of a tethered satellite subjected to aerodynamic forces. Journal of guidance, control, and dynamics, 14(6):1129–1135, 1991.

[17] SS Deshpande, SR Rawat, NP Bandewar, and MY Soman. Consistent and lumped mass matrices in dynamics and their impact on finite element analysis results. Intern. J. of Mechanical Engineering and Technology (IJMET), 7(2):135–147, 2016.

[18] Kessler Donald J. Collisional cascading: The limits of population growth in low earth orbit. Advances in Space Research, 11(1):63–66, 1991.

[19] Xiang-Rong Fu, Ming-Wu Yuan, and Chen Pu. A conforming triangular plane element with rotational degrees of freedom. Mathematical Problems in Engineering, 2015, 2015.

[20] Tadanori Fukushima, Daisuke Hirata, Kazuma Adachi, Yuki Itaya, Jun Yamada, K Tsuno, T Ogawa, N Saito, M Sakashita, S Wada, et al. End of life deorbit service with a pulsed laser onboard a small satellite. In Proceedings of the 8th European Conference on Space Debris, 2021.

[21] Michel Géradin and Alberto Cardona. Flexible multibody dynamics: a finite element approach. Wiley, 2001.

[22] Hamza Guenfoud, Mohamed Himeur, Hassina Ziou, and Mohamed Guenfoud. A consistent triangular thin flat shell finite element with drilling rotation based on the strain approach. International Journal of Structural Engineering, 9(3):191–223, 2018.

[23] David M Hamby. A review of techniques for parameter sensitivity analysis of environmental models. Environmental monitoring and assessment, 32(2):135–154, 1994.

[24] Alan W Harris. Tumbling asteroids. Icarus, 107(1):209–211, 1994.

[25] E Harvie, A Dress, and M Phenneger. GOES on-orbit storage mode attitude dynamics and control. Advances in the Astronautical Sciences, 103(2):1095–1114, 1999.

[26] Weipeng Hu, Qingjun Li, Xianhong Jiang, and Zichen Deng. Coupling dynamic behaviors of spatial flexible beam with weak damping. International Journal for Numerical Methods in Engineering, 111(7):660–675, 2017.

[27] Weipeng Hu, Mingzhe Song, and Zichen Deng. Energy dissipation/transfer and stable attitude of spatial on-orbit tethered system. Journal of Sound and Vibration, 412:58–73, 2018.

[28] Kosei Ishimura and Ken Higuchi. Coupling between structural deformation and attitude motion of large planar space structures suspended by multi-tethers. Acta Astronautica, 60(8-9):691–710, 2007.

[29] John L Junkins and Youdan Kim. Introduction to dynamics and control of flexible structures. American Institute of Aeronautics and Astronautics, 1993.

[30] John L Junkins and Hanspeter Schaub. Analytical mechanics of space systems. American Institute of Aeronautics and Astronautics, 2009.

[31] Bogumił Kamiński, Michał Jakubczyk, and Przemysław Szufel. A framework for sensitivity analysis of decision trees. Central European journal of operations research, 26(1):135–159, 2018.

[32] M Keshmiri, AK Misra, and VJ Modi. General formulation for n-body tethered satellite system dynamics. Journal of Guidance, Control, and Dynamics, 19(1):75–83, 1996.

[33] Yasushi Kojima, Shigemune Taniwaki, and Yoshiaki Okami. Dynamic simulation of stick–slip motion of a flexible solar array. Control Engineering Practice, 16(6):724–735, 2008.

[34] K. Komatsu. Mechanical structure vibration engineering (in Japanese). Morikita Publishing Co., Ltd, Tokyo, 2012.

[35] Young W Kwon and Hyochoong Bang. The finite element method using MATLAB. CRC press, 2018.

[36] Benjamin Joseph Lazan. Damping of materials and members in structural mechanics. PERGAMON PRESS LTD, OXFORD, ENGLAND. 1968, 317, 1968.

[37] Gangqiang Li, Zheng H Zhu, and SA Meguid. Libration and transverse dynamic stability control of flexible bare electrodynamic tether systems in satellite deorbit. Aerospace Science and Technology, 49:112–129, 2016.

[38] Peter W Likins. Effects of energy dissipation on the free body motions of spacecraft. 1966.

[39] Stephen C Lowry, Alan Fitzsimmons, Petr Pravec, David Vokrouhlickỳ, Hermann Boehnhardt, Patrick A Taylor, Jean-Luc Margot, Adrian Galád, Mike Irwin, Jonathan Irwin, and Peter Kusnirák. Direct detection of the asteroidal YORP effect. science, 316(5822):272–274, 2007.

[40] Martha Mejía-Kaiser. IADC space debris mitigation guidelines. pages 381–389, 2020.

[41] AK Misra. Dynamics and control of tethered satellite systems. Acta Astronautica, 63(11-12):1169–1177, 2008.

[42] Shinichiro Nishida, Satomi Kawamoto, Yasushi Okawa, Fuyuto Terui, and Shoji Kitamura. Space debris removal system using a small satellite. Acta Astronautica, 65(1-2):95–102, 2009.

[43] F Orban. Damping of materials and members in structures. In Journal of Physics: Conference Series, volume 268, page 012022. IOP Publishing, 2011.

[44] P Papushev, Yu Karavaev, and M Mishina. Investigations of the evolution of optical characteristics and dynamics of proper rotation of uncontrolled geostationary artificial satellites. Advances in Space Research, 43(9):1416–1422, 2009.

[45] Carmen Pardini and Luciano Anselmo. Environmental sustainability of large satellite constellations in low earth orbit. Acta Astronautica, 170:27–36, 2020.

[46] Kevin H Prendergast. Proceedings of the celestial mechanics conference: The effects of imperfect elasticity in problems of celestial mechanics. The Astronomical Journal, 63:412, 1958.

[47] Christopher D Rahn and Peter M Barba. Reorientation maneuver for spinning spacecraft. Journal of guidance, control, and dynamics, 14(4):724–728, 1991.

[48] I Ramu and SC Mohanty. Study on free vibration analysis of rectangular plate structures using finite element method. Procedia engineering, 38:2758–2766, 2012.

[49] Aaron J Rosengren, Despoina K Skoulidou, Kleomenis Tsiganis, and George Voyatzis. Dynamical cartography of earth satellite orbits. Advances in Space Research, 63(1):443–460, 2019.

[50] David Parry Rubincam. Radiative spin-up and spin-down of small asteroids. Icarus, 148(1):2–11, 2000.

[51] Ryotaro Sakamoto, Hiroaki Tanaka, and Yoshiro Ogi. Improvement of deployment repeatability by the vibration produced by macro fiber composite actuator. Mechanical Engineering Letters, 2:16–00042, 2016.

[52] H J Schek. The force density method for form finding and computation of general networks. Computer methods in applied mechanics and engineering, 3(1):115–134, 1974.

[53] A M. Solovyov, M E. Semenov, P A. Meleshenko, and A I Barsukov. Bouc-wen model of hysteretic damping. Procedia engineering, 201:549–555, 2017.

[54] Masazumi Ueba and Tetsuo Yasaka. Attitude maneuver of service vehicle with spinning spent satellite. Journal of Guidance, Control, and Dynamics, 17(5):1007–1010, 1994.

[55] Jiangwen Wang, Guiming Mei, and Weihua Zhang. Sensitivity analysis of flexible upper frame of pantograph with a novel simplified method. In The IAVSD International Symposium on Dynamics of Vehicles on Roads and Tracks, pages 181–188. Springer, 2020.

[56] Y. K. Wen. Method for random vibration of hysteretic systems. Journal of the Engineering Mechanics Division, 102(2):249–263, 1976.

[57] Toru Yamamoto, Yu Nakajima, Takahiro Sasaki, Naoki Okada, Misuzu Haruki, and Koji Yamanaka. Gnc strategy to capture, stabilize and remove large space debris. Proceedings of the First International Orbital Debris Conference, 2019.

[58] Man Zhang, Baozhong Sun, and Bohong Gu. Accelerated thermal ageing of epoxy resin and 3-d carbon fiber/epoxy braided composites. Composites Part A: Applied Science and Manufacturing, 85:163–171, 2016.

[59] Bang Zhao Zhou, Guo Ping Cai, Yun Meng Liu, and Pan Liu. Motion prediction of a non-cooperative space target. Advances in Space Research, 61(1):207–222, 2018.

Appendix A

Finite Element Method

A.1 Transformation in the FEM

To determinate the element stiffness matrix $[K_e]$ to global coordinates requires the introduction of a transformation from local $\left[K^l\right]$ to global $[K^g]$. If the rotational matrix $[T]$ is orthogonal, then we have

$$[K_e^g] = \left[T^T\right] \left[K_e^l\right] [T] \tag{A.1}$$

which is the general relationship between element stiffness matrix in local and global coordinates. Superscript T stands for transpose matrix. The problem confronting us is the general transformation of a vector $\vec{V}'s$ from (x, y, z) coordinate system to $(\bar{X}, \bar{Y}, \bar{Z})$. Here, (x, y, z) is a local frame and $\bar{X}$, $\bar{Y}$, and $\bar{Z}$ is the global (body) frame. Unit vectors in the global frame are

$$\hat{X} = \begin{bmatrix} 1 \\ 0 \\ 0 \end{bmatrix}, \ \hat{Y} = \begin{bmatrix} 0 \\ 1 \\ 0 \end{bmatrix}, \ \hat{Z} = \begin{bmatrix} 0 \\ 0 \\ 1 \end{bmatrix} \tag{A.2}$$

Then $\vec{V}'s$ are expressed with these unit vectors in the global frame,

$$\vec{V_1} = X_1\hat{X} + Y_1\hat{Y} + Z_1\hat{Z} \tag{A.3}$$

$$\vec{V_2} = X_2\hat{X} + Y_2\hat{Y} + Z_2\hat{Z} \tag{A.4}$$

$$\vec{V_3} = X_3\hat{X} + Y_3\hat{Y} + Z_3\hat{Z} \tag{A.5}$$

Recalling that the dot product of two vectors

$$\vec{A} \cdot \vec{B} = |\vec{A}| \cdot |\vec{B}| \cos\alpha \tag{A.6}$$

The vector can be normalized

$$\hat{x} = \frac{\vec{V_x}}{|\vec{V_x}|},\ \hat{y} = \frac{\vec{V_y}}{|\vec{V_y}|},\ \hat{x} = \frac{\vec{V_z}}{|\vec{V_z}|} \tag{A.7}$$

Then, the transformation matrix is defined as

$$[T] = \begin{bmatrix} \hat{x}\cdot\hat{X} & \hat{x}\cdot\hat{Y} & \hat{x}\cdot\hat{Z} \\ \hat{y}\cdot\hat{X} & \hat{y}\cdot\hat{Y} & \hat{y}\cdot\hat{Z} \\ \hat{z}\cdot\hat{X} & \hat{z}\cdot\hat{Y} & \hat{z}\cdot\hat{Z} \end{bmatrix} \tag{A.8}$$

Figure A.1 shows the vector configuration with global frame $(\bar{X}, \bar{Y}, \bar{Z})$ and local frame (x, y, z) with two triangular elements. These two cases are shown as the following examples.

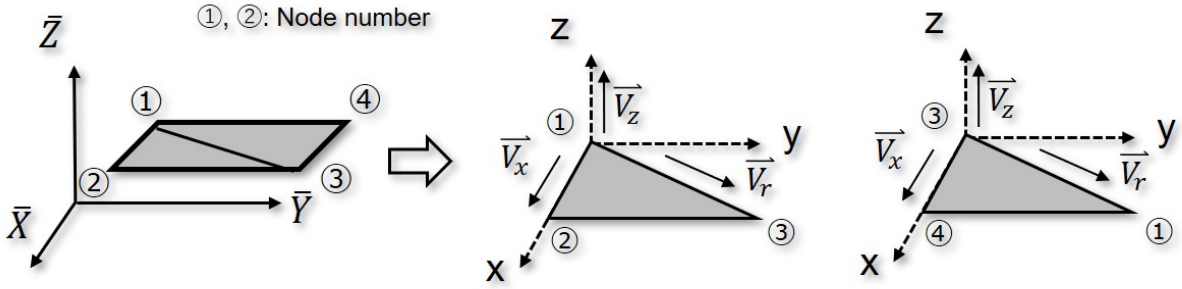

Figure A.1: Configuration of Triangular Element (Global to Local)

Case 1

In the global frame, the three vectors are defined as

$$\vec{V_1} = \begin{bmatrix} 1 \\ 1 \\ 1 \end{bmatrix}^G,\ \vec{V_2} = \begin{bmatrix} 2 \\ 1 \\ 1 \end{bmatrix}^G,\ \vec{V_3} = \begin{bmatrix} 0 \\ 0 \\ 1 \end{bmatrix}^G \tag{A.9}$$

Superscript G stands for global frame. Then, x direction vector $\vec{V_x}$ and its unit vector $\hat{x}$ in the local frame (superscript L) are

$$\vec{V_x} = \vec{V_2} - \vec{V_1} = \begin{bmatrix} 1 \\ 0 \\ 0 \end{bmatrix}^G,\ \hat{x} = \frac{\vec{V_x}}{|\vec{V_x}|} = \begin{bmatrix} 1 \\ 0 \\ 0 \end{bmatrix}^L \tag{A.10}$$

r direction vector in the figure, $\vec{V_r}$ in the global frame is defined as follows.

$$\vec{V_r} = \vec{V_3} - \vec{V_1} = \begin{bmatrix} 1 \\ 1 \\ 0 \end{bmatrix}^G \tag{A.11}$$

$\vec{V_z}$ vector in the global frame and unit vector $\hat{z}$ in the local frame are horizontal vector with V_x and V_r.

$$\vec{V_z} = \vec{V_x} \times \vec{V_r} = \begin{bmatrix} \hat{X} & \hat{Y} & \hat{Z} \\ 1 & 0 & 0 \\ 1 & 1 & 0 \end{bmatrix} = \begin{bmatrix} 0 \\ 0 \\ 1 \end{bmatrix}^G, \hat{z} = \frac{\vec{V_z}}{|\vec{V_z}|} = \begin{bmatrix} 0 \\ 0 \\ 1 \end{bmatrix}^L \tag{A.12}$$

Finally, unit vector along the $\hat{y}$ direction in the local frame is

$$\hat{y} = \hat{z} \times \hat{x} = \begin{bmatrix} \hat{X} & \hat{Y} & \hat{Z} \\ 0 & 0 & 1 \\ 1 & 0 & 0 \end{bmatrix} = \begin{bmatrix} 0 \\ 1 \\ 0 \end{bmatrix}^L \tag{A.13}$$

Transformation matrix is

$$[T] = \begin{bmatrix} 1 & 0 & 0 \\ 0 & 1 & 0 \\ 0 & 0 & 1 \end{bmatrix} \tag{A.14}$$

Case 2

$$\vec{V_1} = \begin{bmatrix} 1 \\ 1 \\ 1 \end{bmatrix}^G, \ \vec{V_3} = \begin{bmatrix} 2 \\ 2 \\ 1 \end{bmatrix}^G, \ \vec{V_4} = \begin{bmatrix} 1 \\ 2 \\ 1 \end{bmatrix}^G \tag{A.15}$$

x direction vector $\vec{V_x}$ in the global frame and unit vector $\hat{x}$ in the local frame are

$$\vec{V_x} = \vec{V_4} - \vec{V_3} = \begin{bmatrix} -1 \\ 0 \\ 0 \end{bmatrix}^G, \ \hat{x} = \frac{\vec{V_x}}{|\vec{V_x}|} = \begin{bmatrix} -1 \\ 0 \\ 0 \end{bmatrix}^L \tag{A.16}$$

r direction vector $\vec{V_r}$ in the global frame is defined as follows.

$$\vec{V_r} = \vec{V_1} - \vec{V_3} = \begin{bmatrix} -1 \\ -1 \\ 0 \end{bmatrix}^G \tag{A.17}$$

$\vec{V_z}$ vector in the global frame and unit vector $\hat{z}$ in the local frame are horizontal vector with V_x and V_r

$$\vec{V_z} = \vec{V_x} \times \vec{V_r} = \begin{bmatrix} \hat{X} & \hat{Y} & \hat{Z} \\ -1 & 0 & 0 \\ -1 & -1 & 0 \end{bmatrix} = \begin{bmatrix} 0 \\ 0 \\ 1 \end{bmatrix}^G, \hat{z} = \frac{\vec{V_z}}{|\vec{V_z}|} = \begin{bmatrix} 0 \\ 0 \\ 1 \end{bmatrix}^L \tag{A.18}$$

Finally, unit vector along the y direction $\hat{y}$ in the local frame is

$$\hat{y} = \hat{z} \times \hat{x} = \begin{bmatrix} \hat{X} & \hat{Y} & \hat{Z} \\ 0 & 0 & 1 \\ -1 & 0 & 0 \end{bmatrix} = \begin{bmatrix} 0 \\ -1 \\ 0 \end{bmatrix}^L \tag{A.19}$$

Transformation matrix is

$$[T] = \begin{bmatrix} -1 & 0 & 0 \\ 0 & -1 & 0 \\ 0 & 0 & 1 \end{bmatrix} \tag{A.20}$$

A.2 Branch Node Matrix

Branch Node Matrix (BNM) is a matrix to indicate the network topology. This theory is used in electrical engineering or in computer science. The connection between the branch and nodes' information is expressed by 0, 1, and -1. For FEM usage, the branch stands for an element. The below figure is a configuration of nodes joined by elements. Arrows are put on each element and node to show the positive direction as vectors. The BNM of this figure has one column for each node and one row for each element. Therefore, the size of BNM is 4×3. The circled numbers indicate the elements numbering.

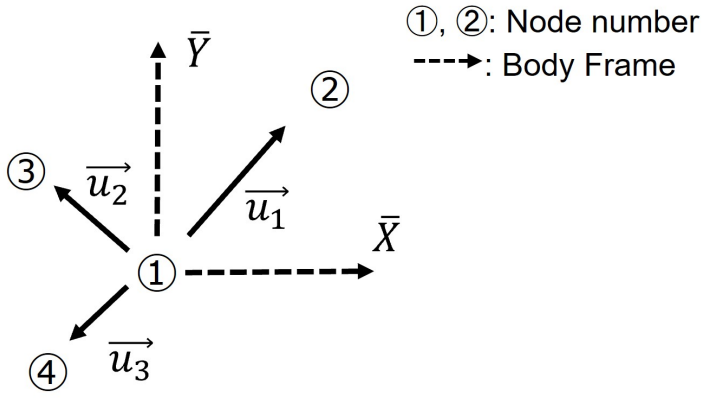

Figure A.2: Displacement Vectors in Branch Node

If an vector runs from node 1 to node 2, the row corresponding to that element has -1 in column 1 and 1 in column 2, all other entries in that row are 0. The components u_i of the $\vec{u}$ describe the displacement of each node of the figure.

$$u_1 = x_2 - x_1 \tag{A.21}$$

$$u_2 = x_3 - x_1 \tag{A.22}$$

$$u_3 = x_4 - x_1 \tag{A.23}$$

This leads to

$$\vec{u} = \begin{bmatrix} u_1 \\ u_2 \\ u_3 \end{bmatrix} = \begin{bmatrix} -1 & 1 & 0 & 0 \\ -1 & 0 & 1 & 0 \\ -1 & 0 & 0 & 1 \end{bmatrix} \begin{bmatrix} x_1 \\ x_2 \\ x_3 \\ x_4 \end{bmatrix} = C_t \vec{x} \tag{A.24}$$

Along the Y axis, let us use $\vec{v}$ is the displacement for the figure.

$$v_1 = y_2 - y_1 \tag{A.25}$$

$$v_2 = y_3 - y_1 \tag{A.26}$$

$$v_3 = y_4 - y_1 \tag{A.27}$$

This leads to

$$\vec{v} = \begin{bmatrix} v_1 \\ v_2 \\ v_3 \end{bmatrix} = \begin{bmatrix} -1 & 1 & 0 & 0 \\ -1 & 0 & 1 & 0 \\ -1 & 0 & 0 & 1 \end{bmatrix} \begin{bmatrix} y_1 \\ y_2 \\ y_3 \\ y_4 \end{bmatrix} = C_t \vec{y} \tag{A.28}$$

Appendix B

Rotational Dynamics

B.1 Acceleration Matrix

An arbitrary angular velocity vector $\vec{\omega}$, is defined as the angular velocity of the body frame relative to the inertial frame. Then, using transport theorem, velocity vectors in the inertial frame are given by

$$ {}^{I}\frac{d}{dt}\vec{r} = {}^{B}\frac{d}{dt}\vec{r} + \vec{\omega} \times \vec{r} \tag{B.1} $$

${}^{I}\frac{d}{dt}$ denotes the inertial derivative, ${}^{B}\frac{d}{dt}$ denotes the time derivative in the body frame, and $\vec{r}$ denotes the position vector in the body frame. Superscript I denotes the inertial derivative, and B denotes the time derivative in the body frame.

$$ \begin{aligned} {}^{I}\frac{d}{dt}\dot{\vec{r}} &= {}^{I}\frac{d}{dt}\left({}^{B}\frac{d}{dt}\vec{r}\right) + {}^{I}\frac{d}{dt}\left(\vec{\omega} \times \vec{r}\right) = {}^{I}\frac{d}{dt}\left({}^{B}\dot{\vec{r}}\right) + {}^{I}\frac{d}{dt}\vec{\omega} \times \vec{r} + \vec{\omega} \times {}^{I}\frac{d}{dt}\vec{r} \\ &= {}^{B}\frac{d}{dt}\left({}^{B}\dot{\vec{r}}\right) + \vec{\omega} \times {}^{B}\dot{\vec{r}} + \dot{\vec{\omega}} \times \vec{r} + \vec{\omega} \times {}^{B}\dot{\vec{r}} + \vec{\omega} \times \vec{\omega} \times \vec{r} \end{aligned} \tag{B.2} $$

$$ {}^{I}\ddot{\vec{r}} = {}^{B}\ddot{\vec{r}} + 2\vec{\omega} \times {}^{B}\dot{\vec{r}} + \dot{\vec{\omega}} \times \vec{r} + \vec{\omega} \times \vec{\omega} \times \vec{r} \tag{B.3} $$

Because there is no additional force in the inertial frame, ${}^{I}\ddot{\vec{r}} = 0$,

$$ {}^{B}\ddot{\vec{r}} = -\vec{\omega} \times \vec{\omega} \times \vec{r} - \dot{\vec{\omega}} \times \vec{r} - 2\vec{\omega} \times {}^{B}\dot{\vec{r}} \tag{B.4} $$

using the rule:

$$ \tilde{a} \cdot \tilde{b} = \vec{b}\vec{a}^{T} - (\vec{a} \cdot \vec{b})I_{3\times 3} \tag{B.5} $$

Therefore,

$$
\begin{aligned}
{}^{B}\ddot{\vec{r}} &= -\left[\vec{\omega}\vec{\omega}^{T} - \omega^{2} I_{3\times 3}\right]\vec{r} - \dot{\vec{\omega}} \times \vec{r} && \text{(B.6)} \\
&= \left[\omega^{2} I_{3\times 3} - \vec{\omega}\vec{\omega}^{T} - \dot{\tilde{\omega}}\right]\vec{r} && \text{(B.7)}
\end{aligned}
$$

The acceleration matrix is

$$
\vec{f}(t) = [\omega^{2} I_{3\times 3} - \vec{\omega}\vec{\omega} - \dot{\tilde{\vec{\omega}}}] \cdot \vec{r} \tag{B.8}
$$

where $\sim$ denotes a skew-symmetric matrix.

B.2 Rotation Axis

The angular momentum vector in the inertial frame is denoted by $\vec{H}$. The satellite body frame is given by $B\,[b_1,\ b_2,\ b_3]$ as shown in Fig. B.1. The rotational kinetic energy T of a single

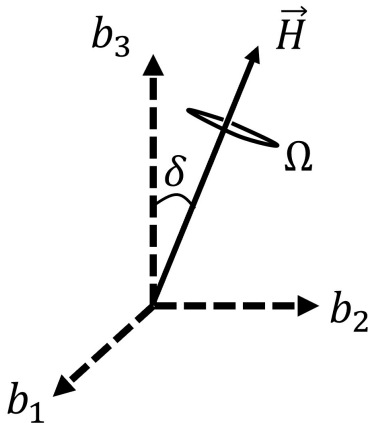

Figure B.1: Angular Momentum $\vec{H}$ and Body Frame

rigid body is given by,

$$
T = \frac{1}{2}\omega^{T}\,[I]\,\omega \tag{B.9}
$$

Using the angular momentum magnitude $H = |\vec{H}|$ and kinetic energy T, the dynamic moment of inertia I_d which is given by,

$$
I_d = \frac{H^2}{2T} \tag{B.10}
$$

Another fundamental quantity is called the effective spin rate ω_e

$$\omega_e = \frac{2T}{H} \tag{B.11}$$

which linearly scales the satellite's angular velocity components. I_d and ω_e yield the familiar looking expressions

$$H = I_d \omega_e,\ T = \frac{1}{2} I_d\ \omega_e^2 \tag{B.12}$$

The rotation matrix is given by BN $= R_3(\sigma t) R_1(\delta)$ where R_i denotes a principal rotation about the i^{th} axis.

$$[R_1(\delta)] = \begin{bmatrix} 1 & 0 & 0 \\ 0 & \cos\delta & \sin\delta \\ 0 & -\sin\delta & \cos\delta \end{bmatrix},\ [R_3(\sigma t)] = \begin{bmatrix} \cos(\sigma t) & \sin(\sigma t) & 0 \\ -\sin(\sigma t) & \cos(\sigma t) & 0 \\ 0 & 0 & 1 \end{bmatrix} \tag{B.13}$$

$$\vec{H}^B = \begin{bmatrix} H_1 \\ H_2 \\ H_3 \end{bmatrix} = R_3(\sigma t) R_1(\delta) \vec{H}^N = \begin{bmatrix} \cos(\sigma t) & \sin(\sigma t)\cos\delta & \sin(\sigma t)\sin\delta \\ -\sin(\sigma t) & \cos(\sigma t)\cos\delta & \cos(\sigma t)\sin\delta \\ 0 & -\sin\delta & \cos\delta \end{bmatrix} \begin{bmatrix} 0 \\ 0 \\ H \end{bmatrix}^N \tag{B.14}$$

$$= \begin{bmatrix} H\sin(\sigma t)\sin\delta \\ H\cos(\sigma t)\sin\delta \\ H\cos\delta \end{bmatrix} = \begin{bmatrix} I_t \\ I_t \\ I_a \end{bmatrix} \boldsymbol{\Omega} \tag{B.15}$$

$$\boldsymbol{\Omega} = H \begin{bmatrix} \frac{1}{I_t}\sin(\sigma t)\sin\delta \\ \frac{1}{I_t}\cos(\sigma t)\sin\delta \\ \frac{1}{I_a}\cos\delta \end{bmatrix} \tag{B.16}$$

Appendix C

Differential Equations

C.1 Homogenuous equation

The general solution of a homogeneous equation is demonstrated.

$$\ddot{x} + \omega_0^2 x = 0 \tag{C.1}$$

Let its solution as $x = e^{\lambda t}$, then

$$\dot{x} = \lambda e,\ \ddot{x} = \lambda^2 e^{\lambda t} \tag{C.2}$$

$$e^{\lambda}\left(\lambda^2 + \omega_0^2\right) = 0 \tag{C.3}$$

$$\lambda^2 = -\omega_0^2,\ \lambda = \pm i\omega_0 \tag{C.4}$$

$$\lambda_1 = i\omega_0,\ \lambda_2 = -i\omega_0 \tag{C.5}$$

Finally,

$$x = e^{i\omega_0 t} + e^{-i\omega_0 t} \tag{C.6}$$

Using the Euler's formula,

$$\begin{aligned} x &= C_1\left(\cos(\omega_0 t) + i\sin(\omega_0 t)\right) + C_2\left(\cos(\omega_0 t) - i\sin(\omega_0 t)\right) \\ &= (C_1 + C_2)\cos(\omega_0 t) + (C_1 - C_2)i\sin(\omega_0 t) \\ &= A\cos(\omega_0 t) + B\sin(\omega_0 t) \end{aligned} \tag{C.7}$$

$A\cos(\omega_0 t) + B\sin(\omega_0 t)$ is the general solution of the differential equation without damping ratio.

C.2 Homogenuous equation with damping factor

$$\ddot{x} + 2\zeta\dot{x} + \omega_0^2 x = 0 \tag{C.8}$$

Same as the above section, let its solution as $x = e^{\lambda t}$, then

$$e^{\lambda}\left(\lambda^2 + 2\zeta\lambda + \omega_0^2\right) = 0$$
$$\lambda_1 = -\zeta + \sqrt{\zeta^2 - \omega_0^2},\ \lambda_2 = -\zeta - \sqrt{\zeta^2 - \omega_0^2} \tag{C.9}$$

Depending on the value of ζ and ω_0, the solution can be categorized as follows.

1 $\underline{\zeta^2 - \omega_0^2 < 0}$

$$\sqrt{\zeta^2 - \omega_0^2} = i\omega$$
$$\lambda_1 = -\zeta + i\omega,\ \lambda_2 = -\zeta - i\omega \tag{C.10}$$

Using Euler's formula,

$$\begin{aligned} e^{\lambda_1 t} &= e^{(-\zeta + i\omega)t} = e^{-\zeta t}e^{i\omega t} \\ &= e^{-\zeta t}(\cos(\omega t) + i\sin(\omega t)) \end{aligned} \tag{C.11}$$

$$\begin{aligned} e^{\lambda_2 t} &= e^{(-\zeta - i\omega)t} = e^{-\zeta t}e^{-i\omega t} \\ &= e^{-\zeta t}(\cos(\omega t) - i\sin(\omega t)) \end{aligned} \tag{C.12}$$

$$x = e^{-\zeta t}\left\{C_1\left(\cos(\omega t) + i\sin(\omega t)\right) + C_2\left(\cos(\omega t) - i\sin(\omega t)\right)\right\} \tag{C.13}$$
$$= e^{-\zeta t}\left\{(C_1 + C_2)\cos(\omega_0 t) + (C_1 - C_2)i\sin(\omega_0 t)\right\} \tag{C.14}$$
$$= e^{-\zeta t}\left\{A\cos(\omega_0 t) + B\sin(\omega_0 t)\right\} \tag{C.15}$$

$e^{-\zeta t}\left\{A\cos(\omega_0 t) + B\sin(\omega_0 t)\right\}$ is the general solution of the differential equation with damping ratio.

2 $\underline{\zeta^2 - \omega_0^2 > 0}$

$$x = Ae^{-\left(\zeta - \sqrt{\zeta^2 - \omega_0^2}\right)t} + Be^{-\left(\zeta + \sqrt{\zeta^2 - \omega_0^2}\right)t} \tag{C.16}$$

3 $\underline{\omega_0 = \zeta}$

The simple solution is $\lambda = \zeta$, but there is another solution to this case. Let us assume $x = a(t)e^{-\lambda t}$

$$\dot{x} = \dot{a}e^{-\zeta t} + (-\zeta)ae^{-\zeta t} = e^{-\zeta t}(\dot{a} - \zeta a) \tag{C.17}$$

$$\begin{aligned} \ddot{x} &= \ddot{a}e^{-\zeta t} + \dot{a}(-\zeta)e^{-\zeta t} + \dot{a}(-\zeta)e^{-\zeta t} + \zeta^2 a e^{-\zeta t} \\ &= e^{-\zeta t}(\ddot{a} - 2\zeta\dot{a} + \zeta^2 a) \end{aligned} \tag{C.18}$$

$$\begin{aligned} e^{-\zeta t}(\ddot{a} - 2\zeta\dot{a} + \zeta^2 a + 2\zeta\dot{a} - 2\zeta^2 a + \omega_0^2 a) &= e^{-\zeta t}\left\{\ddot{a} + a(\zeta^2 - \omega_0^2)\right\} \\ &= 0 \end{aligned} \tag{C.19}$$

Therefore, $At + B$ can be a solution of equation. The general solution of the equation is $x = (At + B)e^{-\zeta t}$

C.3 Non-homogeneous equation

Basically, the general solution of the non-homogeneous equation is solved as general solution of the homogeneous equation plus a particular solution of the non-homogeneous equation. Similar to the above section, the equation includes excitation force, such as

$$\ddot{x} + \omega_0^2 x = f_0 \sin(\omega t) \tag{C.20}$$

Let its solution as $x = a\sin(\omega t)$ then

$$\dot{x} = a\omega\cos(\omega t),\ \ddot{x} = -a\omega^2\sin(\omega t) \tag{C.21}$$

$$a\left\{(\omega^2\sin(\omega t) - \omega_0^2\sin(\omega t)\right\} = -f_0\sin(\omega t) \tag{C.22}$$

$$a = \frac{f_0}{\omega_0^2 + \omega^2} \tag{C.23}$$

The general solution of the equation is

$$x = \frac{f_0}{\omega_0^2 - \omega^2}\sin(\omega t) \tag{C.24}$$

Finally,

$$x = e^{i\omega_0 t} + e^{-i\omega_0 t} \tag{C.25}$$

The solution with damping ratio (ζ) such as

$$\ddot{x} + 2\zeta\dot{x} + \omega_0^2 x = f_0 \sin(\omega t) \tag{C.26}$$

Let its solution as $x = a\cos(\omega t) + b\sin(\omega t)$ then

$$\dot{x} = -a\omega\sin(\omega t) + b\omega\cos(\omega t) \tag{C.27}$$

$$\ddot{x} = -a\omega^2\cos(\omega t) - b\omega^2\sin(\omega t) \tag{C.28}$$

Then the equation is

$$\left\{-a\omega^2 + 2\zeta b\omega + a\omega_0^2\right\}\cos(\omega t) + \left\{-b\omega^2 - 2\zeta a\omega + b\omega_0^2\right\}\sin(\omega t) = f_0\sin(\omega t) \tag{C.29}$$

$$a(\omega_0^2 - \omega^2) + 2\zeta b\omega = 0 \tag{C.30}$$

$$b(\omega_0^2 - \omega^2) + 2\zeta a\omega = f_0 \tag{C.31}$$

when solving the above equation, a and b are defined as

$$a = \frac{-2\zeta\omega f_0}{\left(\omega_0^2 - \omega^2\right)^2 + 4\zeta^2\omega^2},\ b = \frac{\left(\omega_0^2 - \omega^2\right) f_0}{\left(\omega_0^2 - \omega^2\right)^2 + 4\zeta^2\omega^2} \tag{C.32}$$

Finally the solution is as follows

$$x = \frac{f_0}{\left(\omega_0^2 - \omega^2\right)^2 + 4\zeta^2\omega^2}\left\{-2\zeta\omega\cos(\omega t) + (\omega_0^2 - \omega^2)\sin(\omega t)\right\} + general\ solution \tag{C.33}$$

C.4 Oscillation case

$$\ddot{z} + 2\zeta\omega_o\dot{z} + \omega_o^2 z = \frac{\omega_l^2 I_D^2 r}{2I_t I_a}\sin 2\delta\cos(\omega t) \tag{C.34}$$

where z is the out-of-plane coordinate, assumed to be small or $z \ll r$, ζ is the damping ratio of the element, and ω_o represents the natural frequency of the system. We note that in actuality there

are multiple natural frequencies present and that the driving frequency tends to be much smaller than the system natural frequencies, or $\omega_o \gg \sigma \sim \omega_l$. Let its general solution as $z = e^{\lambda t}$, then

$$\dot{z} = \lambda e^{\lambda t},\ \ddot{z} = \lambda^2 e^{\lambda t} \tag{C.35}$$

$$e^{\lambda t}\left(\lambda^2 + 2\zeta\omega_0\lambda + \omega_0^2\right) = 0 \tag{C.36}$$

$$\lambda = -\zeta\omega_0 \pm \sqrt{\zeta^2\omega_0^2 - \omega_0^2} = -\zeta\omega_0 \pm \omega_0\sqrt{\zeta^2 - 1} \tag{C.37}$$

$$\lambda_1 = \left(-\zeta + i\sqrt{1-\zeta^2}\right)\omega_0,\ \lambda_2 = \left(-\zeta - i\sqrt{1-\zeta^2}\right)\omega_0 \tag{C.38}$$

Using Euler's formula, the general solution of a homogeneous equation is

$$z = e^{-\zeta\omega_0 t}\left(C\cos(\omega_0\sqrt{1-\zeta^2}t) + D\sin(\omega_0\sqrt{1-\zeta^2}t)\right) \tag{C.39}$$

In addition, the general solution of non-homogeneous equation is assumed as $z = A\sin(\omega t) + B\cos(\omega t)$ then

$$\dot{z} = A\omega\cos(\omega t) - B\omega\sin(\omega t) \tag{C.40}$$

$$\ddot{z} = -A\omega^2\sin(\omega t) - B\omega^2\cos(\omega t) \tag{C.41}$$

Let $\frac{\omega_l^2 I_D^2 r}{2I_t I_a}\sin 2\delta = f$, then equation is

$$\left\{-A\omega^2 - 2\zeta B\omega\omega_0 + A\omega_0^2\right\}\sin(\omega t) + \left\{-B\omega^2 - 2\zeta A\omega\omega_0 + B\omega_0^2\right\}\cos(\omega t) = f cos(\omega_0 t) \tag{C.42}$$

Then,

$$A(\omega_0^2 - \omega^2) - 2\zeta\omega_0\omega B = 0 \tag{C.43}$$

$$B(\omega_0^2 - \omega^2) + 2\zeta\omega_0\omega A = f \tag{C.44}$$

when solving the above equation, A and B are defined as

$$A = \frac{2\zeta\omega_0\omega f}{\left(\omega_0^2 - \omega^2\right)^2 + 4\zeta^2\omega_0^2\omega^2},\ B = \frac{\left(\omega_0^2 - \omega^2\right) f}{\left(\omega_0^2 - \omega^2\right)^2 + 4\zeta^2\omega_0^2\omega^2} \tag{C.45}$$

Finally entire solution is as follows

$$z = A\sin(\omega t) + B\cos(\omega t) + e^{-\zeta\omega_0 t}\left(C\cos(\omega_0\sqrt{1-\zeta^2}t) + D\sin(\omega_0\sqrt{1-\zeta^2}t)\right) \tag{C.46}$$

With the initial condition as $z = 0,\ \dot{z} = 0$

$$B + C = 0 \tag{C.47}$$

$$C = -B = -\frac{\left(\omega_0^2 - \omega^2\right) f}{\left(\omega_0^2 - \omega^2\right)^2 + 4\zeta^2\omega_0^2\omega^2} \tag{C.48}$$

The time derivative of the equation is

$$\dot{z} = A\omega\cos(\omega t) - B\omega\sin(\omega t) - \zeta\omega_0 e^{-\zeta\omega_0 t}\left(C\cos(\omega_0\sqrt{1-\zeta^2}t) + D\sin(\omega_0\sqrt{1-\zeta^2}t)\right) \tag{C.49}$$

$$+e^{-\zeta\omega_0 t}\left(-C\omega_0\sqrt{1-\zeta^2}\sin(\omega_0\sqrt{1-\zeta^2}t) + D\omega_0\sqrt{1-\zeta^2}\cos(\omega_0\sqrt{1-\zeta^2}t)\right) \tag{C.50}$$

As $t = 0,\ \dot{z} = 0,$

$$\dot{z} = A\omega + \zeta B\omega_0 + D\omega_0\sqrt{1-\zeta^2} = 0 \tag{C.51}$$

$$D = -\frac{\zeta}{\sqrt{1-\zeta^2}}\frac{\left(\omega_0^2 + \omega^2\right) f}{\left(\omega_0^2 - \omega^2\right)^2 + 4\zeta^2\omega_0^2\omega^2} \tag{C.52}$$

Finally, the particular solution of non-homogeneous solution is $(\omega = \sigma)$

$$\begin{aligned} z(t) = {} & \frac{f}{(\omega_o^2 - \sigma^2)^2 + 4\zeta^2\omega_o^2\sigma^2}\left\{(\omega_o^2 - \sigma^2)\cos(\sigma\ t) + 2\zeta\omega_o\sigma\sin(\sigma\ t)\right. \\ & -\frac{\zeta}{\sqrt{1-\zeta^2}}e^{-\zeta\omega_o t}(\omega_o^2 + \sigma^2)\sin\left(\omega_o\sqrt{1-\zeta^2}\ t\right) \\ & \left.-(\omega_o^2 - \sigma^2)e^{-\zeta\omega_o t}\cos\left(\omega_o\sqrt{1-\zeta^2}\ t\right)\right\} \end{aligned} \tag{C.53}$$

Appendix D

Sloshing dynamics

D.1 Deriving the equation of motion

Acting on external torque $\vec{L}$ on slug is

$$\vec{L} = \mu\vec{\omega}_{S/B} \tag{D.1}$$

where μ is the non-negative viscous damping coefficient, $\vec{\omega}$ is the angular velocity of the slug relative to the body frame in the space craft. Angular momentum in the body frame is defined as

$$\vec{H}_B = I_B\vec{\omega}_{B/N} \tag{D.2}$$

Here, I_B is inertia matrix in the body frame and $\vec{\omega}$ is the angular velocity of the body with respect to the inertial frame. Using transport theorem and time derivative in the inertial frame,

$$\begin{aligned} {}^N\frac{d}{dt}\vec{H}_B &= {}^N\frac{d}{dt}I_B \times \vec{\omega}_{B/N} + I_B \times {}^N\frac{d}{dt}\vec{\omega}_{B/N} && \text{(D.3)} \\ &= I_B \times \left({}^B\frac{d}{dt}\vec{\omega}_{B/N} + \vec{\omega}_{B/N} \times \vec{\omega}_{B/N} \right) && \text{(D.4)} \\ &= I_B\dot{\omega} + \tilde{\omega}I_B\vec{\omega} = 0 && \text{(D.5)} \end{aligned}$$

Finally, equation of motion is defined as

$$\underline{I_B\dot{\omega} = -\tilde{\omega}I_B\vec{\omega} + \mu\vec{\omega}_{S/B}} \tag{D.6}$$

D.2 Dynamics of Slug

For the slug, within the space craft, angular momentum and velocities are as follows,

$$\vec{H}_S = J\vec{\omega}_{S/N},\ \vec{\omega}_{S/N} = \vec{\omega}_{S/B} + \vec{\omega}_{B/N} \tag{D.7}$$

Subscript S stands for space craft, and J is the spherical slug's inertia.

$$\begin{aligned}
\frac{^N d}{dt}\vec{H}_S &= \frac{^N d}{dt}\left(J\vec{\omega}_{S/N}\right) \\
&= \frac{^N d}{dt}J \times \vec{\omega}_{S/N} + J\frac{^N d}{dt}\left(\vec{\omega}_{S/N}\right) \\
&= J\left\{\frac{^B d}{dt}\left(\vec{\omega}_{S/N} + \vec{\omega}_{B/N} \times \vec{\omega}_{S/N}\right)\right\} \\
&= J\vec{\omega}_{S/N} + \tilde{\omega}J\vec{\omega}_{S/B} \qquad \text{(D.8)} \\
&= -\mu\vec{\omega}_{S/B} \qquad \text{(D.9)}
\end{aligned}$$

$^N\frac{d}{dt}$ denotes inertial derivative, $^B\frac{d}{dt}$ denotes the time derivative in the body frame, then equation of motion of slug with respect to the inertial frame is

$$\underline{J\dot{\omega}_{S/N} = -\tilde{\omega}J\vec{\omega}_{S/B} - \mu\vec{\omega}_{S/B}} \tag{D.10}$$

Equation of motion of the slug with respect to the body frame is

$$J\dot{\omega}_{S/B} + J\dot{\omega}_{B/N} = -\tilde{\omega}J\vec{\omega}_{S/B} - \mu\vec{\omega}_{S/B} \tag{D.11}$$

$$\underline{\dot{\omega}_{S/B} = -\dot{\omega} - \tilde{\omega}\vec{\omega}_{S/B} - \frac{\mu}{J}\vec{\omega}_{S/B}} \tag{D.12}$$